Fabrication and Control of Magnetic Pd,Fe Thin Film Heterostructures

by

Renee Michelle Harton

A dissertation submitted in partial fulfillment
of the requirements for the degree of
Doctor of Philosophy
(Physics)
in The University of Michigan
2016

Doctoral Committee:

Professor Roy Clarke, Chair
Professor Rachel S. Goldman
Assistant Professor Emmanouil Kioupakis
Professor Homer A. Neal
Professor Herbert G. Winful

ACKNOWLEDGEMENTS

I would like to thank my family for encouraging me throughout my graduate career. Without their undying love and support, none of this would have been possible. I would also like to thank the chair of my committee, Roy Clarke, for providing me with the opportunity to conduct research in his lab. I will be forever grateful for his faith in my abilities, which led him to provide me with the freedom to reach my full potential. Finally, I would like to thank each member of my committee for providing me with insight and perspective that was invaluable.

TABLE OF CONTENTS

CHAPTER

LIST OF FIGURES

LIST OF TABLES

<u>**Table**</u>

LIST OF ABBREVIATIONS

bcc body-centered cubic

fcc face-centered cubic

MOKE Magneto-Optic Kerr Effect

sc simple cubic

XRD X-Ray Diffraction

sc simple cubic

SO spin-orbit

ABSTRACT

Fabrication and control of magnetic Pd,Fe thin film heterostructures

by

Renee Michelle Harton

Chair: Professor Roy Clarke

The goal of this dissertation research is to investigate the use of multiferroic (ferroelectric-ferromagnetic) thin-film interfaces as a means to control the magnetization in materials of interest for perpendicular recording.This project explores the relationship between magnetization and structure in thin films of Fe/Pd compounds deposited onto ferroelectric $BaTiO_3$ substrates. Utilizing magnetostrictive coupling, the magnetism of a magnetic film was controlled by the epitaxial strain at the film/substrate interface. $BaTiO_3$ is particularly favorable for this purpose as its structure develops a significant elongation along the tetragonal c-axis as a result of symmetry breaking at the cubic to tetragonal phase transition. A novel aspect of the work is that we have tuned the Curie point of the ferromagnetic transition to approximately match the ferroelectric Curie point of the substrate, so that the magnetostrictive effect is maximized. This is achieved by alloying Fe with Pd to produce a Pd_3Fe compound. We report for the first time, the elastic control of the perpendicular magnetic anisotropy of Palladium-Iron (Pd,Fe) films deposited onto a barium-titanate ($BaTiO_3$) (100) substrate. Using Magneto-optic Kerr Effect (MOKE) magnetometry, we observed the behavior of the magnetization before and after the tetragonal-to-cubic phase transition of the $BaTiO_3$ substrate. We found that such films exhibited in-plane magnetization reversal below the T-C transition temperature, and out-of-plane magnetization reversal above the transition. This change in behavior demonstrates that it is possible to achieve elastic control of the perpendicular magnetic anisotropy of the deposited Pd,Fe film. In addition, we were able to grow an ordered $FePd_3$ film on $SrTiO_3$ using the inter-diffusion of an Fe/Pd multilayer heterostructure. Each layer of the heterostructure was deposited using Ultra-High Vacuum deposition. Utilizing in-situ RHEED (Reflection High Energy Electron Diffraction), we observed that each deposited layer was both ordered and exhibited the crystalline structure of the bulk material. Once deposited, the multi-layer heterostructure was heated above the $FePd_3$ formation temperature. Upon heating, the RHEED pattern began to exhibit the crystalline structure of $FePd_3$. Using X-ray Diffraction analysis and MOKE magnetometry, we found that the epitaxial film consisted primarily of $FePd_3$. This example of atomic layer epitaxy of Fe, Pd alloys represents a successful approach to forming high quality magnetic heterostructures on perovskites with excellent control over their composition and structural ordering.

CHAPTER I

Motivation

The concept of storing information on an external device is familiar; whether the information is stored using a hard drive, USB flash-drive, CD-Rom or a floppy disk, the idea of storing information on an external unit for future use is a common notion. Consequently, when designing a potential storage device, devising the physical requirements for this unit is an intuitive process.

First, one must identify the information that needs to be stored. Once selected, it is important that one is able to transfer this information onto the device. This step requires one to be able to control the state of the units or ”bits” used for storage. For the peace of mind of the user and the fidelity of the device, it is important that this process happens quickly. Once the information is written onto the device, we would like to ignore it until we need to use it again. When the time to re-use the stored data arrives, we would like to import/retrieve and possibly alter it from its original state. Consequently, once the information is written onto the device, it is important that the device maintain the information for the length of time between the writing event and the time of retrieval. Therefore, it is clear that the only constraint on the ”storage lifetime” of the device is the time difference between the writing and retrieval times. Unfortunately, most systems are not isolated. They are constantly interacting with their surroundings. As a result, if information is stored in a specific system, over time, the state of the system will change, which results in the degradation of the stored information. As a result, the lifetime of the stored information in a specific device is determined by the amount of time necessary to significantly distort the state of the system. These interactions with the surrounding environment, even over short periods of time, can significantly alter the signal. For a constant interaction, these disturbances result in a background signal, which can disguise the stored signal. However, if the stored signal is larger than the fluctuations caused by the surrounding environment, the stored signal can still be retrieved. In any event, the state of the information will change over time and needs to be considered when designing data storage devices.

If the information is stored in the orientation of the magnetization of a ferromagnetic material, the two anti-parallel states along a specific axis can be used as the two states used to represent the stored data. In order for these states to be used, one must ensure the fidelity of the device by requiring that the two states be distinguishable. This distinction is confirmed by using a system with a large saturation magnetization ($\mathbf{M}_S$). In a magnetically anisotropic system, $\mathbf{M_S}$ is proportional to K_uV, where K$_u$ is the uniaxial anisotropy coefficient along the axis of magnetization and V is the volume of the stored information bit.

In addition to the requirements of a storage device that have already been mentioned, it is always nice to think that storage capabilities are endless, that there is no limit to what can be stored. Nevertheless, the point is always reached when the storage device reaches capacity. In order to satiate this desire for greater storage capability, it is also important to maximize the amount of information that can be stored on the device. Increased storage can be achieved by increasing the areal storage density of the unit. In order to increase the number of bits stored in a certain area, one might decrease the volume, V, of the material in which an individual information "bit" is stored. However, since $\mathbf{M_S}$ depends on V, as V decreases, the uniaxial anisotropy (K_u) must increase. As a result, it is important that the material used has a large K_u value.

Another factor that contributes to the areal storage density of the device is the minimum distance between anti-aligned domains. This factor is determined by the size of the domain wall separating the domains. It has been shown that the size of the domain wall between neighboring domains aligned perpendicular to the sample surface is smaller than for those aligned along the sample plane[*Hubert and Schafer* (1998)]. As a result, there is interest in being able to store information in magnetic moments aligned perpendicular to the plane of the magnetic storage medium. The perpendicular recording alignment of magnetization perpendicular to the recording plane is favored for materials with a large perpendicular anisotropy coefficient. This coefficient for $Fe_{50}Pd_{50}$ tends to be larger than for other materials[*Endo et al.* (2005)]. This result led us to the Fe,Pd alloys. Since we wanted to control the magnetization perpendicular to the sample plane, it was important that we were able to tune the perpendicular magnetic anisotropy coefficient.

In 2006, Winkeman et.al. found that the perpendicular anisotropy of an $Fe_{50}Co_{50}$ film could be controlled using a tetragonal distortion induced by the lattice-mismatch between the film and the substrate. Using this information, we were interested in exploring the effect of a distortion of this sort on a Fe,Pd alloy. However, since we are interested in data recording applications, we wanted to impart a distortion to the deposited film that was reversible. Consequently, we took advantage of the properties of thin-film heterostructures where a ferromagnetic layer is deposited onto a substrate with tunable properties that could couple to the magnetism of the deposited film.

First, one might think to switch the magnetic state of a material using **H**-fields. Although possible, this method is not energy efficient due to the energy dissipation caused by Joule heating in the wires forming the solenoid used to generate the **H**-field. In this work, we found that a better way to manipulate the magnetization, one that uses less energy, is to exploit the magnetostriction of the substrate. Accordingly, we decided to tune the magnetic polarization of a material by coupling it to a substrate which has an order parameter controlled by temperature. A ferroelectric substrate is a suitable choice because it undergoes a structural transition at a certain temperature. Since multiferroics, in principle, allow for this sort of control, we investigated multiferroics that would suit our needs.

Multiferroics are materials that exhibit more than one ferroic order. Ferromagnetic order is characterized by a spontaneous magnetic polarization, ferroelectrics exhibit spontaneous electric polarization, and ferroelastic materials demonstrate spontaneous strain. As this work focuses on the storage of information in the magnetic spins of a material, we were interested in controlling the magnetic order of a material. Since the amount of energy dissipation is lower during the production of electric fields rather than magnetic fields generated by a solenoid, for this work we were interested in controlling the magnetization using electric fields. The most obvious material for this application is one that exhibits magneto-electric coupling.

The magnetoelectric coupling of a material can be described using the dependence of the free energy of a material on an electric field ($\mathbf{E}$) and magnetic field ($\mathbf{H}$). This relation can be described by the following equation:

$$\begin{aligned} F(\mathbf{E},\mathbf{H}) =& F_0 - P_i^S E_i - M_i^S H_i - \frac{1}{2}\epsilon_0\epsilon_{ij}E_iE_j - \frac{1}{2}\mu_0\mu_{ij}H_iH_j \\ & - \alpha_{ij}E_iH_j - \frac{1}{2}\beta_{ijk}E_iH_jH_k - \frac{1}{2}\gamma_{ijk}H_iE_jE_k \end{aligned} \tag{1.1}$$

The equilibrium values of the electric polarization ($\mathcal{P}_E$) and magnetization ($\mathbf{M}$) of the material are found by minimizing the free energy, F, with respect to $\mathbf{E}_i$ and $\mathbf{H}_i$, respectively. The result can be described by the following equation:

$$\begin{aligned} \mathcal{P}_E &= -\frac{\partial F}{\partial E_i} = P_i^S + \frac{1}{2}\epsilon_0\epsilon_{ij}E_i + \alpha_{ij}E_i + \frac{1}{2}\beta_{ijk}H_jH_k + \frac{1}{2}\gamma_{ijk}E_j \\ \mathbf{M} &= -\frac{\partial F}{\partial H_i} = M_i^S - \frac{1}{2}\mu_0\mu_{ij}H_j + \alpha_{ij}E_i + \frac{1}{2}\beta_{ijk}E_iH_j + \frac{1}{2}\gamma_{ijk}E_jE_k \end{aligned} \tag{1.2}$$

The Magneto-electric coupling due to the linear magneto-electric effect is described by the terms with the coupling constant, α_{ij}. From Equation (1.2), it is clear that an electric field E_i along $\mathbf{\hat{x}_i}$ results in a magnetization ($\mathbf{M}$) along the $\mathbf{\hat{j}}$ direction. Conversely, a magnetic field (H_i) results in an electric polarization, $\mathcal{P}$ along the $\mathbf{\hat{j}}$ direction. The sizes of $\mathcal{P}_E$ and $\mathbf{M}$ are dependent on the magneto-electric coupling constant, α_{ij}. It can be shown that α_{ij} must satisfy the following inequality:

$$\alpha_{ij} < \mu_{ij}\epsilon_{ij} \tag{1.3}$$

As a consequence of this inequality, the ME coupling is most pronounced in materials that exhibit both ferromagnetic and ferroelectric order. Since ferromagnetic ferroelectrics satisfy this criterion, these materials will be discussed next.

Ferromagnetic ferroelectrics are materials that simultaneously exhibit both ferromagnetic and ferroelectric ordering. Although these materials are of interest, materials where both orders are significant are not prevalent. The reason being the difference in the sources of the ferromagnetic and ferroelectric order. In most ferroelectrics, the spontaneous electric polarization is due to a structural distortion of the unit cell. This change in the positions of the ions of the unit cell results in a net displacement of the positive and negative charge centers. Ultimately, this shift results in an electric dipole moment, which leads to a net electric polarization when multiple crystallites are considered. On the other hand, the magnetic polarization is due to partially filled d-orbitals. Since the cations responsible for the ferroelectric polarization typically have empty d-orbitals, the source of the two orders must be separate. Indeed, the usual multiferroic combination with this sort of separation involves ferroelectricity and *anti*-ferromagnetic order. An example material is Bismuth Ferrite ($\mathrm{BiFeO_3}$). This multiferroic exhibits ferroelectric and anti-ferromagnetic order at RT. Although switching of the magnetization using electric fields has been demonstrated, since the material is AFM, the macroscopic spontaneous magnetization is zero[*Zhao et al.* (2006)]. Consequently, these materials are not directly useful for magnetic data storage. Owing to such difficulties, interest in single phase multiferroics has been stagnant for several years. Recently, there has been great interest in novel fabrication methods and theoretical modeling that has aided in devising and fabricating new multiferroic materials. Although these advances are significant, it is still challenging to create single component thin film single phase multiferroic materials[*Ramesh and Spaldin* (2007)].

One alternative approach, explored in this dissertation, is the use of multiferroic heterostructures consisting of multiple materials each of which exhibits a single ferroic order. Since the materials are only in contact at the interface, the potential coupling between the two materials can only occur at the interface of neighboring materials. As a result, the number of unit cells that experience the coupling is smaller, but the size of the ferroic orders can make up for this difference. In the case of a ferromagnetic/ferroelectric, $\mu_{ij}\epsilon_{ij}$ is larger than for a single phase ferromagnetic ferroelectric. Although this is promising, this effect is limited only to thin films. This is acceptable in a recording device, because most modern recording media are produced in thin film form, leading us to use epitaxial strain to control the magnetism of the magnetic thin film. For this reason, we were interested in materials whose magnetic state was strongly coupled to its elastic state. A magnetic material that exhibits coupling of this sort, when deposited onto a substrate that exhibits piezoelectric behavior can have magnetization that is indirectly tuned by a voltage. This was the goal of the work of this dissertation. The substrate chosen for this work was the perovskite, $BaTiO_3$. $BaTiO_3$ exhibits piezoelectric behavior and also has several structural phases. When $BaTiO_3$ is used as a substrate, changing its phase after the film has been deposited can impart strain to the deposited film. The effect of this strain on the magnetism has been demonstrated[*Sahoo et al.* (2007)]. For an Fe film deposited onto $BaTiO_3(001)$, the change in the in-plane lattice constant as it traversed the tetragonal(T)-Cubic(C) phase transition resulted in a strain anisotropy that caused a uniaxial magnetic anisotropy of the film. This effect confirmed the capability to tune the magnetization of deposited film by changing the strain state of the system. Equipped with this knowledge, we arrived at the focus of this dissertation.

For the research described in this dissertation, we probed the interfacial and structural interactions present in the heterostructure, PdFe/BTO. Bulk palladium-iron has been known to exhibit pressure-induced invar behavior which is accompanied by an increase in the volume magnetostriction of the bulk material[*Winterrose et al.* (2009)]. These experimental results suggest that the magnetization of a thin film of Pd,Fe might be strongly coupled to the position of the lattice ions and the deformation of the orbitals. For the research reported in this dissertation, thin films of Pd,Fe were deposited onto $BaTi O_3$. Using the structural phase transitions of $BaTiO_3$, we were able to observe the effect of the lattice parameters and electric state of the substrate on the magnetic state of the deposited film.

In order to enhance the coupling between the substrate and the film, we grew an ordered $FePd_3$ film on $SrTiO_3$ using the interdiffusion of an Fe/Pd multilayer heterostructure. The specifics of these experiments will be discussed in Chapters (III) and (IV) of the dissertation. The following chapter will discuss the background necessary to understand the results of these experiments.

CHAPTER II

Background

2.1 Magnetism

Everyday we interact with materials that vary widely in their intrinsic properties. Some materials feel soft, while others feel hard; some are smooth, and at the same time others feel rough. Although these properties seem not to be correlated, we know from elementary inorganic chemistry that all materials are made from the same set of fundamental particles. Consequently, one must conclude that the source of these differences in properties rests in the ways in which the fundamental particles are combined.

Since all materials can be described using the same fundamental particles, the differences that we observe in materials are actually caused by the difference in the combinations of these fundamental units. Since the atoms have a neutral charge, all of the possible combinations must have the same number of protons and electrons. Also, due to the sub-nuclear interactions, as the number of protons increases so must the number of neutrons. All of the combinations of protons, neutrons, and electrons that have been observed in nature are documented in the periodic table. In order to gain a general intuition for the different properties of materials made of different elements in the periodic table, it is important to note that the most apparent difference between various elements is their number of subatomic particles. Accordingly, understanding how these particles interact can elucidate the source of some of the different properties of materials made of different elements. In the next section of this dissertation, the subatomic interactions will be discussed.

We know from Coulomb's law [Equation(2.1)] that charged particles exert forces on each other. Using this law, one can conclude that the direction of the force the positively charged nucleus exerts on the electron will always be attractive, and the magnitude of this force will depend on the electron's distance from the nucleus. This electrostatic force has the following form:

$$\mathbf{F_E} = \frac{Ze^2}{4\pi\epsilon_0|\mathbf{r}|^2}\hat{\mathbf{r}} \tag{2.1}$$

where Z is the number of protons in the nucleus of the atom and $\mathbf{r}$ is the displacement vector between the nucleus and the electron. In order to determine the energy of an electron at a position, $\mathbf{r}_b$ from the nucleus, each electron can be assumed to be brought along a trajectory, where its initial position, $\mathbf{r}_a$, is effectively an infinite distance from the nucleus, such that the force from the nucleus is effectively zero, $\mathbf{F}_E = 0$, while at its final position, $\mathbf{r}_b$, F_E is non-zero. Here it is assumed that at position r_a, $\mathrm{V}_e = 0$. Upon reaching the position r_b from $\mathrm{r}_a = \infty$, the force $\mathbf{F}_E$ does work on the electron which results in a decrease in the potential energy of the particle. As a consequence, an electron with charge, e, positioned at the point $\mathbf{r}_b$ has a potential energy which can be described by the following equation:

$$V_e = -\frac{Ze^2}{4\pi\epsilon_0|\mathbf{r}|} \tag{2.2}$$

Since the potential energy of a particle of charge, q, at position, $\mathbf{r}_b$, is equal to qV_e, the implication of this decrease in the potential energy of the electron is that an energy equal to qV_e is needed to remove the particle from the electric field of the nucleus. As a result, electrons closer to the nucleus will require more energy to be removed from the electric field. Accordingly, for low energy interactions, the energies of the inner electrons can be assumed to be unchanged, and thus, only the outermost electrons are responsible for the different observed material properties. Since the majority of the properties of different materials are caused by the outermost electrons, it is important to understand the properties of the electron.

For the next set of derivations, the semi-classical description of the atom will be used. In this model, the electron orbits the nucleus at a fixed radius, **r**, that is quantized. Using the de Broglie wavelength of the electron, for each allowed orbit, it is required that the circumference of the orbit be equal to an integer number of wavelengths. This criterion can be described by the following:

$$\begin{aligned} n\lambda_B &= 2\pi r \\ \frac{nh}{p} &= 2\pi r \\ \frac{nh}{2\pi} &= rp \\ n\hbar &= \mathbf{L} \end{aligned} \tag{2.3}$$

where n marks the integer number of each orbit, λ_B is the associated de Broglie wavelength of the electron with a magnitude that is equal to $\lambda_B = \frac{h}{p}$, and r is the radius of the orbit. From Equation (2.3), it is clear that for an electron with a fixed λ_B, the difference in the radii of neighboring orbits (Δn) can be described by the following expression:

$$\Delta r = \frac{\lambda_B}{2\pi} \tag{2.4}$$

For an electron orbiting the nucleus at a fixed radius, r, the electron's motion about the nucleus results in a magnetic field, **B**, which can be described using the Biot-Savart law, which has the following form:

$$d\mathbf{B} = -\frac{\mu_0 \mathrm{I}}{4\pi}\frac{\mathbf{r} \times d\mathbf{l}}{\mathbf{r}^3} \tag{2.5}$$

Applying Equation (2.5) to the motion of the orbiting electron results in the following expression describing **B**:

$$\mathbf{B}(r) = -\mathrm{e}\frac{\mu_0}{2}\mathbf{r} \times \mathbf{v} \tag{2.6}$$

where **r** is the distance between each point of the electron orbit and the point of observation, **v** is the velocity of the electron, and e is the charge of the electron. Additionally from classical mechanics, we know that the angular momentum of the electron can be described by the following equation:

$$\mathbf{l} = \mathrm{m}_e\mathbf{r} \times \mathbf{v} \tag{2.7}$$

Solving for $\mathbf{r}\times\mathbf{v}$ in Equation (2.7), and inserting the result into Equation (2.6), we see that **B** can also be described by the following expression:

$$\mathbf{B} = -\frac{e}{2m_e}\mu_0\mathbf{l} \tag{2.8}$$

Although this magnetic field was derived from the motion of an electron about the nucleus of an atom, an equivalent magnetic field could be created by a stationary magnetic moment, **m**. This magnetic moment can be determined using the following constitutive relation:

$$\mathbf{B} = \mu_0(\mathbf{H} + \mathbf{M}) \tag{2.9}$$

where **H** is the magnetic intensity, **M** is the magnetization, and μ_0 is the magnetic permeability of free space. From Equation(2.9), it is clear that an equivalent field **B** emanates from a magnetic moment described by the following expression:

$$\mathbf{m} = -\frac{\mathrm{e}}{2m_e}\mathbf{L} = \gamma\mathbf{L} \tag{2.10}$$

From this equation, it is clear that the angular momentum, **L**, and the magnetic moment, $\mathbf{m}$, are of opposite sign and that their magnitudes differ by a factor of $\frac{e}{2m_e}$. This factor, γ, describing the mapping of the electron's angular momentum, $\mathbf{L}$, to a magnetic moment, $\mathbf{m}$, is often referred to as the gyromagnetic ratio. Returning to the angular momentum of the orbiting electron, since the angular momentum defined in Equation (2.7), depends on the radius of the electron and the electron orbit is quantized, the angular momentum, $\mathbf{L}$, must also be quantized. This quantization of $\mathbf{L}$ can be described by the following equation:

$$\mathbf{L} = m_l \hbar \tag{2.11}$$

where m_l is the orbital angular momentum quantum number. From Equation (2.3), we can see that the $\Delta\mathbf{L}$ of neighboring allowed orbits ($\Delta n = 1$) is equal to $\hbar$. As a result, the change in m_l for neighboring orbits is equal to 1. Consequently, for an electron with an angular momentum, $\mathbf{l}$, the possible projections of this angular momentum along a specific axis must satisfy the following inequality, $|\mathbf{m}_l|<|\mathbf{l}|$. where $\Delta\mathrm{m}_l = 1$ for each step.

Later, it was discovered that the orbital angular momentum was not the only source of angular momentum for the electron, but that there was also an intrinsic angular momentum which altered the electron's total magnetic moment, and consequently, the resultant magnetic field. The source of this intrinsic angular momentum is called spin, and is equal to $\frac{\hbar}{2}$ for the electron. As was the case for the orbital angular momentum, the spin angular momentum can be mapped to a magnetic moment, $\mathbf{m}_s$. The relation between the spin angular momentum, $\mathbf{s}$, and this magnetic magnetic moment, $\mathbf{m}_s$, can be described by the following relation:

$$\mathbf{m_s} = -\frac{e}{m_e}\mathbf{s} = \gamma_s \mathbf{s} \tag{2.12}$$

It is important to note that the spin gyromagnetic ratio (γ_s) is 2 times larger than the orbital gyromagnetic ratio(γ_l). Similar to the orbital angular momentum, the projections of the spin angular momentum are also quantized. The value of $\Delta\mathbf{s}$ between different projections of the spin angular momentum along a specific axis is equal to $\hbar$, which corresponds to a value of $\Delta\mathrm{m}_s$ that is equal to 1 for neighboring projections. As a result, **s** has only two projections along a specific axis, which are equal to $\frac{\hbar}{2}$ and $\frac{-\hbar}{2}$. For the remainder of this section of the dissertation, both the orbital and spin angular momenta will be projected along the $\hat{\mathbf{z}}$ axis. As a result,

$$\begin{aligned} \hat{\mathbf{s}} \cdot \hat{\mathbf{z}} &= m_s\hbar \\ \hat{\mathbf{l}} \cdot \hat{\mathbf{z}} &= m_l\hbar \end{aligned} \tag{2.13}$$

Prior to this point in the dissertation, each orientation of the magnetic moments of the electron were energetically equivalent. However, since this dissertation focuses on how the magnetic moments of a system respond to external stimuli, for the remainder of this section, the effect of an external magnetic field on the magnetism of a material will be explored.

We know from classical mechanics that in the absence of an applied magnetic field, every orientation of a magnetic dipole is energetically equivalent. However, when it is in the presence of an external magnetic field, **B**, this symmetry is broken, and certain orientations of the magnetic moments are energetically favored. The energy of each orientation of a magnetic dipole relative to an external magnetic field, **B**, can be described by the following equation:

$$U = -\mu \cdot \mathbf{B} \tag{2.14}$$

where μ is the classical magnetic dipole moment and **B** is the external magnetic field. It is important to note that the configuration with the lowest energy occurs when the magnetic dipole moment is aligned with the applied magnetic field. In the case of the classical magnetic dipole, the allowed orientations of the dipole are continuous. Accordingly, the possible energies of the magnetic dipole in an applied magnetic field are also continuous. However, since the projections of the spin and orbital magnetic moment are quantized, it is clear that this is not the case for the magnetic moment of the electron. Nevertheless, the case of the classical magnetic dipole is illustrative and will be used to understand the energies of the electron in an external magnetic field using the quantum picture. In the absence of an external field, the configurations of both the electron's orbital magnetic moment and spin magnetic moment are equivalent. However, as was the case for the classic magnetic dipole, an applied external field breaks this symmetry. This interaction is often called the Zeeman interaction. The Hamiltonian describing the interaction of a magnetic field directed along the z-axis with the spin and orbital magnetic moments of the electron can be described by the following equation:

$$H = -\frac{\mu_B}{\hbar}(\hat{\mathbf{l}} + 2\hat{\mathbf{s}}) \cdot \mathbf{B} = -\frac{\mu_B}{\hbar}(\hat{\mathbf{m}}_{\mathbf{l}} + 2\hat{\mathbf{m}}_{\mathbf{s}})B_z = -\mu_B(m_l + 2m_s)B_z \tag{2.15}$$

where m$_s$ and m$_l$ are the quantum numbers of the spin and orbital angular momenta, respectively, and μ_B is the Bohr magneton, which is equal to $\frac{\gamma_l}{\hbar}$, From this equation, it is clear that the magnetic field breaks the degeneracy of the different projections of the spin and orbital angular momenta described by the $\mathbf{m}_s$ and $\mathbf{m}_l$ quantum numbers. Resulting in the magnetic moments that are aligned with **B**, those with positive magnetic quantum numbers, resulting in the lowest energies. From this equation, we see that the energy of a magnetic dipole is minimized when the dipole is aligned with the external field, **B**. From this analysis, it is clear that an applied magnetic field breaks the symmetry of the system resulting in the orientation aligned with the applied **B** having the least energy. As a result, one might assume that all materials when placed in an external magnetic field will enhance the magnetic field, because all of the magnetic moments will align with the field. Although this is the case for certain materials, such as paramagnetic materials and ferromagnets; there are materials that when placed in magnetic fields have spins that align in the opposite direction. The response of a material to an external magnetic field is described by the magnetic susceptibility, χ. This parameter can be determined using the following relation:

$$\chi = \frac{\mu_0 \mathbf{M}}{\mathbf{B}} \tag{2.16}$$

In the following sections, the physics of paramagnetic materials and ferromagnetic materials will be discussed. The first class of materials discussed will be paramagnetic.

2.1.1 Paramagnetism

As was mentioned in Section (2.1), paramagnetic materials are those which when place in an external magnetic field, increase the magnitude of the field. This section of the dissertation will describe the physics behind this phenomenon.

From Section (2.1), we know that the interaction of an electron with an external magnetic field, **B**, is referred to as the Zeeman interaction, and can be described by a Hamiltonian of the following form:

$$\mathcal{H}_{Zeeman} = -\frac{\mu_B}{\hbar}(\hat{\mathbf{l}} + 2\hat{\mathbf{s}}) \cdot \mathbf{B} = -\frac{\mu_B}{\hbar}(2\mathbf{m_s} + \mathbf{m_l}) \cdot B\hat{\mathbf{z}} = \mu_B(m_l + 2m_s)B \tag{2.17}$$

For this derivation, we will consider a single electron in the s-orbital of an atom. Consequently, the orbital angular momentum,**l**, will be equal to zero. Accordingly, the possible energies of this single electron can be described by the following equation:

$$E = -2\mu_B m_s B \tag{2.18}$$

The thermodynamic average of a parameter,f, can be described by the following equation:

$$< f >= \frac{1}{\mathcal{Z}} \sum_{n=1}^{N} f_n e^{\frac{E_n}{k_B T}} \tag{2.19}$$

where m spans the number of possible configurations, N, and $\mathcal{Z}$ is the partition function and can be described by the following equation:

$$\mathcal{Z} = \sum_{n=1}^{N} e^{\frac{E_n}{k_B T}} \tag{2.20}$$

$$< \mathrm{m} >= \frac{1}{\mathcal{Z}} \sum_{n=1}^{N} \mathrm{m}_i e^{\frac{E_i}{k_B T}} = \frac{\mu_B (e^{\frac{\mu_B B}{k_B T}} - e^{-\frac{\mu_B B}{k_B T}})}{(e^{\frac{\mu_B B}{k_B T}} + e^{-\frac{\mu_B B}{k_B T}})} \tag{2.21}$$

This equation can also be represented by the following equation:

$$< \mathbf{m} >= \mu_B (\frac{e^x - e^{-x}}{e^x + e^{-x}}) = \mu_B \tanh(x) \tag{2.22}$$

where x=$\frac{\mu_B B}{k_B T}$. At room temperature, x<< 1, as a result, tanh(x)∼x. In this limit, $< \mathbf{m} >$ can be described by the following equation:

$$< \mathbf{m} >= \frac{\mu_B^2 B}{k_B T} \tag{2.23}$$

For this derivation, only the spin of a single electron was considered. The results of this derivation can be extended to a material with multiple electrons if the electrons do not interact with one another. For this sort of system, the total magnetization, **M**, of a system with n electrons can be described by the following equation:

$$\mathbf{M} = n < \mathbf{m} >= n \frac{\mu_B^2 B}{2 k_B T} \tag{2.24}$$

Since the magnetic susceptibility, χ is described by the following equation:

$$\chi = \frac{\mu_0 \mathbf{M}}{\mathbf{B}} \tag{2.25}$$

.

For this system of n independent electrons, the magnetic susceptibility (χ) can be described by the following equation:

$$\chi = \frac{n\mu_0 \mu_B^2}{k_B T} \tag{2.26}$$

In this derivation, only the magnetism of a single spin was considered. Although this illustration was useful, the atoms used for the studies described in this dissertation, contained atoms with several electrons. Consequently, it would be illustrative to extend this analysis to a system with several electrons. The remainder of this section will focus on this subject.

For a single electron in the s-orbital of an atom, the total spin angular momentum, $\mathbf{S}$, is equal to $\frac{1}{2}$. Accordingly, there are only two orientations of the associated magnetic moment, $\mathbf{m}_s$. However for an electron in another type of orbital or for several electrons, the situation is more complex. In both of these cases, the total angular momentum of the systems includes more than one angular momentum vector. Since both the orbital and spin angular momenta are vectors, the total angular momentum, $\mathbf{J}$, must include a vector sum. As a result, $\mathbf{J}$ is described by the following expression:

$$\mathbf{J} = \mathbf{L} + \mathbf{S} \tag{2.27}$$

where $\mathbf{L}$ and $\mathbf{S}$ are the total orbital and spin angular momenta of all of the electrons, respectively. As was the case for a single electron, the total angular momentum can be described in terms of $\hbar$ using the following equation:

$$\mathbf{J} = M_J \hbar \tag{2.28}$$

where M_J are natural numbers. As was the case for the single electron, the different orientations of **J** are quantized. The change in the total angular momentum , $\Delta\mathbf{J}$, between neighboring orientations is is $\hbar$ while $\Delta M_J=1$. Consequently, there are 2J+1 possible orientations of the **J**, these states can be described by the following set of equations:

$$\begin{gathered} \mathbf{J} : -M_J\hbar < \mathbf{J} < M_J\hbar \\ M_J : -\frac{J}{\hbar} < M_J < \frac{J}{\hbar} \end{gathered} \tag{2.29}$$

It is clear that the classical case where the possible orientations of the magnetic moment are continuous is reached as J $\rightarrow \infty$. As was the case for the single s-electron, none of the orientations of **J** are energetically favored. However when this system of electrons with total angular momentum, **J**, is placed in an external magnetic field, **B**, this symmetry is broken. Once again, the interaction of the external **B** and the magnetic moments of an atom can be described using the Zeeman interaction [Equation(2.17)] which has the following form:

$$\mathcal{H}_{Zeeman} = -\mathbf{m} \cdot \mathbf{B} \tag{2.30}$$

For a magnetic field, **B**, directed along $\hat{\mathbf{z}}$, $\mathcal{H}_{Zeeman}$ has the following form:

$$\mathcal{H}_{Zeeman} = -\mathbf{m} \cdot \mathbf{B} = \frac{\mu_B}{\hbar}(\mathbf{L_z} + 2\mathbf{S_z})B_z \tag{2.31}$$

Equation (2.31) can be simplified using the Landé g-factor, g_l, which is defined as the ratio of the projection of the total magnetic moment along the total angular momentum, **J**, and the magnitude of **J** and has the following form:

$$g_l = \frac{1}{2}\frac{\mathbf{S}(\mathbf{S}+1) - \mathbf{L}(\mathbf{L}+1)}{\mathbf{J}(\mathbf{J}+1)} + \frac{3}{2} \tag{2.32}$$

Employing the Landé g-factor, g$_l$, the magnitude of **J** has the following form:

$$\mathbf{m} = g_l \frac{\mu_B}{\hbar}\mathbf{J} = g_l \mu_B M_J \tag{2.33}$$

Consequently, $\mathcal{H}_{Zeeman}$ [Equation(2.31)], can be described by the following equation:

$$\mathcal{H}_{Zeeman} = g_l \mu_B M_J \mathbf{B_z} \tag{2.34}$$

Applying Equation (2.19) to an atom with several electrons, one finds that the thermodynamic average <**M**> of an atom with several electrons can be described by the following equation:

$$< \mathbf{M} >= \frac{1}{\mathcal{Z}} \sum_{-J}^{J} M_J e^{-i\frac{E_n}{k_B T}} = \frac{1}{\mathcal{Z}} \sum_{J}^{J} M_J e^{i\frac{g_l \mu_B M_J B}{k_B T}} \tag{2.35}$$

The Taylor series expansion of e has the following form:

$$\sum_{n=1}^{N} \frac{x^n}{n!} \approx 1 + x \text{ (for small x)} \tag{2.36}$$

Applying Equation (2.36) to Equation (2.35) results in the following equation:

$$< \mathbf{M} >= \frac{1}{\mathcal{Z}} M_J \sum_{-J}^{J} e^x \tag{2.37}$$

where $x = \frac{g_l \mu_B M_J B}{k_B T}$. For temperatures near and above RT, x<<1. As a result, $< \mathbf{M} >$

for T near and above RT, can be described by the following equation:

$$< \mathbf{M_z} >= \frac{g_l \mu_B}{\mathcal{Z}} \sum_{-J}^{J} M_J (1 - \frac{g_l \mu_B M_J B}{k_B T}) \tag{2.38}$$

where the partition function, $\mathcal{Z}$, has the following form:

$$\mathcal{Z} = \sum_{-J}^{J} e^{-i \frac{g_l \mu_B M_J B}{k_B T}} \tag{2.39}$$

Inserting Equation (2.39), into Equation (2.38), we find that $< \mathbf{M} >$ can be described by the following equation:

$$< \mathbf{M}_Z >= -\frac{g_l \mu_B \sum_{-J}^{J} M_J (1 - \frac{g_l \mu_B M_J B}{k_B T})}{\sum_{-J}^{J} e^{-i \frac{g_l \mu_B M_J B}{k_B T}}} \tag{2.40}$$

Evaluating the sums in Equation (2.40) results in the following equation:

$$< \mathbf{M_Z} >= \frac{\mu_B^2 g_l^2 B [J(J+1)]}{3 k_B T} \tag{2.41}$$

Applying Equation (2.16) to Equation (2.41) to determine the magnetic susceptibility, χ, of the multi-electron atom, one finds that χ can be described by the following expression:

$$\chi = \frac{\mu_0 g_l^2 \mu_B^2 H [J(J+1)]}{3 k_B T} \tag{2.42}$$

This result diverges as T → 0, and suggests a change in the behavior as T approaches zero. Below a critical temperature, this description fails for magnetic materials.

2.1.2 Ferromagnetism

This section will discuss the physics of ferromagnetic materials, which as mentioned in Section (I) have a spontaneous magnetic polarization in the absence of an applied field. As much as these materials are described by their magnetic polarization in the absence of an externally applied field, they are also defined by the temperature above which this order disappears. This temperature is called the Curie Temperature, T_C. Below this T_C, the material is ferromagnetic. Ferromagnetism is caused by the exchange interaction which can be described by the following equation:

$$H_{exchange} = -J\mathbf{s_1} \cdot \mathbf{s_2} \tag{2.43}$$

where J is the coupling constant and $\mathbf{s_1}$ and $\mathbf{s_2}$ are the magnetic spin momenta. It is important to note that when $|J|>0$, the parallel alignment of neighboring spins is favored. The parallel alignment of magnetic spins results in a spontaneous magnetization, **M**, which is the defining characteristic of ferromagnetic materials.

2.2 Crystalline structure of ordered materials

The experiments described in this dissertation investigate the properties of both random and ordered alloys. Consequently, this section of the dissertation will introduce the formalism used to describe ordered structures which will be discussed in more detail in Sections (2.2.1) and (2.2.2).

Crystalline solids can be modeled using the repetition of a single unit at regularly spaced points throughout space. Using this representation, one can describe a crystal lattice by first describing the repeated fundamental unit and finally the lattice along which the element is copied. The position of the points on the underlying lattice can be represented by the following expression:

$$\mathbf{r}_{\mathrm{b}} = \sum_{i=1}^{3} \mathrm{c}_{\mathrm{i}}\mathbf{R_i} \tag{2.44}$$

where $\mathrm{c_i}$ spans the natural numbers and $\mathbf{R}_{\mathrm{i}}$ has the following form:

$$\mathbf{R_i} = \mathrm{R_i}\mathbf{\hat{x}_i}. \tag{2.45}$$

In this equation, $\mathbf{\hat{x}_i} = [\mathbf{\hat{x}}, \mathbf{\hat{y}}, \mathbf{\hat{z}}]$, and $\mathrm{R_i}$ is equal to the spacing of the points along the direction, $\mathbf{\hat{x}_i}$. R_i is often referred to as the lattice constant. Collectively, the points described by Equation (2.45) form the direct lattice of a material. Looking at Equation (2.44), it is clear that the direct lattice is composed of regularly spaced points separated along the direction specified by $\mathbf{\hat{x}_i}$. The ions of this lattice interact with the electrons of the lattice ions via the Coulomb interaction. Since the lattice ions are positioned at regular intervals throughout space, the potential, $\mathrm{U}(\mathbf{r})$, which describes this interaction will exhibit the same repetition and thus can be represented by the following equation:

$$\mathrm{U}(\mathbf{r} + \mathbf{R_i}) = \mathrm{U}(\mathbf{r}) \tag{2.46}$$

To determine the electron wavefunctions, the time-independent Schrödinger equation must be used; which has the following form:

$$-\frac{\hbar^2}{2m}\nabla^2\psi(\mathbf{r}) + \mathbf{U}(\mathbf{r})\psi(\mathbf{r}) = E\psi(\mathbf{r}) \tag{2.47}$$

Since the potential, $\mathbf{U}(\mathbf{r})$, can be described by Equation (2.46), one can expect the electron wavefunctions to exhibit the same repetition excepting a phase which can be described by a plane wave. Therefore, the electron wavefunction can be described by the following equation:

$$\psi(\mathbf{r} + \mathbf{R_i}) = \psi(\mathbf{r})e^{i\mathbf{k}\cdot\mathbf{R_i}} \tag{2.48}$$

where $\mathbf{k}$ is the spatial frequency of the plane wave. It is clear from Equation (2.48), that $\psi(\mathbf{r} + \mathbf{R_i}) = \psi(\mathbf{r})$ only if the plane wave meets the following criterion:

$$e^{i\mathbf{k}\cdot\mathbf{R_i}} = 1 \qquad (2.49)$$

This equation, Equation (2.49), only holds if the period of the plane wave, $\frac{2\pi}{K}$, is equal to a multiple of the spacing between the units of the underlying lattice, n$*$R$_i$, or if the following equation is valid.

$$\mathbf{K} \cdot \mathbf{R_i} = 2\pi\mathrm{n} \qquad (2.50)$$

where n spans the natural numbers. Using Equations (2.45) and (2.50), it is evident that **K** can be represented by the following expression:

$$\mathbf{K} = \frac{2\pi}{\mathrm{R_i}} \sum_{i=1}^{3} \mathrm{b_i}\mathbf{a_i} \qquad (2.51)$$

where each element of b_i spans the natural numbers. The points described by Equation (2.51) form a lattice which is often called the reciprocal lattice. We will return to this lattice when we describe the physics behind X-Ray crystallography, which will be used to characterize the structure of the materials studied in this dissertation. More immediately, in the next section the formalism used to describe the direct lattice will be explained.

2.2.1 Crystalline Structure of metals

In Section (2.2), the formalism used to specify the direct lattice of ordered materials was introduced. This section of the dissertation will build upon the framework laid in this introduction. As in Section (2.2), the general presentation of this topic will be similar to that of *Ashcroft and Mermin* (1976). However, only the examples and representations pertinent to the samples studied in this thesis will be highlighted. Interested readers should refer to *Ashcroft and Mermin* (1976) for a more thorough explanation of this topic.

As introduced in Section (2.2), the lattice of a crystalline solid can be modeled using the repetition of a physical element at regularly positioned points throughout space. At each lattice site, either a single atom or a combination of atoms can be placed. In either case, this underlying lattice is ordered. Accordingly, one should be able to describe the position of each point of the lattice, relative to a fixed origin, using a combination of integer multiple translations along a fixed set of displacement vectors. This condition which was stated in Equation (2.44) can be expressed by the following definition:

> **The position, R, of any point of a Bravais lattice, with respect to a fixed origin, can be described using the displacements described in Equation (2.44), which are, collectively, restated in the following equation:** (2.52)
>
> $$\mathbf{R} = \sum_i \mathrm{n}_i \mathbf{R}_i$$
>
> **where $\mathbf{R}_i$ is defined in Equation (2.45) and $\mathbf{n}_i$ is the magnitude of the vector component along the direction specified by $\mathbf{R}_i$.**

The collection of points described by Equation (2.52) form a Bravais lattice, while the unit vectors, $\mathbf{x}_i$, are its primitive vectors. It is important that, altogether, the primitive vectors, $\mathbf{x}_i$, span the space used to describe the specific lattice. Additionally, for a fixed value of n_i, the points described by $\mathrm{R_i}$ form the minimum number of sites necessary to form the specific Bravais lattice. This collection of points is called the unit cell of the Bravais lattice. Another formulation of the Bravais lattice definition [Equation (2.52)] is captured by the following statement:

> **For every point in a Bravais lattice, the structure and orientation of the surrounding lattice points must be independent of the position of the point in the lattice.** (2.53)

Although Equation (2.52) and statement (2.53) are equivalent, the geometric nature of statement (2.53) allows one to quickly determine whether a particular lattice suits the

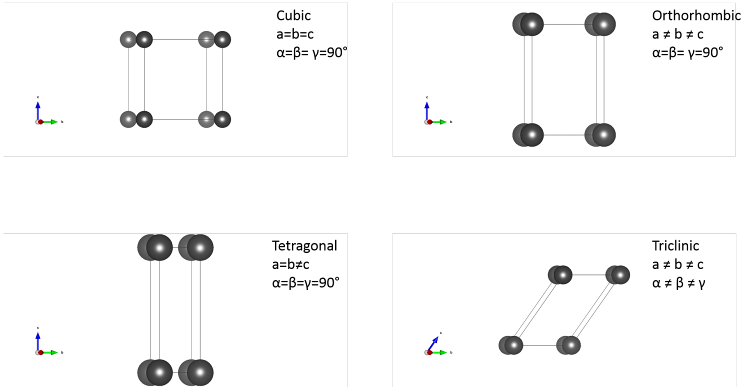

Figure 2.1: Examples of Bravais lattices

Bravais lattice criterion *Ashcroft and Mermin* (1976). Consequently, throughout this dissertation, the definition (2.53) will be used to determine whether a specific lattice qualifies as a Bravais lattice. This categorization of each lattice has implications that present themselves while using X-ray crystallography to determine the structure of the specific material. This connection will be clarified in Section (2.8) where X-ray crystallography will be discussed. In the remaining portion of this section, the structure of the Bravais lattices that will be important for the work of this dissertation will be covered.

There are only 219 distinct structures that qualify as Bravais lattices. A small subset of these Bravais lattices are displayed in Figure (2.1) along with their definitions. A good introduction to the structure of Bravais lattices is possibly the most basic one, the simple cube. The positions of the lattice sites of the unit cell of a simple cube can be described using the following set of unit vectors:

$$\begin{aligned} \mathbf{a_1} &= a\hat{\mathbf{x}}, \\ \mathbf{a_2} &= a\hat{\mathbf{y}}, \\ \mathbf{a_3} &= a\hat{\mathbf{z}}. \end{aligned} \tag{2.54}$$

It is clear that a monatomic simple cube satisfies the Bravais lattice definition specified by Equation (2.53). However, for the face-centered cubic (fcc)face-centered cubic

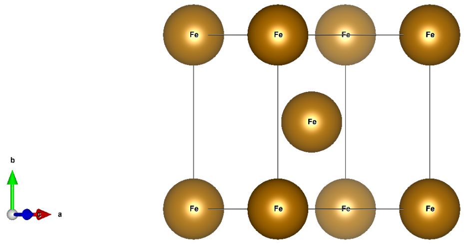

Figure 2.2: Schematic drawing of bcc Fe conventional unit cell

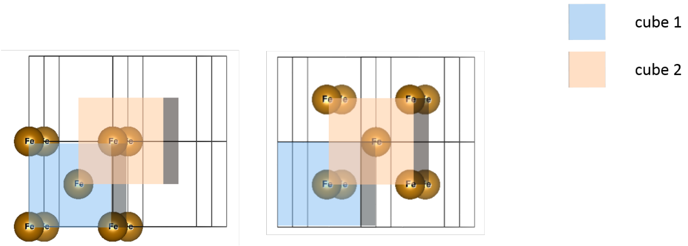

Figure 2.3: Schematic drawing of alternate depiction of bcc Fe lattice

(fcc) lattice and the body-centered cubic (bcc) lattice, this connection is not so transparent. Since these two examples are important for the work of this thesis, they will now be discussed. The bcc unit cell consists of a simple cube with an atom at its center. Figure (2.2) displays the conventional unit cell of the bcc Fe lattice. Applying Statement (2.53) to the conventional unit cell displayed in Figure (2.2), it is clear that the structure and orientation of the surrounding lattice points of each corner atom are equivalent. However, the surrounding lattice points of the center atom seem to differ from those surrounding the corner atoms. Accordingly, one might conclude that this lattice does not satisfy the definition and thus is not a Bravais lattice. However, upon further investigation, it becomes clear that the bcc structure can also be represented using interpenetrating cubes as in Figure (2.3). Using this representation, it is clear that the corner atom of **cube 1** is the center atom of **cube 2**. Meanwhile, the corner atom of **cube 2** is the center atom of **cube 1**. Since a single atom can be both the corner and center atom of a cube, depending on the cube's position in the

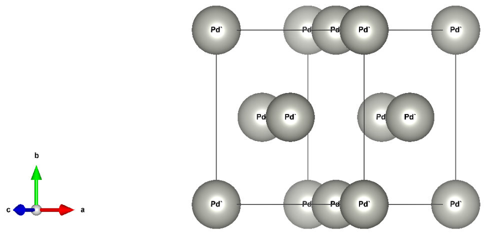

Figure 2.4: Schematic drawing of face centered cubic Pd conventional unit cell

lattice, it is clear that the surrounding lattice environment of the atoms in both of the positions are identical. This equivalence in the structure and orientation of the lattice points surrounding the center and corner points of the bcc conventional unit cell confirms that the bcc lattice is a Bravais lattice. Applying the first formulation of the Bravais lattice definition, Equation (2.52), to this lattice, one finds that each point of the lattice can be reached through integer multiple displacements along the following primitive vectors:

$$\begin{aligned} \mathbf{a_1} &= \frac{a}{2}(-\hat{\mathbf{x}} + \hat{\mathbf{y}} + \hat{\mathbf{z}}), \\ \mathbf{a_2} &= \frac{a}{2}(\hat{\mathbf{x}} - \hat{\mathbf{y}} + \hat{\mathbf{z}}), \\ \mathbf{a_3} &= \frac{a}{2}(\hat{\mathbf{x}} + \hat{\mathbf{y}} - \hat{\mathbf{z}}) \end{aligned} \tag{2.55}$$

Similar to the bcc lattice, the fcc lattice is also cubic, but instead of having an atom at the cube's center, the fcc lattice has a single atom at the center of each cubic face. The fcc Pd conventional unit cell is displayed in Figure (2.4). After observing this conventional unit cell, one might conclude that the fcc lattice is not a Bravais lattice according to Equation (2.53), because the surrounding lattice of the corner atoms are not the same as those of the atoms at the cubic faces. Nonetheless, as was the case with the bcc lattice, the fcc lattice can also be represented as interleaving cubes. A schematic representation of one face of the lattice can be found in Figure

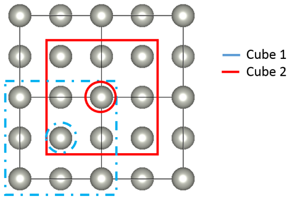

Figure 2.5: Schematic drawing of face-centered cubic Pd lattice

(2.5). This figure demonstrates this mixing. It is clear from Figure (2.5), that the atoms at the center of the faces of the original cube (**cube 1**) form the corners of a second cube (**cube 2**). The corners of **cube 1** are the atoms at the center of the faces of **cube 2**. This representation of the lattice demonstrates that the atoms at the center of the cubic faces are equivalent to the atoms at the corners of the fcc conventional unit cell. Consequently, the fcc lattice meets the condition for a Bravais lattice. It is important to note that this equivalence only holds if the atoms of **cube 1** and **cube 2** are of the same species, and is invalid if they are different. In the case where the elements of the cubes differ, the structure must be represented using an underlying Bravais lattice with a physical element replicated at each point of the lattice. This copied physical element is called a basis. It can contain a single atom or a combination of atoms. It is important to note that the ordered materials described completely using only the primitive vectors of the Bravais lattice also consisted of a basis, but it only included one atom. Since the *lattice with a basis* portrayal is the most general description approach, this method will be used to describe the structures in the remainder of this thesis. In the latter portion of this section, the *lattice with a basis* formalism will be used to describe the important structures of this dissertation, starting with the bcc lattice.

In order to represent the bcc lattice using the *lattice with a basis* formalism, it is most helpful to look at two neighboring unit cells of the bcc lattice. Figure (2.6)

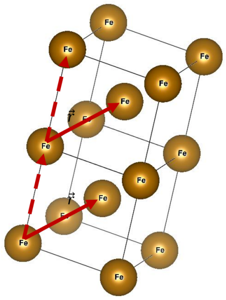

Figure 2.6: Schematic drawing of Fe bcc unit cell with basis and translation vector

shows these neighboring conventional unit cells. Looking at the positions of the atoms in Figure (2.6), it is clear that both cells can be represented by translating the corner atom and the center atom along the primitive vectors of a simple cube. Consequently, one can conclude that the underlying Bravais lattice can be represented by the lattice vectors of a simple cube which have the following form:

$$\begin{aligned}\mathbf{a_1} &= a\hat{\mathbf{x}}, \\ \mathbf{a_2} &= a\hat{\mathbf{y}}, \\ \mathbf{a_3} &= a\hat{\mathbf{z}}\end{aligned} \tag{2.56}$$

where a is the lattice constant of the bcc unit cell. The basis of the structure can be represented by the following basis vectors which are measured using the same coordinate system used to describe the lattice of the simple cube:

$$\begin{aligned}\mathbf{r_1} &= \mathbf{0}, \\ \mathbf{r_2} &= \frac{a}{2}(\hat{\mathbf{x}} + \hat{\mathbf{y}} + \hat{\mathbf{z}})\end{aligned} \tag{2.57}$$

In order to find the primitive vectors and basis vectors needed to describe the fcc lattice, one can look at Figure (2.4). From this figure, it is evident that the fcc lattice can be represented by translating the corner and the center atoms in the xy, yz, and xz planes along the vectors of a simple cube. As a result, the lattice vectors are equivalent to those described in Equation (2.56). While the basis vectors have the following form:

$$\begin{aligned}
\mathbf{r_1} &= \mathbf{0}, \\
\mathbf{r_2} &= \frac{a}{2}(\hat{\mathbf{x}} + \hat{\mathbf{y}}), \\
\mathbf{r_3} &= \frac{a}{2}(\hat{\mathbf{y}} + \hat{\mathbf{z}}), \\
\mathbf{r_4} &= \frac{a}{2}(\hat{\mathbf{x}} + \hat{\mathbf{z}})
\end{aligned} \tag{2.58}$$

As the previous examples demonstrate, the *lattice with a basis* formalism can be used to describe a monatomic Bravais lattice. However, since each of these structures can be described using only primitive vectors, this method seems unnecessary. It is not until one works to describe a structure with multiple atoms that the power of the *lattice with a basis* formalism is unveiled. Since, for these systems the primitive vector representation fails. This fact is highlighted by the description of the structures, $FePd_3$, FePd, $SrTiO_3$, and $BaTiO_3$. None of these structures can be completely described using only primitive vectors. Consequently, in the latter portion of this section, the structure of the unit cells of these materials will be described using the *lattice with a basis* formalism.

The unit cell of $FePd_3$ consists of a simple cube with Fe at the corners of the cube and Pd atoms at the center of the cubic faces. A schematic drawing of this structure can be found in Figure (2.7). Since this structure contains two types of atoms, it is not a Bravais lattice. However, it can be described using the *lattice with a basis* formalism. In this case, the unit cell of the underlying Bravais lattice can be modeled as that of a simple cube which can be described using the lattice vectors of Equation (2.56) with a four atom basis, 1 Fe atom and 3 Pd atoms. The position of the 4 atoms

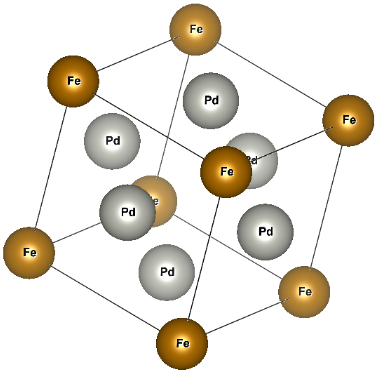

Figure 2.7: Conventional unit cell of $FePd_3$

can be described by the following basis vectors:

$$\begin{aligned}\mathbf{Fe}(1)\colon\ & \hat{\mathbf{0}},\\ \mathbf{Pd}(1)\colon\ & \frac{a}{2}(\hat{\mathbf{x}}+\hat{\mathbf{y}}),\\ \mathbf{Pd}(2)\colon\ & \frac{a}{2}(\hat{\mathbf{y}}+\hat{\mathbf{z}}),\\ \mathbf{Pd}(3)\colon\ & \frac{a}{2}(\hat{\mathbf{x}}+\hat{\mathbf{z}}).\end{aligned} \tag{2.59}$$

where the lattice constant,a, is 3.848 Å. A material with this structure is said to exhibit L_{12} ordering. The structure of FePd consists of a tetragonal unit cell with Fe atoms at two of the opposing tetragonal face centers, and two Pd atoms at the centers of the other two opposing faces and the bottom and top faces. A schematic representation of the FePd conventional unit cell can be found in Figure (2.8). Using the *lattice with a basis* formalism, FePd can be described using a tetragonal Bravais

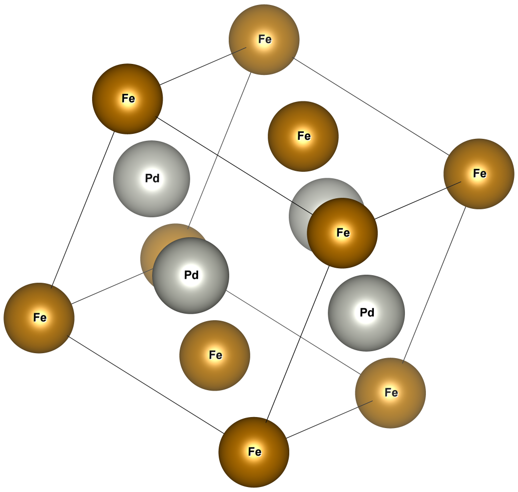

Figure 2.8: FePd unit cell

lattice, described by the following primitive vectors:

$$\begin{aligned}\mathbf{a_1} &= \mathrm{a}\hat{\mathbf{x}},\\ \mathbf{a_2} &= \mathrm{a}\hat{\mathbf{y}},\\ \mathbf{a_3} &= \mathrm{c}\hat{\mathbf{z}}.\end{aligned} \tag{2.60}$$

where a and c are 3.723 Åand 3.852 Å, respectively. Since the FePd structure has Pd atoms at the center of its bottom face and two of its opposing faces and Fe at the center of the other two opposing faces, the position vectors of the basis atoms can be described by the following vectors:

$$\begin{aligned}\mathbf{Fe}(1) &= \hat{\mathbf{0}},\\ \mathbf{Fe}(2) &= \frac{b}{2}\hat{\mathbf{y}} + \frac{c}{2}\hat{\mathbf{z}},\\ \mathbf{Pd}(1) &= \frac{a}{2}\hat{\mathbf{x}} + \frac{c}{2}\hat{\mathbf{z}},\\ \mathbf{Pd}(2) &= \frac{a}{2}\hat{\mathbf{x}} + \frac{b}{2}\hat{\mathbf{y}}.\end{aligned} \tag{2.61}$$

A structure of this sort is said to exhibit L_{10} ordering. During the final portion of this

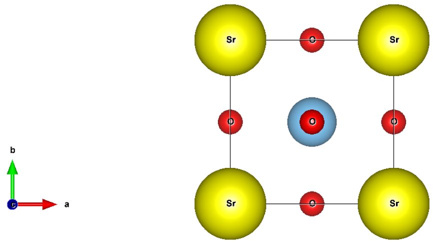

Figure 2.9: $SrTiO_3$ unit cell

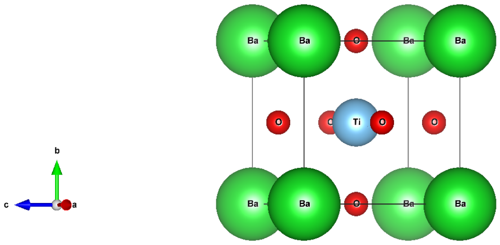

Figure 2.10: $BaTiO_3$ unit cell

section, the structure of the two perovskites, $SrTiO_3$ and $BaTiO_3$ will be reviewed.

Although these perovskites exhibit different structural phases at different temperatures,the structure of these materials at room temperature will be discussed in this section. The structures of their additional phases along with the temperatures where they exist will be discussed in Section (2.5.1). Schematic drawings of their unit cells can be found in Figure (2.9) and Figure (2.10), respectively. At room temperature, $SrTiO_3$ consists of a simple cube of Sr^{+2} atoms, with a Ti^{+4} ion at its center. The Ti^{+4} ion is surrounded by 6 O^{-2} ions which form an octahedron centered about the Ti^{+4} ion. Using the *lattice with a basis* formalism, the underlying Bravais lattice is a simple cube with primitive vectors described by the vectors in Equation (2.56), where

a is 5.511Å. The basis vectors can be described by the following vectors:

$$\begin{aligned}
\mathbf{Sr}(1) &= 0, \\
\mathbf{Ti}(1) &= \frac{a}{2}(\hat{\mathbf{x}} + \hat{\mathbf{y}} + \hat{\mathbf{z}}), \\
\mathbf{O}(1) &= \frac{a}{2}(\hat{\mathbf{x}} + \hat{\mathbf{y}}), \\
\mathbf{O}(2) &= \frac{a}{2}(\hat{\mathbf{x}} + \hat{\mathbf{z}}), \\
\mathbf{O}(3) &= \frac{a}{2}(\hat{\mathbf{y}} + \hat{\mathbf{z}}).
\end{aligned} \tag{2.62}$$

$BaTiO_3$ has a similar structure to $SrTiO_3$, but at room temperature its structure is tetragonal. The $BaTiO_3$ unit cell consists of Ba^{+2} ions at the corners of the tetragonal structure and a Ti^{+4} atom positioned at the center of the tetragonal structure. Surrounding the Ti^{+4} ion are 6 O^{-2} ions which form an octahedron about the ion. A symbolic diagram of the $BaTiO_3$ structure can be found in Figure (2.10). The $BaTiO_3$ structure can be described using an underlying tetragonal lattice with vectors described in Equation (2.60) where a, b, and c are equal to 3.99 Å,3.99 Å, and 4.04 Å, respectively. The positions of the atoms in the basis can be described by the following vectors:

$$\begin{aligned}
\mathbf{Ba}(1) &= 0, \\
\mathbf{Ti}(1) &= \frac{a}{2}(\hat{\mathbf{x}} + \hat{\mathbf{y}} + \hat{\mathbf{z}}), \\
\mathbf{O}(1) &= \frac{a}{2}(\hat{\mathbf{x}} + \hat{\mathbf{y}}), \\
\mathbf{O}(2) &= \frac{a}{2}\hat{\mathbf{x}} + \frac{c}{2}\hat{\mathbf{z}}, \\
\mathbf{O}(3) &= \frac{a}{2}\hat{\mathbf{y}} + \frac{c}{2}\hat{\mathbf{z}}.
\end{aligned} \tag{2.63}$$

As described in Section (2.2), for the work described in this dissertation, the alloys, FePd and $FePd_3$ will be deposited onto the substrates $BaTiO_3$ and $SrTiO_3$. These structures will be revisited to describe their magnetic and electric properties. The next section of this dissertation will provide the framework necessary to describe the reciprocal lattice which is used in X-ray crystallography to determine the crystalline structure of the materials used in this study.

2.2.2 The Reciprocal lattice

Section 2.2.1 discussed the formalism used to characterize the crystalline structure of ordered materials. Although these methods adequately describe crystals, in practice, the crystalline structure is not measured directly. Instead, diffraction techniques are implemented to determine the reciprocal lattice. The results of these measurements are then used to determine the structural properties of the direct lattice. Consequently, in order to deduce the structure of the direct lattice from these measurements of the reciprocal lattice, one must understand the structure of the reciprocal lattice and how this structure relates to its corresponding direct lattice. In this section of the dissertation, we will explore this connection. The section will begin with a definition of the reciprocal lattice that is more easily applied than Equation (2.51), and conclude with a visual representation of the relation between the reciprocal and direct lattices.

As was discussed in Section (2.2), every ordered crystal lattice can be modeled as a periodic structure. One method used to model this periodic configuration uses a train of impulses. A single impulse positioned at $\mathbf{r} = n|\mathbf{a_0}|$ can be described by the following function:

$$\mathrm{f(x)} = \delta(\mathrm{x} - \mathrm{n}|\mathbf{a}_0|) \tag{2.64}$$

where $|\mathbf{a_0}|$ is the lattice constant of the 1D lattice, $\delta(\mathrm{x})$ is the Dirac delta function, and n spans the natural numbers. Consequently, a train of impulses along one dimension can be described by the following equation:

$$f_{1D}(x) = \sum_{n=1}^{\infty} \delta(\mathrm{x} - \mathrm{n}|\mathbf{a_0}|) \tag{2.65}$$

Since Equation (2.65) is periodic with a period of $|\mathbf{a_0}|$, one can use Fourier decomposition to describe the function as a scaled sum of sinusoidal functions. Using these methods, a general function, g(x), can be represented as a scaled sum of sinusoidal functions with the following general form:

$$g(x) = \sum_{m=-\infty}^{\infty} \hat{\mathrm{G}}_{\mathrm{m}} e^{\mathrm{im}\pi\frac{\mathbf{x}}{\mathrm{L}}} \tag{2.66}$$

where 2L equals the period of the function, which for our example is equal to $\mathrm{a_0}$, and the coefficients, $\hat{\mathrm{G}}_{\mathrm{m}}$, can be described by the following equation:

$$\hat{G}_m = \frac{1}{2L}\int_{-L}^{L} f(x) e^{-\mathrm{im}\pi\frac{\mathrm{x}}{\mathrm{L}}} dx. \tag{2.67}$$

Applying Equation(2.67) to the impulse centered at $\mathbf{x} = 0$, one can represent the periodic function, f(x), [Equation (2.65)] as a sinusoidal sum, with Fourier coefficients of the following form:

$$\hat{G}_m = \frac{1}{|a_0|}\int_{-\frac{|a_0|}{2}}^{\frac{|a_0|}{2}} \delta(x) e^{-im\pi\frac{x}{L}} = \frac{1}{|a_0|} \tag{2.68}$$

Inserting Equation (2.68) into Equation (2.66) , we find that the 1D train of impulses can be described by a function with the following form:

$$\mathbf{f}(\mathbf{x}) = \sum_{m=-\infty}^{\infty} \frac{1}{|a_0|} e^{2im\pi\frac{x}{|a_0|}} \tag{2.69}$$

It is well known that the dual pair of the delta function, $\hat{\delta}(k_x)$, can be described by the following equation, *Ablowitz and Fokas* (2003):

$$\mathcal{F}[\hat{\delta}(k_x - k_0)] = \frac{1}{2\pi}\int_{-\infty}^{\infty} \hat{\delta}(k_x - k_0) e^{ik_x x} dk_x = \frac{1}{2\pi} e^{ik_0 x} \tag{2.70}$$

Using this result, one can deduce that the inverse Fourier transform of a shifted Dirac delta function has the following form:

$$2\pi\hat{\delta}(k_x - k_o) \overset{\mathcal{F}^{-1}}{\Longrightarrow} e^{ik_o x} \tag{2.71}$$

$$\mathcal{F}[f(x)] = \frac{2\pi}{|a_0|} \sum_{m=-\infty}^{\infty} \delta(k_x - \frac{2m\pi}{|a_0|}) \tag{2.72}$$

Using the relation highlighted in Equation (2.72), one can conclude that the Fourier transform of a train of impulses each separated by intervals of length, $|\mathbf{a_{x_0}}|$, in position space is equal to a train of impulses in reciprocal space, each separated by intervals equal to $\frac{2\pi}{|\mathbf{a_{x_0}}|}$.

Since, the crystal lattice is composed of a series of atoms spaced at equal intervals equal to a_0, one can conclude that the reciprocal lattice of the crystal will consist of a series of regularly spaced points at intervals equal to $\frac{2\pi}{a_0}$. Similar to the case of the direct lattice, the positions of these points in reciprocal space must be described using vectors. In multiple dimensions, a clear definition of these vectors is needed. This will be the next topic discussed in this section.

Using the Bloch equation [Equation (2.49)], one is able to deduce that the reciprocal lattice vectors must be parallel to the direct lattice vectors. Consequently, the reciprocal lattice vectors of a 1D direct lattice with lattice vector, $\mathbf{a}_{x0}$, can be described by the following equation:

$$\mathbf{k_1} = \frac{2\pi}{|\mathbf{a_{x_0}}|}\mathbf{\hat{a}_{x_0}} \tag{2.73}$$

The results of this analysis used to determine the reciprocal lattice of a 1D lattice can be easily applied to a 2D lattice with atomic spacings of $|\mathbf{a_{x0}}|$ and $|\mathbf{a_{y0}}|$ along the x and y directions, respectively. As was the case for the 1D lattice, the 2D lattice can be modeled as a train of impulses described by the following equation:

$$\mathrm{f(x,y)} = \sum_{n_y}\sum_{n_x} \delta(\mathrm{x} - \mathrm{n}_x|\mathbf{a_{x_0}}|)||\delta(\mathrm{y} - \mathrm{n}_y|\mathbf{a_{y_0}}|) \tag{2.74}$$

where n_x and n_y span the natural numbers. Applying the results of Equation (2.72) to each dimension of the 2D lattice, one finds that the magnitude of the reciprocal lattice vectors are $\frac{2\pi}{|\mathbf{a_{x_0}}|}$ and $\frac{2\pi}{|\mathbf{a_{y0}}|}$. We also know from Equation (2.49) that the direction of each reciprocal lattice vector is parallel to its corresponding direct lattice vector. Accordingly, both the magnitude and direction of the reciprocal lattice vectors of the 2D direct lattice can be described by the following set of equations:

$$\begin{aligned} \mathbf{b_1} &= 2\pi\frac{\hat{\mathbf{z}} \times \mathbf{a_{y_0}}}{\Omega_2} \\ \mathbf{b_2} &= 2\pi\frac{\hat{\mathbf{z}} \times \mathbf{a_{x_0}}}{\Omega_2} \end{aligned} \tag{2.75}$$

where Ω_2 is the area of the direct lattice unit cell, which is equal to $\Omega_2 = |\mathbf{a_{x_0}}||\mathbf{a_{y0}}|$. Since the materials studied in this dissertation will have 3 dimensions, the results of this analysis must be applied to a lattice with 3 dimensions. Using the formalism used to describe the 1D and 2D lattice, a 3D Bravais lattice with lattice spacings, $|\mathbf{a}_{x0}|$, $|\mathbf{a}_{y0}|$, $|\mathbf{a}_{z0}|$, along the x,y and z axes, respectively, can be described by the following equation:

$$\mathrm{f(x,y,z)} = \sum_{n_z}\sum_{n_y}\sum_{n_x} \delta(\mathrm{x} - \mathrm{n_x}|\mathbf{a}_{\mathrm{x}0}|)\delta(\mathrm{y} - \mathrm{n_y}|\mathbf{a}_{\mathrm{y}0}|)\delta(\mathrm{z} - \mathrm{n_z}|\mathbf{a}_{\mathrm{z}0}|) \tag{2.76}$$

Using the results of Equation (2.49) and Equation (2.72), we can conclude that the reciprocal lattice vectors of the 3D direct lattice can be described by the following set of equations:

$$\begin{aligned}
\mathbf{k_x} &= 2\pi\frac{\mathbf{a_{y_0}} \times \mathbf{a_{z_0}}}{\Omega_3}, \\
\mathbf{k_y} &= 2\pi\frac{\mathbf{a_{z_0}} \times \mathbf{a_{x_0}}}{\Omega_3}, \\
\mathbf{k_z} &= 2\pi\frac{\mathbf{a_{x_0}} \times \mathbf{a_{y_0}}}{\Omega_3}.
\end{aligned} \tag{2.77}$$

where $\Omega_3 = \mathbf{a_{x_0}} \cdot (\mathbf{a_{y_0}} \times \mathbf{a_{z_0}})$ and $\mathbf{a_{i_0}}$ are the primitive vectors of the corresponding direct lattice. Applying the set of equations in Equation (2.77) to the unit vectors of the bcc lattice [Equation (2.55)], one finds that the reciprocal lattice of the bcc lattice is the fcc lattice. Moreover, if Equations (2.77) are applied to the unit cell of a simple cube [Equation (2.54)], it is clear the reciprocal lattice of a simple cube is a simple cube. This result will prove to be important for the analysis of the XRD results described in this dissertation. Although this set of equations enables one to describe the components of the reciprocal lattice quantitatively, a visual representation of the connection between the two lattices is hidden. We will now introduce another representation that elucidates this relation.

Up to this point in the dissertation, each material structure has only been characterized by its entire unit cell. Although this is a logical presentation, it is not the only method. One can also look at a specific material as being composed of different planes of atoms. Since the entire crystal lattice is ordered and, in theory, infinite, every lattice plane of atoms is infinite. This also means that for each lattice plane, there exists an infinite set of such planes each separated by fixed intervals throughout space. Every set of planes is referred to as a family of planes. Figure (2.11a) illustrates the family of lattice planes of a simple cube that are parallel to the x-axis. However, upon further inspection of this figure, one can conclude that this family of planes is not unique. There are also lattice planes that are perpendicular to the $< 110 >$ vector. This family of planes is illustrated in Figure (2.11b). As these two examples demonstrate, a single family of planes is often not a unique description of

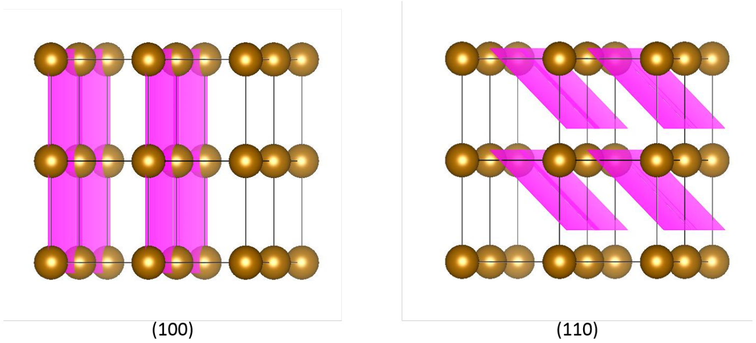

Figure 2.11: Schematic drawing of a simple cubic lattice with highlighted (100) and (110) planes

a crystal lattice. However, we will later see that in X-ray diffraction the total sum of the reflections from each family of lattice planes can uniquely describe the crystalline structure of a material. From Figure (2.11), it is clear that a family of lattice planes can be described by a vector that is perpendicular to the planes. After further consideration of the properties of the reciprocal lattice, it will become clear that the reciprocal lattice vectors are perpendicular to the lattice planes of a Bravais lattice, and can be used to identify each family of lattice planes. In the remainder of this section, this relation between the lattice planes of a Bravais lattice and the reciprocal lattice vectors will be examined.

As Section (2.2) illustrates, the phase of the electron's wavefunction can be described by a plane wave that satisfies Equation (2.49). This equation requires the phase of the wavefunction to be equal to unity at the Bravais lattice sites. From elementary complex variables, we know that along the direction of $\mathbf{k}$, the plane wave amplitude oscillates with a spatial frequency of $|\mathbf{k}|$. Meanwhile, perpendicular to $\mathbf{k}$, there is no variation in the plane wave amplitude. One can use this information, to determine the orientation of the plane wave relative to a general family of lattice planes. For any family of lattice planes, one can position a plane at the position $\mathbf{r} = 0$. For all the points on this plane, $\mathbf{e}^{i\mathbf{k}\cdot\mathbf{r}} = \mathbf{e}^{i\mathbf{k}\cdot\mathbf{0}} = 1$. As a result, the variation of the plane wave used to describe the change in the phase of $\Psi(\mathbf{r})$ must occur for translations perpendicular to the surface of the lattice plane. Consequently, $\mathbf{k}$ must be perpendicular to the plane of atoms. Moreover, since $\Psi(\mathbf{r}+\mathrm{n}\mathbf{R}_{\mathrm{i}}) = \Psi(\mathbf{r})$, the electron wavefunction must be equal to unity at each point on each plane of the family. Since the direct lattice has a period of $\mathbf{R}_{\mathrm{i}}$, each plane is surrounded by two neighboring planes, each separated by a distance, $\mathbf{R}_i$, from the original plane. Using this analysis, one might conclude that the orientation of a family of lattice planes can be uniquely described by the Bravais lattice vector, $\mathbf{R}_i$. Although the neighboring lattice points are separated by the displacement vector, $\mathbf{R}_i$, this vector does not uniquely describe the orientation of the plane, since, the lattice sites within a single plane are also separated by the same displacement vector, $\mathbf{R}_i$. Although this is the case for the Bravais lattice vector,$\mathbf{R}_i$, the reciprocal lattice vector,$\mathbf{K}$ must always be perpendicular to the plane of lattice sites. As a result, $\mathbf{K}$ uniquely describes the orientation of the plane.

From this analysis, one can conclude that each family of planes can be uniquely described by the shortest reciprocal lattice vector,$\mathbf{K}_0$, of the crystal's Bravais lattice. Using the following definition of $\mathbf{K}$,

$$\mathbf{K} = l\mathbf{b_1} + m\mathbf{b_2} + n\mathbf{b_3}, \tag{2.78}$$

a family of planes can be described by the reciprocal lattice vector $\mathbf{K_0}$ with a length that is equal to the separation of two adjacent planes in reciprocal space. Accordingly, a specific family of planes perpendicular to the vector $<$ h k l $>$ in reciprocal space with adjacent planes separated by the length of $<$ h k l $>$ in reciprocal space is described using the notation (h k l) where h, k, and l are each called Miller indices when used in this notation. Although this analysis is useful, this definition describes the plane in reciprocal space. In order to connect these indices to distances in direct space, the plane of lattice sites described by (l m n) intersects the x_1, x_2, and x_3 axes at the points described by the following equation:

$$\begin{aligned} x_1 &: \frac{a_1}{h} \\ x_2 &: \frac{a_2}{k} \\ x_3 &: \frac{a_3}{l}. \end{aligned} \tag{2.79}$$

where a_1,a_2, and a_3 are the x, y and z-intercepts of the lattice plane. For the remainder of this dissertation, the notation, <h k l>, will be used to denote the components of a vector in reciprocal space, and (h k l) will be used to refer to the plane perpendicular to this vector.

2.3 Coupling between crystalline structure and magnetism

2.3.1 Magnetic Anisotropy Energy (MAE)

From elementary quantum mechanics, we know that the potential of a single atom is spherically symmetric. Ignoring the interactions between the electrons of the atom, there is no preferred configuration of the spin magnetic moment. However in a simple cubic Bravais crystal lattice there are several atoms positioned at regular intervals along the $\hat{x}$, $\hat{y}$,and $\hat{z}$ directions. The presence of these surrounding lattice ions breaks the symmetry of the single atom Hamiltonian. The potential created by the other ions in the crystal is commonly referred to as the crystal field, V_{cf}. The addition of V_{cf} to the Hamiltonian changes the eigenstates of the system. This potential plays a large role in the magnetocrystalline anisotropy, which will be discussed in the next subsection.

Generally speaking, any interaction that is not spherically symmetric will break the symmetry of the system and will result in magnetic anisotropy. The energy of a specific configuration of the magnetic moments of the system, can be described by the free energy, G. The effect of interactions on the free energy of the system can be described by the following contributing free energy term, G$_s$

$$G_s = K_a \sin^2(\theta - \theta_0) \tag{2.80}$$

where K$_a$ is the anisotropy coefficient which has units, $\frac{J}{m^3}$ and is specific to the source of the interaction, and θ is the angle of the magnetization of the system relative to an axis of interaction. It is important to note that the sign of K$_a$ determines whether θ_0 is the favored orientation of the magnetization. In order to determine the preferred orientation of the system, the free energy must be minimized with respect to θ. The resulting angle is the preferred axis of the system. The interactions that are important for the work in this dissertation are the magnetocrystalline anisotropy energy, magneto-electric coupling, magneto-elastic coupling, and shape anisotropy. These interactions along with their effects on the magnetic anisotropy of the system will be discussed in the following subsections.

2.3.2 Magnetocrystalline Anisotropy Energy

In a crystal lattice, the electrons of a single atom interact with the neighboring lattice ions through the electrostatic Coulomb interaction. Ignoring the Coulomb interaction between neighboring electrons, the orbitals of the electrons of a single atom are impacted by this 'crystal field' created by the surrounding lattice ions. As a result, the electron orbitals that were originally degenerate experience shifts due to this new term in the Hamiltonian of the electrons. The orbital that describes the position of the electron when this interaction is included is the one with the lowest energy. In this manner, the orbital angular momentum, **L** is coupled to the lattice. Moreover, since the spin orbit coupling within a material can be generally described by the following potential:

$$V_{SO} = \mathrm{c}\ \mathbf{L} \cdot \mathbf{S} \tag{2.81}$$

where c is a constant that is specific to the material. In materials where V_{SO} is large, the energy of the electron is minimized when the spin angular momentum is aligned with its orbital angular momentum. This coupling results in a magnetic anisotropy of the crystal where the preferred orientations of the magnetic moments align with the axes of the lattice. The contribution of this interaction in a cubic lattice on the total free energy (F) of the system can be described by the following equation:

$$\begin{aligned} F_{MCA} =& K_1[\cos^2(\theta_1)\cos^2(\theta_2) + \cos^2(\theta_2)\cos^2(\theta_3) + \cos^2(\theta_3)\cos^2(\theta_1)] \\ &+ K_2[\cos^2(\theta_1)\cos^2(\theta_2)\cos^2(\theta_3)] \end{aligned} \tag{2.82}$$

where θ_1, θ_2, and θ_3 are the angles between $\mathbf{M}$ and <100>,<010> and <001>, respectively. For a tetragonal system with an elongated axis the x-axis, F_{MCA} has the following form:

$$F_{MCA} = K_1^2[\sin^2\theta_1 + K_2\sin^4\theta_1] + K_3\cos^2(\theta_2)\cos^2(\theta_3) \tag{2.83}$$

This coupling will be important when analyzing the results of the experiments described in this dissertation.

2.3.3 Magneto-elastic coupling and Magnetostriction

In magnetostrictive materials, the lattice distorts when the material is in the presence of an external magnetic field, **H**. As was mentioned in Section (2.1), when magnetic dipole moments are placed in an external magnetic field, **H**, the energy of the magnetic moments is minimized when they are aligned with this magnetic field. Conversely, the energy reaches its maximum value when the magnetic moments are anti-aligned. As mentioned in Section (2.1), this interaction is commonly referred to as the Zeeman interaction. The direction of a collection of spin magnetic moments can also be affected by another coupling that is experienced when spin magnetic moments are in the presence of other spin magnetic moments. This is the exchange interaction, and is described by the following equation:

$$\mathcal{H}_{ex} = J_{ij}\mathbf{s_i} \cdot \mathbf{s_j} \tag{2.84}$$

where $\mathbf{s_i}$ and $\mathbf{s_j}$ are the spin magnetic moments of the ith and jth electron, and J_{ij} is the coupling constant which describes the magnitude of the exchange coupling between these two electrons. $|\mathrm{J}_{ij}|$ strongly depends on the distance between the electrons. For most materials, it only has a significant impact on the energies of the nearest neighboring spins. The effect of exchange coupling on the response of spin magnetic moments in the presence of an applied magnetic field, **H**, is to reduce the magnitude of the applied **H**-field necessary to magnetize the material along dir(**H**). Due to the exchange interaction, when one spin aligns with **H**, the energy of the neighboring spins is reduced when aligned with this spin.

J_{ij} is strongly affected by the spacing of the ith and jth electrons. This dependence is captured by the constant, g, which can be described by the following expression:

$$\epsilon g = \epsilon\frac{\partial \mathcal{H}_{ex}}{\partial \epsilon} = \epsilon\frac{\partial J_{ij}}{\partial r_{ij}}\frac{\partial r_{ij}}{\partial \epsilon}(\mathbf{s_i} \cdot \mathbf{s_j}) \tag{2.85}$$

where ϵ is the applied strain, r_{ij} is the spacing between the ith and jth electrons. From Equation (2.85), the magnitude of the exchange interaction between neighboring electrons is determined by the derivative, $\frac{\partial J_{ij}}{\partial \epsilon}$. The rate of change of the coupling constant, J_{ij}, with applied strain depends on the specifics of the material. Since magnetizing a magnetostrictive material alters the lattice, the source of this coupling must be an interaction that couples the spatial properties of the material with its magnetic properties, one such interaction is spin-orbit coupling. The potential of this interaction is described by the following equation:

$$\mathcal{H}_{SO} = \mathrm{c}\ \mathbf{L} \cdot \mathbf{S} \tag{2.86}$$

For magnetic materials that exhibit large spin-orbit coupling, when the magnetic moments minimize their energy by aligning with the applied **H**, due to $\mathcal{H}_{SO}$, the energy of the system is minimized when the orbital magnetic moments are aligned with the the spin magnetic moment. The change in the orientation of **L** results in the change in shape of the material. For materials, with small $\mathcal{H}_{SO}$, this coupling between the spin and orbital magnetic moments is negligible and thus the magnetostriction is minimal.*Duc and Brommer* (2002)

For the magnetic materials studied in this dissertation, the atom responsible for the ferromagnetic properties of the samples is Fe. Fe, a 3d atom, has delocalized electrons. Since the electrons are delocalized their energies are more strongly affected by the surrounding ions. These interactions largely decrease the orbital magnetic moment, which results in an $\mathcal{H}_{SO}$ that is negligible. Accordingly, the spin magnetic moments are able to align with an external **H** while the orbital magnetic moments remain effectively unchanged.*Duc and Brommer* (2002) This results in a magnetostriction coefficient that is non-zero, but is small compared to materials where the spin-orbit coupling is stronger.

Magnetostriction is empirically described using the magnetostriction coefficient, λ, which is defined by the following expression:

$$\lambda \equiv \frac{\Delta \mathbf{l}}{\Delta \mathbf{H}} \tag{2.87}$$

where l is the length of the material and **H** is the magnitude of the applied magnetic field. The deformation of a material can be described using the following modes: isotropic deformations, anisotropic deformations, and shear deformations.

For a volume with cubic symmetry, an isotropic deformation alters the volume of the material while maintaining the original symmetry of the material. Consequently, this distortion is achieved by changing each lattice constant in the same manner. Anisotropic deformations remove the cubic symmetry, while still maintaining the volume of the original cube. Shear deformations reduce the symmetry of the material by altering the angles of the cube while maintaining the lattice constants and volume of the original structure. Magnetostriction that results in isotropic deformations is described by the isotropic magnetostriction (λ_0). Magnetostriction that results in an anisotropic deformation along <xyz> in the presence of an external magnetic field **H** with dir(**H**)=<xyz> is referred to as linear magnetostriction, and described by the magnetostriction coefficient, λ_{xyz}. In general, the relative sign of the change in volume (isotropic deformation), lattice constant (anisotropic deformation), angle (sheer deformation) to the original cube is described by the sign of the magnetostriction coefficient, λ. In the remainder of this thesis, the coupling between the lattice of a material and its magnetism will be described using the magnetostriction coefficients.

2.3.4 Magneto-electric coupling

As was mentioned in Section (2.1), the angular momentum of the electron has two components, one that is associated with the electron's orbital motion while the other contribution is associated with the spin of the electron. When an electron is placed in an electric field, **E**, it experiences a force, $\mathbf{F_e}$, which is opposite the dir(**E**) for electrons. As a result, the orbits of the electrons are altered due to this external field. Accordingly, the direction of the orbital angular momentum, **L**, is also changed.

As was described in Section (2.3.2), the orbital angular momentum electron is coupled to its spin angular momentum through the spin-orbit coupling interaction, V_{SO}. The effect of this interaction on the energy of the electron is minimized when the spin angular momentum (**S**) and the orbital angular momentum (**L**) are aligned.

Consequently, in materials where the orbital angular momentum is not quenched, an external electric field can indirectly control the magnetism of the material.

For the materials studied in this dissertation, the electric field was induced by the electric polarization of the $BaTiO_3(100)$ substrate while in its tetragonal (ferroelectric) state. Since the $BaTiO_3$ is only in contact with the deposited film at the film/substrate interface, only the orbits of the electrons near the interface will be impacted by the electric polarization of $BaTiO_3$ while in this phase. As a result, the Magneto-electric coupling in multiferroic heterostructures occurs only at the interface, and thus does not play a significant role in deposited films that are thick. This reasoning will be important in the analysis of the results of the experiments described in this dissertation.

2.4 Properties of Fe and Fe alloys

2.4.1 Allotropes of Fe

Between the temperatures 20^oC and 4000^oC and the pressures 10^{-12} bar and 1000 bar, all of the phases of Fe are expressed. For different regions of this range of temperatures and pressure, Fe exists as a vapor, liquid, and solid. The temperature and pressure ranges of each phase are displayed in the phase diagram shown in Figure (2.12). While Fe can exist as either a vapor or liquid for various temperatures and pressures, for the work covered in this dissertation, we were interested in tuning the properties of the material by forcing the material to condense onto a substrate. Consequently, the samples studied in this dissertation were solid. It is clear from Figure (2.12) that for temperatures below 1538^oC, there are three solid allotropes which exist for different temperature and pressure ranges. Below 500^oC and 1000 bar, the stable allotrope is α-Fe. The unit cell of this allotrope is bcc with a lattice constant of 2.87Åat RT. Since the Curie temperature (T_c) of Fe is 770^oC, the ferromagnetic

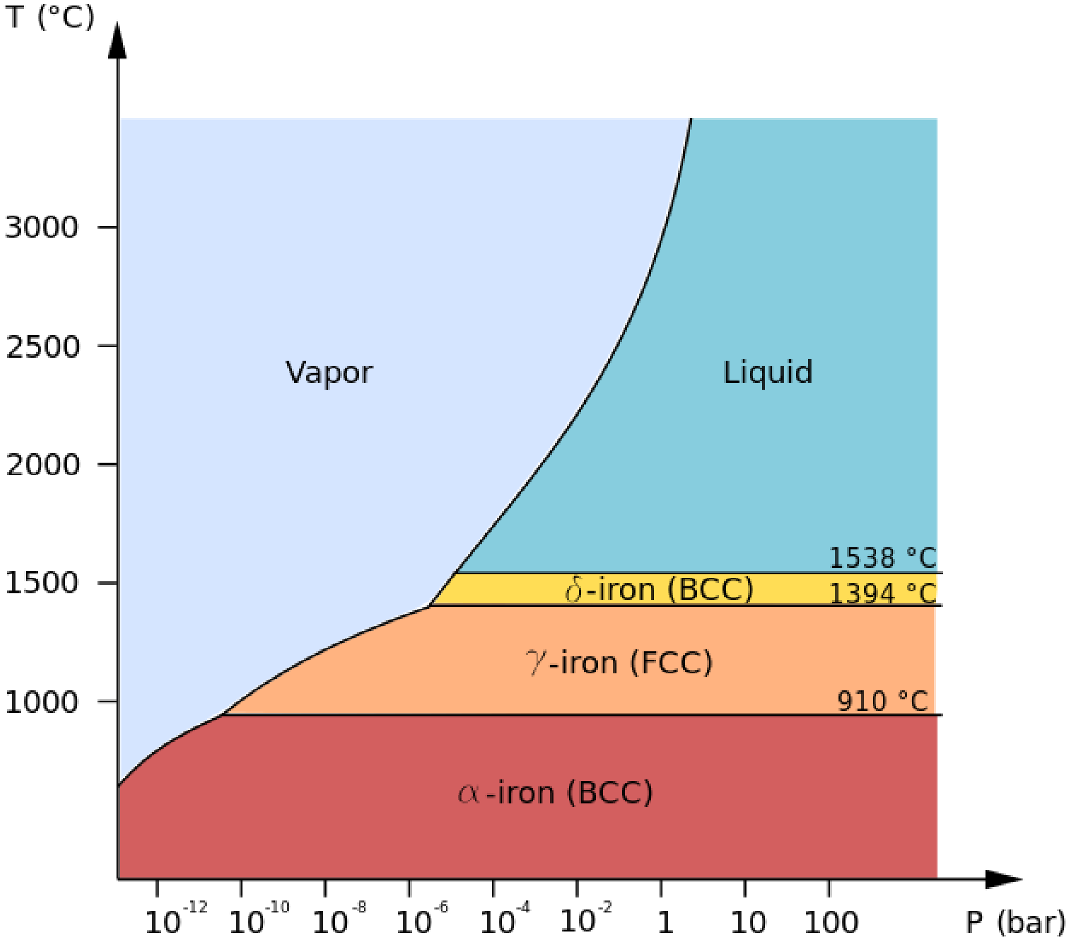

Figure 2.12: Phase diagram of Fe*Smith* (1995)

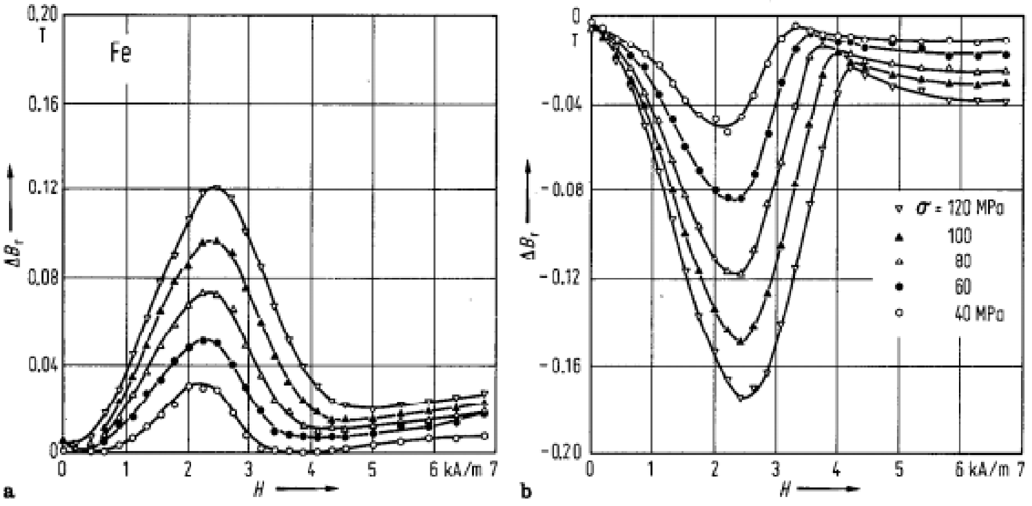

Figure 2.13: Reversible part of the magnetic flux density ($\Delta \mathbf{B_r}$) v. H curve for different values of stress (σ) applied sinusoidally, a. tensile region of sinusoid, b. compression region of sinusoid. *Wijn* (1997)

transition occurs in this temperature region *Yousuf et al.* (1986). Below this temperature, α-Fe exhibits ferromagnetic order, while above this transition temperature the material is paramagnetic. This phase exists for various pressures up to 910^{o}C. Above this temperature at a pressure of 10^{-10} bar, the stable allotrope is γ-Fe which has a unit cell that is fcc.The unit cell of γ-Fe is 3.63 Å. For pressures above 10^{-5} bar and between the temperatures 1394^{o}C and 1538^{o}C, the stable allotrope is δ-Fe. The structure of the unit cell of this allotrope is bcc. At the temperature, 1425 ^{o}C, the lattice constant of this allotrope was measured to be 2.93 Å. Since we were interested in the properties of the ferromagnet, and because α-Fe is better lattice-matched with $BaTiO_3$ when rotated by 45^o, our desired allotrope for the film of the Fe/$BaTiO_3$ samples studied in this dissertation were α-Fe. Since the measurements conducted during these studies were obtained at temperatures that did not exceed 200^{o}C, we can assume that the material was ferromagnetic during all of the measurements. This was confirmed experimentally. The bulk modulus which describes the structural response of a material to changes in pressure was measured to be 168 GPa,*Kittel* (2005). As was mentioned in Section (2.3.2), the magnetism of the α-Fe phase is coupled to the bcc lattice due to spin-orbit (SO). As a result, α-Fe exhibits both magnetocrystalline anisotropy and magnetostriction. These properties of Fe will be discussed during the remainder of this subsection.

The magnetocrystalline anisotropy constant of α-Fe is $4.8\times10^{-5}\frac{erg}{cm^3}$, *Gijs et al.* (1997). Since the crystal lattice distorts in response to external pressure, the magnetocrystalline anisotropy of the material also changes. This variation in the magnetocrystalline anisotropy, K_1, with external pressure, p, can be described by the following parameter:

$$K_1^{-1}\frac{dK_1}{dp} = 40 \times 10^{-12}\ \mathbf{Pa}^{-1}\, \textit{Wijn}\ (1997) \tag{2.88}$$

As was mentioned in Section (2.3.2), the magnitude of the anisotropy coefficient along a specific axis is related to the free energy of the spins while aligned along that axis. Changes in these coefficients can result in a rotation of the ground state of the magnetization relative to this axis. By extension, the change in these coefficients is correlated to the magnetostriction of the material, which relates the magnetization along a specific axis to the stress applied to this axis. If the anisotropy coefficient increases, the free energy of the spin orientation will increase as the lattice is changed. As a result, the spins can rotate to another axis with a smaller anisotropy coefficient. This coupling between the magnetization and the crystal lattice described in terms of the length of the material along a specific axis, l, and the **H** applied along the axis is described by the magnetostriction coefficient, λ. The magnetostriction exhibited by α-Fe is demonstrated in Figure (2.13). In this figure, the reversible magnetic flux density ($\Delta\mathbf{B}$) is plotted relative to the applied field strength (**H**). During each measurement, an external stress (σ) was applied to the sample. In Figure (2.13) the $\Delta\mathbf{B}$ v. **H** plots for different values of σ are displayed. For this measurement, the stress applied to the bulk material was sinusoidal. Figure (2.13a) and Figure (2.13b) display the dependence of $\boldsymbol{\Delta}\mathbf{B}_r$ on **H** during the portion of the stress sinusoid that resulted in tensile stress and compressive stress, respectively. The difference in the magnitudes of $\Delta\mathbf{B}$ of the curves of equivalent stress in Figures (2.13a) and Figures (2.13b) suggests hysteresis in the stress response of bulk Fe. The magnetostriction of α-Fe can be described, generally, by the following magnetostriction coefficients, λ:

$$\begin{aligned} \lambda_{100} &= 15 \times 10^{-6} \\ \lambda_{111} &= -21 \times 10^{-6} \\ \lambda_{s} &= 7 \times 10^{-6} \end{aligned} \tag{2.89}$$

where $\lambda_{xyz} = \frac{\Delta l_{xyz}}{\Delta \mathbf{H}}$ and λ_s is the isotropic average of the magnetostriction along the <100> and <111> directions, which can be described by the following equation:

$$\lambda_s = \frac{2}{5}\lambda_{100} + \frac{3}{5}\lambda_{111} \tag{2.90}$$

In this subsection of the dissertation, the structural and magnetic properties of bulk Fe were discussed along with magnetoelastic coupling of the material. Since this work, also focused on Fe,Pd alloys, the magnetic and structural properties of these alloys will also be discussed.

2.4.2 Palladum-Iron Alloys

Depending on the concentration of Fe and Pd in an Fe_xPd_{100-x} alloy, the structural and magnetic properties vary widely. The phase diagram of Fe_xPd_{100-x} alloys in bulk is displayed in Figure (2.14). It is clear from Figure (2.14) that $Fe_{100-x}Pd_x$ has several phases. It is also evident that for temperatures above 912^{o}C, the stable phase of $Fe_{100-x}Pd_x$ are γ-Fe and Pd, which both have conventional unit cells that are fcc. The lattice constant of this unit cell is 3.65Å. As was mentioned in Chapter (I), the objective of this work was to observe the effect of strain induced by the substrate on a deposited film. In order to accurately characterize the effect of the substrate-

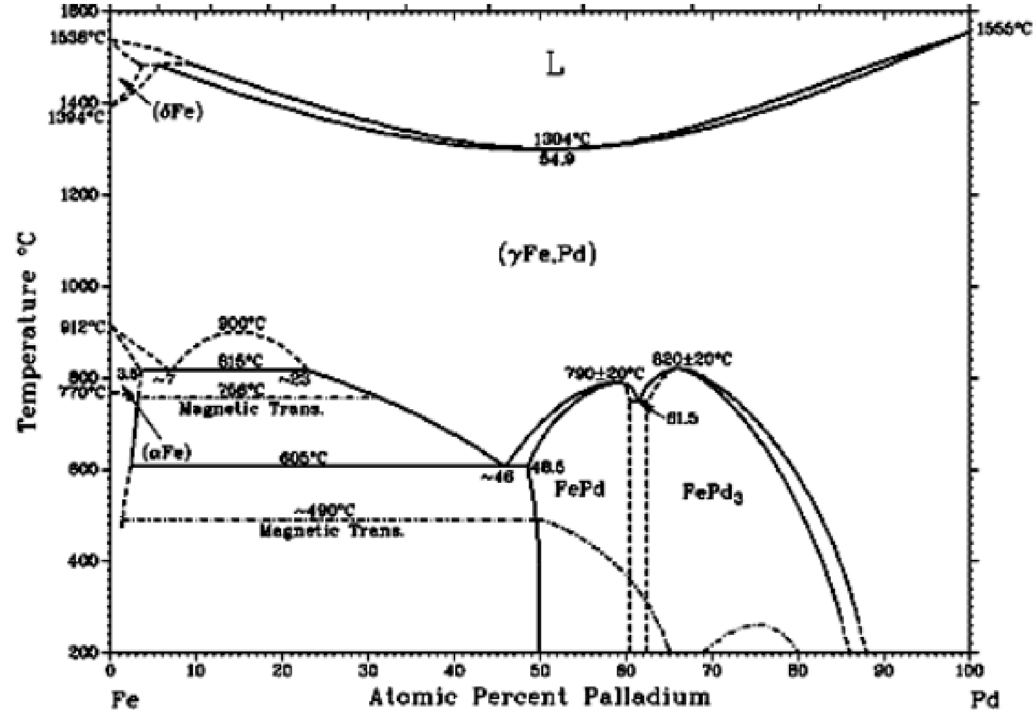

Figure 2.14: Phase diagram of $Fe_{100-x}Pd_x$ alloys[*Okamoto* (1992)]

induced strain on the deposited film, we were interested in using an ordered film. Since L1$_0$-Fe$_{50}$Pd$_{50}$ and L1$_2$-FePd$_3$ both exhibit structural and chemical order, these phases were chosen for our study. The magnetic and structural properties of these phases will now be discussed.

Using Figure (2.14), it is clear that the Fe$_{50}$Pd$_{50}$ phase is stable for temperatures below 800^{o}C and for Pd concentrations between 50% and 60% Pd. At each Fe$_{100-x}$Pd$_x$ composition within this range, the structure of the FePd unit cell is structurally ordered. However, at exactly Fe$_{50}$Pd$_{50}$, the L1$_0$-FePd phase is observed, which is both structurally and chemically ordered. A schematic diagram of the conventional unit cell is displayed in Figure (2.8). The conventional unit cell can be described by a simple cubic (sc) Bravais lattice with the following 4 atom basis:

$$\begin{aligned}
\mathrm{Fe}(1) &: 0\hat{\mathbf{x}} + 0\hat{\mathbf{y}} + 0\hat{\mathbf{z}} \\
\mathrm{Fe}(2) &: 0\hat{\mathbf{x}} + \frac{1}{2}\hat{\mathbf{y}} + \frac{1}{2}\hat{\mathbf{z}} \\
\mathrm{Pd}(1) &: \frac{1}{2}\hat{\mathbf{x}} + 0\hat{\mathbf{y}} + 0\hat{\mathbf{z}} \\
\mathrm{Pd}(2) &: \frac{1}{2}\hat{\mathbf{x}} + \frac{1}{2}\hat{\mathbf{y}} + 0\hat{\mathbf{z}}
\end{aligned} \tag{2.91}$$

2 Fe ions and 2 Pd ions. The lattice constant of the sc Bravais lattice is 3.85Å. This material exhibits ferromagnetic order with a Curie temperature, T$_C$, of 446.85^{o}C. One important physical characteristic of this phase is its large magnetostriction. The in-plane magnetostriction ($\lambda_{||}$) is as large as 200 ppm in sputtered Fe$_{50}$Pd$_{50}$ thin films deposited on a substrate maintained 473 K *Wunderlich et al.* (2009).

Returning to Figure (2.14), the structurally ordered FePd$_3$ phase is observed for Pd compositions between 65 % to 87 %. At the exact composition, Fe$_{30}$Pd$_{70}$, the L1$_2$-FePd$_3$ phase is observed. The conventional unit cell of the L1$_2$-FePd$_3$ phase can be described using an sc Bravais lattice with a lattice constant, a=3.848Å, and a 4 atom basis described by the following position vectors:

$$\begin{aligned} \mathrm{Fe}(1) &: 0\hat{\mathbf{x}} + 0\hat{\mathbf{y}} + 0\hat{\mathbf{z}} \\ \mathrm{Pd}(1) &: \frac{1}{2}\hat{\mathbf{x}} + \frac{1}{2}\hat{\mathbf{y}} \\ \mathrm{Pd}(2) &: \frac{1}{2}\hat{\mathbf{x}} + \frac{1}{2}\hat{\mathbf{z}} \\ \mathrm{Pd}(3) &: \frac{1}{2}\hat{\mathbf{y}} + \frac{1}{2}\hat{\mathbf{z}} \end{aligned} \tag{2.92}$$

Similar to $L1_0$-FePd, this phase is both structurally and chemically ordered. For the surrounding compositions, some of the atomic sites of the chemically ordered phase are replaced with either Fe or Pd ions depending on whether x is larger or smaller than 30. For compositions where $x>30$, the Pd atomic sites are replaced with Fe ions, the converse is true for compositions where $x<30$. The T_C of this ordered phase is 225^oC. For alloys with Pd concentrations between 84% and 90%, the T_C decreases linearly. However, since the dependence of T_C on Pd concentration can more accurately be approximated by a negative parabola, with its vertex positioned at $\sim$ 77% Pd, for Pd concentrations <77%, the non-zero curvature of the parabola must be considered and the rate of change of T_C decreases as the concentration approaches 77% Pd.

Returning to the magnetostriction of the $Fe_{100-x}Pd_x$, the concentration dependence of the linear magnetostriction of $Fe_{100-x}Pd_x$ annealed alloys is displayed in Figure(2.15). A maximum in the linear magnetostriction occurs at 40 % Pd. After reaching this maximum value, λ decreases to zero at 60% Pd. According to these results, there should be no magnetic response to strain in $FePd_3$. However, pressure-induced invar behavior has been observed in bulk $FePd_3$, *Winterrose et al.* (2009). The temperature-invariant volume of invar alloys can be described by the increase in the population of the Low Spin state due to thermal fluctuations. This state has a lower magnetization and smaller volume than the ferromagnetic state, the occupation of this LS state as the temperature increases effectively cancels out the effect of

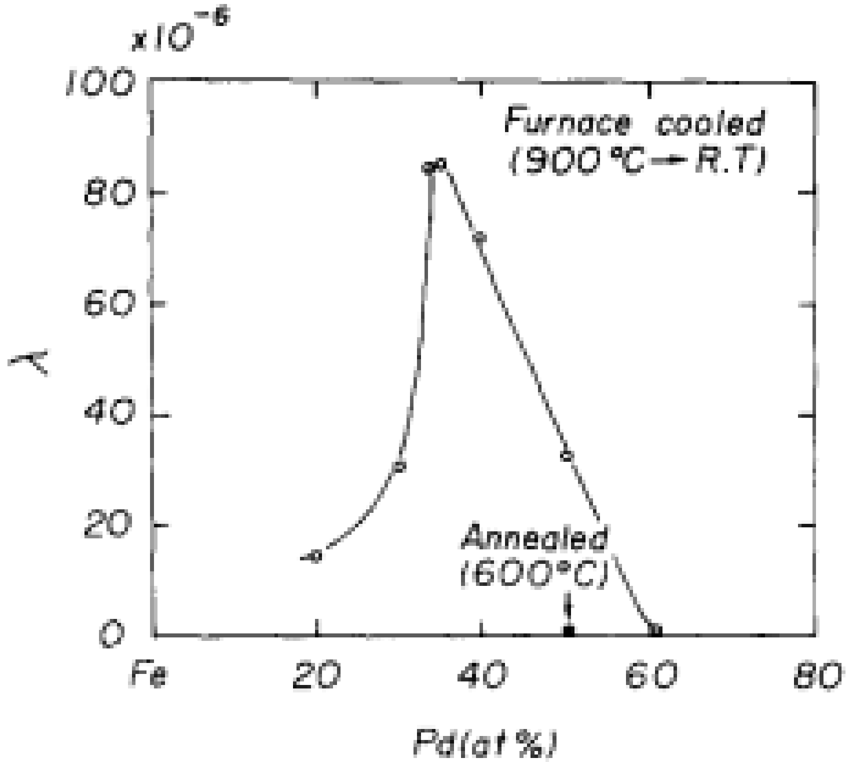

Figure 2.15: Linear magnetostriction (λ) of bulk $\mathrm{Fe}_{100-x}\mathrm{Pd}_x$ alloys that were annealed at 900^{o}C and subsequently furnace cooled to RT.*Fukamichi* (1979)

thermal expansion as the temperature of the material is increased *Winterrose et al.* (2009). Since the two nearly degenerate states each have an associated magnetization and volume, the increase in the population of the LS state, also results in a change in the magnetic state of the material. It is in this manner that the magnetization and the elastic state of the material are coupled. This behavior suggests that as an external pressure is applied to the FePd_3 lattice, the $|\lambda|_0$ increases. This variation in λ_0 could result in a deviation from the behavior described in Figure (2.15) for the $\mathrm{L1}_2$-FePd_3 ($\mathrm{Fe}_{30}\mathrm{Pd}_{70}$) phase. This effect will be explored in the *Elastic Control of* Fe_16Pd_{84} experiments.

2.5 Properties of perovskites: $SrTiO_3$ and $BaTiO_3$

2.5.1 Crystalline structure of perovskites and ferroelectrics

Ferroelectrics are defined by their spontaneous electric polarization. Unlike ferromagnetic materials, the electric polarization of ferroelectrics is caused by structural distortions of the lattice where the net positive charge is separated from the net negative charge, and thus an electric dipole is created. There are several classes of materials that demonstrate this sort of behavior. One such group is the perovskite-oxides with the general chemical formula, ABO_3, where A and B are two cations and O is the O^{-2} anion. $CaTiO_3$, $SrTiO_3$, and $BaTiO_3$ are a few members of this class of materials.

Although these materials have similar chemical formulae, their unit cell structures can vary widely. One source of variation is the difference in the relative sizes of the A and B cations. In its cubic phase, the conventional unit cell of the general ABO_3 structure can be represented using a simple cubic Bravais lattice, with 4 basis atoms. In this structure, the A cation is positioned at the corner of the cube, the Ti^{+4} ion at the body center, and the three O^{-2} ions at the face centers of the cube. When visualizing the unit cell in this way, it is clear that the O^{-2} ions form an octahedron, at the center of which, the Ti^{+4} ion is positioned. Furthermore, the A cations are positioned at the center of the octahedron formed in the space between the O^{-2} octahedra. As a consequence, the structure of the unit cell is affected by the relative sizes of the ionic radii of the A and B ions. If the sizes of the two ions differ greatly, the unit cell will suffer distortion. The proclivity of a material to deviate from this cubic structure can be determined using the Goldschmidt tolerance factor

t, which is described by the following equation:

$$t = \frac{r_A + r_O}{\sqrt{2}(r_B + r_O)} \tag{2.93}$$

where r_A, r_O, and r_B are the ionic radii of atom A, B and O^{-2}, respectively. A schematic drawing of the $SrTiO_3$ conventional unit cell is displayed in Figure (2.16).

When t is equal to 1, $r_A + r_O = r_B + r_O$, and the cubic perovskite structure is favored. When this is the case, there is no distortion. However, if t is far from 1, the cubic structure is not favored. The tolerance ranges are as follows: for values of t between $.9<t<1$, the cubic structure is favored. For values of t that satisfy the condition, $.7<t<.9$, the orthorhombic or rhombohedral structures are favored. For t values greater than 1, the hexagonal structure is favored,*Rabe* (2007). For the experiments described in this dissertation, $SrTiO_3$ and $BaTiO_3$ were used as substrates. The specifics of these perovskite-oxides will be discussed in the following subsections.

2.5.2 Structural and Electrical Properties of Strontium Titanate (STO)

For the sample grown in the *atomic ordering via interdiffusion of Fe/Pd multilayer heterostructure deposited onto $SrTiO_3$* experiment, Strontium Titanate ($SrTiO_3$) (100) was used as a substrate. In this section of the dissertation, the properties of this material will be discussed. $SrTiO_3$, a perovskite, exhibits both a tetragonal and cubic phase.

The lattice constant of these phases are plotted as a function of temperature in Figure(2.17). The T-C transition temperature occurs at -168.15 ^{o}C. Above this temperature, the conventional unit cell of $SrTiO_3$ is cubic with a lattice constant, a_C=3.905. Below the T-C transition temperature, $SrTiO_3$ is in its tetragonal phase, and has lattice constants described by the following list:

$$\begin{aligned} a &= \sqrt{a_{cubic}} \\ c &= 2a_{cubic} \end{aligned} \tag{2.94}$$

From Figure (2.17), it is clear that at RT the cubic structure is favored. This struc-

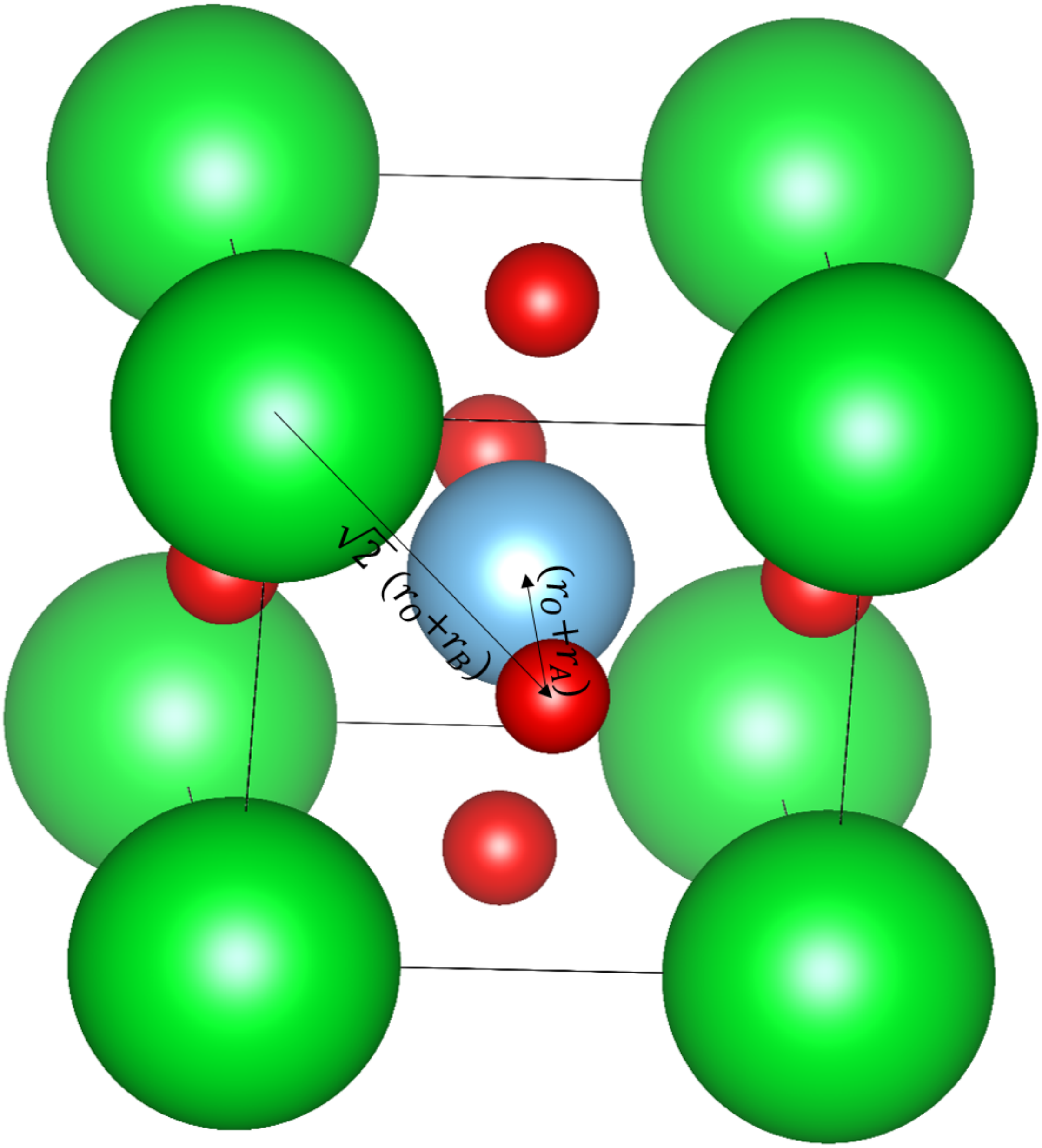

Figure 2.16: Schematic drawing of ABO_3 conventional unit cell

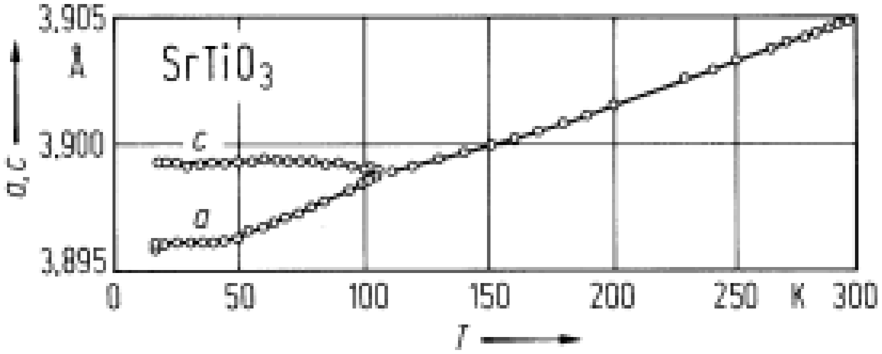

Figure 2.17: Lattice constant of $SrTiO_3$ as a function of temperature*Okazaki and Kawaminami* (1973)

ture can be understood if one uses the Goldschmidt criterion, introduced in Section (2.5.1). Since t is nearly 1, there is minimal structural distortion, which can be accounted for by the rotation and tilting of the O^{-2} octahedra. The substrates used in this experiment were cleaved along the (100) plane. In the cubic phase, the lattice constant, a=3.905Å. The positions of the basis atoms can be described by the following list of vectors:

$$\begin{aligned}\mathbf{r_{Sr}} &= [0,0,0]\\ \mathbf{r_{Ti}} &= [\frac{1}{2},\frac{1}{2},\frac{1}{2}]\\ \mathbf{r_{O_1}} &= [\frac{1}{2},\frac{1}{2},0]\\ \mathbf{r_{O_2}} &= [\frac{1}{2},0,\frac{1}{2}]\\ \mathbf{r_{O_3}} &= [0,\frac{1}{2},\frac{1}{2}]\end{aligned} \tag{2.95}$$

Using the vectors in Equation (2.95), it is clear that the centers of both the positive charges (Ti^4 and Sr^{+2}) and negative charges (O^{-2}) are equivalent and that there is no spontaneous electric dipole moment. Therefore, this phase has no spontaneous electric polarization. For the studies described in this dissertation, the substrate was maintained in the cubic phase.

phase	temparature range (^{o}C)
Rhombohedral(R)	<-75
Orthrhombic (O)	-75<T<18
Tetragonal (T)	18<T<137
Simple Cubic(C)	>137

Table 2.1: $BaTiO_3$ phases

2.5.3 Structural and Electrical Properties of Barium Titanate (BTO)

For the *Elastic Control of the magnetism in Pd,Fe alloys* experiments, $BaTiO_3$ (100) was used as the substrate. In this section, the properties of this material will be discussed.

The perovskite-oxide, $BaTiO_3$, exhibits several structural phases between the temperatures -125^{o}C and 180^{o}C. The observed phases are a rhombohedral (R) phase, an orthorhombic (O) phase, a tetragonal (T) phase, and a cubic (C) phase. The temperature ranges of each phase along with their lattice constants can be found in the $BaTiO_3$ phase diagram displayed in Figure (2.18). For the studies described in this dissertation, the T-C transition was used to impart strain to the deposited film. This transition is highlighted in the figure. Using this diagram, the temperature ranges of each phase can be easily extracted and are displayed in Table (2.1).

It is also important to note that $BaTiO_3$ exhibits structural hysteresis, which is demonstrated near each transition temperature.

Since $BaTiO_3$ is a perovskite-oxide, the analysis of Section (2.5.1) can be used to determine its structure. Using the *lattice with a basis* formalism, the conventional unit cell of $BaTiO_3$ in its cubic (C) phase can be represented using the Bravais lattice of a simple cube with a basis consisting of a Ba^{+2} ion at the corner of the cube, a Ti^{+4} ion at the cube's body center and O^{-2} ions at the face centers. The O^{-2} ions form an octahedron about the Ti^{+4} ion. A schematic drawing of the conventional unit cell in the cubic phase is depicted in Figure (2.19).

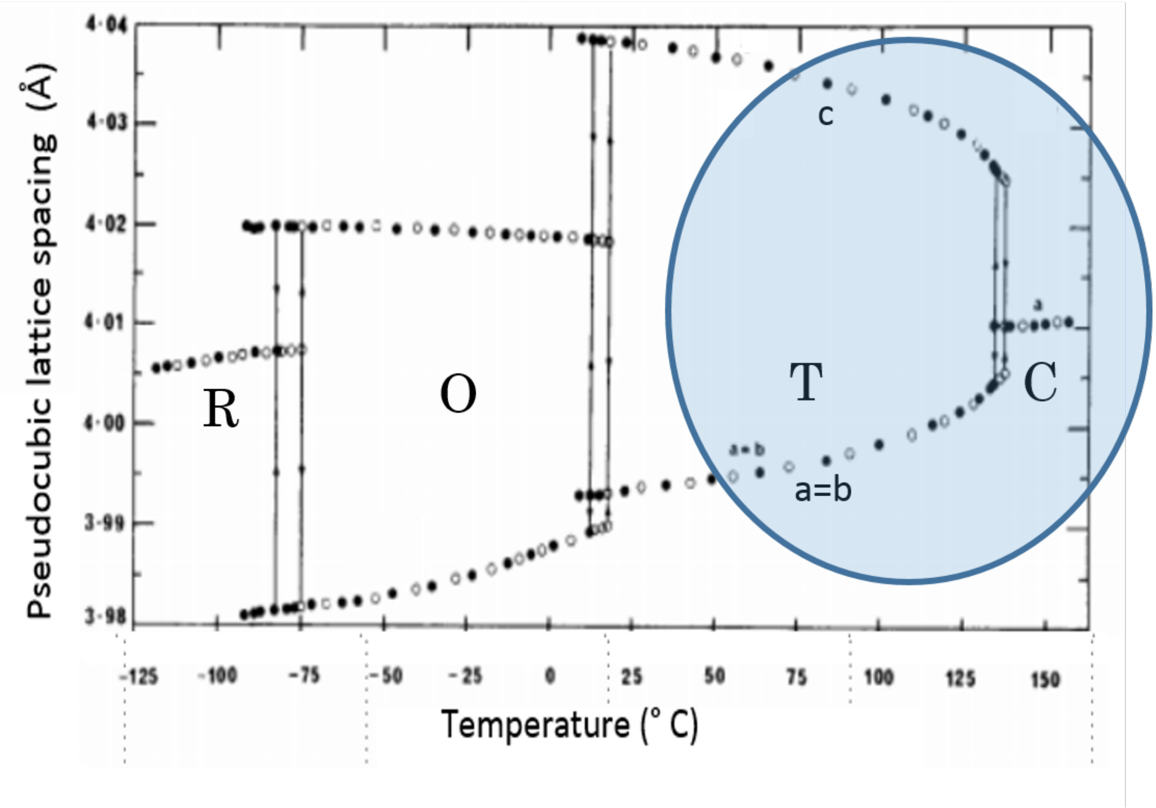

Figure 2.18: Phase Diagram of $BaTiO_3$. *Clarke* (1976)

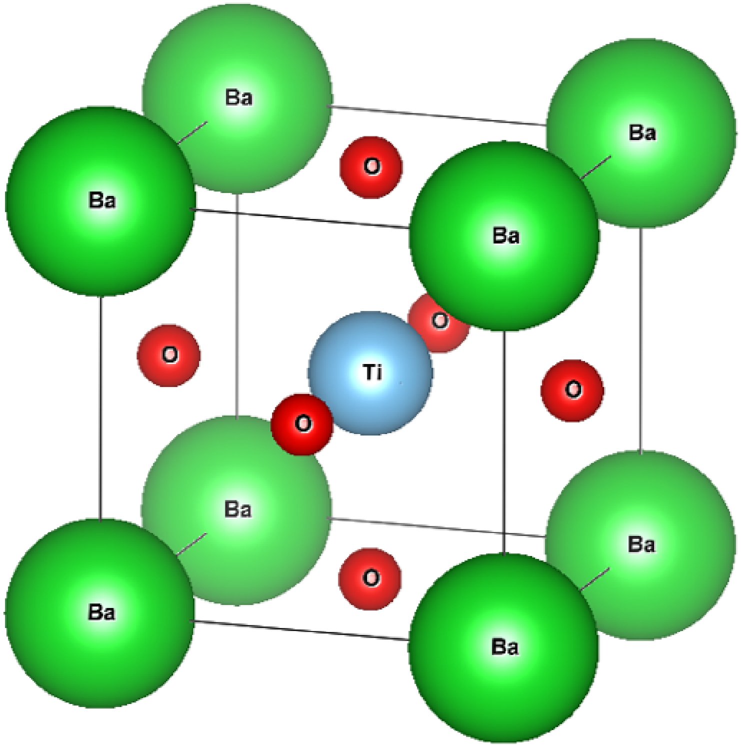

Figure 2.19: Schematic Drawing of conventional unit cell of cubic $BaTiO_3$

In order to determine whether the cubic perovskite structure is favored for $BaTiO_3$ lattice, one can use the Goldschmidt tolerance factor [Section (2.5.1)]. For $BaTiO_3$, t is close to 1. As a result, the cubic-perovskite structure is favored.

The parameters of the Bravais lattice used to describe each phase are described in Table(2.4). The positions of the basis atoms used for each phase are described in Table(2.3). As was mentioned in Section (2.5.1),the spontaneous electric polarization of a ferroelectric material is caused by the displacement of the atoms within the unit cell. It is clear from Figure (2.19) that in the cubic phase (C), there is no separation between the negative and positive charge centers. Consequently, the C phase is paraelectric ($\hat{\mathbf{p}} = 0$). However, each phase below the T-C transition temperature is ferroelectric, with the direction and magnitude of the spontaneous electric polarization, $\hat{\mathbf{p}}$, changing at each structural phase transition. In order to understand the nature of the distortion at each phase, the motion of the basis atoms in each phase

phase	$\mathbf{x_{Ti}, y_{Ti}, z_{Ti}}$	$\mathbf{x_{O_1}, y_{O_1}, z_{O_1}}$
C	[0,0,0]	[0,0,0]
T	$[\frac{1}{2},\frac{1}{2},\frac{1}{2} + \mathbf{\Delta z_{Ti}}]$	$[\frac{1}{2},\frac{1}{2},\mathbf{\Delta z_{O_2}}]$
O	$[\frac{1}{2},0,\frac{1}{2} + \mathbf{\Delta z_{Ti}}]$	$[0,0,\frac{1}{2} + \mathbf{\Delta z_{O_1}}]$
R	$[\frac{1}{2} + \mathbf{\Delta x_{Ti}},\frac{1}{2} + \mathbf{\Delta x_{Ti}},-\frac{1}{2} + \mathbf{\Delta x_{Ti}}]$	$[\frac{1}{2} + \mathbf{\Delta x_{O}},\frac{1}{2} + \mathbf{\Delta x_{O}},\mathbf{\Delta z_{O}}]$

Table 2.2: Initial positions of the basis atoms used in Rietveld Refinement of $BaTiO_3$ XRD data

phase	$\mathbf{x_{O_2}, y_{O_2}, z_{O_2}}$
C	[0,0,0]
T	$[\frac{1}{2},0,\frac{1}{2} + \mathbf{\Delta z_{O_2}}]$
O	$[\frac{1}{2},\frac{1}{4} + \mathbf{\Delta y_{O_2}},\frac{1}{4} + \mathbf{\Delta z_{O_2}}]$
R	N/A

Table 2.3: Initial positions of the basis atoms used in Rietveld Refinement of $BaTiO_3$ XRD data (continued)

have been well studied.

One such study, conducted by Kwei et. al. consisted of conducting powder X-ray diffraction measurements at various temperatures on $BaTiO_3$ *Kwei et al.* (1993). This data was analyzed using Reitveld Refinement to determine the positions of the atom within the unit cell. The results of this analysis suggested that the polarization of each $BaTiO_3$ phase was caused by displacements of both the Ti^{+4} ion and the O^{-2} ions. For the refinement, the initial position of the Ba^{+2} ion was assumed to be [000]. The starting positions of the other basis atoms are described in Table (2.3). The converged atomic displacements can be found in Table (2.4). Using these results, the source of the polarization of each phase will be now be discussed.

phase	a (Å)	b (Å)	c (Å)	$\alpha(^o)$	$\beta(^o)$	$\gamma\ (^o)$	$\hat{\mathbf{p}}$
simple cubic (C)	4.0105	4.0105	4.0105	90	90	90	N/A
tetragonal (T)	3.9935	3.9935	4.0385	90	90	90	[001]
orthorhombic (O)	4.0200	3.9825	4.0200	89.82	90	90	[011]
rhombohedral (R)	4.0065	4.0065	4.0065	89.39	90	90	[111]

Table 2.4: Lattice parameters of $BaTiO_3$

phase	$\mathbf{\Delta x_{Ti}, \Delta y_{Ti}, \Delta z_{Ti}}$	$\mathbf{\Delta x_{O_1}, \Delta y_{O_1}, \Delta z_{O_1}}$	$\mathbf{\Delta x_{O_2}, \Delta y_{O_2}, \Delta z_{O_2}}$
C	[0,0,0]	[0,0,0]	[0,0,0]
T	[0,0,.0224]	[0,0,-.0244]	[0,0,-.0105]
O	[0,0,.0079]	[0,0,.0146]	[0,.0044,-.0189]
R	[-.0107,0,0]	[.0113,0,.0200]	N/A

Table 2.5: Calculated Variations on $\mathbf{r_0}$ of the $BaTiO_3$ basis atoms

The first phase below the **C** phase in temperature, is the tetragonal **T** phase. The a and b lattice constants of the tetragonal phase are 3.99 Å, while the c axis is 4.03 Å. Considering the variation in the lattice constants across the C-T transition, one can view the shift from the cubic phase to the tetragonal phase as the result of an elongation of the unit cell along [001]. From Table (2.3), the assumed initial position of the basis atoms are described by the following list of position vectors:

$$\begin{aligned} \mathbf{r_{Ti}} &= [\frac{1}{2}, \frac{1}{2}, \frac{1}{2}] \\ \mathbf{r_{O_1}} &= [\frac{1}{2}, \frac{1}{2}, 0] \\ \mathbf{r_{O_2}} &= [\frac{1}{2}, 0, \frac{1}{2}] \end{aligned} \tag{2.96}$$

Using Table (2.5), the source of the polarization in the T phase are the following displacements of the basis atoms:

$$\begin{aligned} \mathbf{\Delta r_{Ti}} &= [0, 0, .0224] \\ \mathbf{\Delta r_{O_1}} &= [0, 0, -.0244] \\ \mathbf{\Delta r_{O_2}} &= [0, 0, -.0105] \end{aligned} \tag{2.97}$$

From these results, one can conclude that the Ti^{+4} ion moved upwards while the O^{-2} octahedron moved downwards. The resulting displacement of the positive charges relative to the negatively charged octahedron leads to the formation of a dipole moment,($\mathbf{d}$), within a single unit cell. Summing $\mathbf{d}$ over several unit cells, one finds that this material exhibits an electric polarization, $\hat{\mathbf{p}}$, which points along the $\hat{\mathbf{z}}$

direction.

The next phase following the **T** phase with decreasing temperature is the rhombohedral (**R**) phase. This phase has the following lattice parameters, a=4.005 Åand α=89.85^o [Table(2.4)]. As a result, the **R** phase can be represented as an elongation along the [111] axis. In the **R** phase, the basis only includes 2 atoms, a Ti^{+4} ion and an O^{-2} ion. From Table (2.3),the assumed initial positions of the basis atoms were described by the following position vectors,

$$\begin{aligned} \mathbf{r_{Ti}} &= [\frac{1}{2}, \frac{1}{2}, -\frac{1}{2}] \\ \mathbf{r_{O_1}} &= [\frac{1}{2}, \frac{1}{2}, 0] \end{aligned} \tag{2.98}$$

Using the Table (2.5), the displacements needed for convergence are described by the following set of position vectors:

$$\begin{aligned} \mathbf{\Delta r_{Ti}} &= [-.0107, 0, 0] \\ \mathbf{\Delta r_{O_1}} &= [.0113, 0, .0200] \end{aligned} \tag{2.99}$$

Accordingly, $\hat{\mathbf{p}}$=[111].

The next phase is the orthorhombic phase. The lattice constants of this phase are as follows, a=3.99Å, and b=c=4.02Å, and α= 89.84^o. As a result, the O phase can be represented as an elongation along the [011] axis. In this phase, the basis of the conventional unit cell consists of a Ti^{+4} ion and 2 O^{-2} ions. The calculated displacements that resulted in convergence for this phase suggest that in the orthorhombic phase, $\hat{\mathbf{p}}$=[011].

For the experiments described in this dissertation, the change in the lattice constants across the T-C transition (137^{o}C) was used to impart strain to the deposited film. As a result, only the parameters of the tetragonal and cubic phases are considered in this work.

2.6 Magneto-Optic Kerr Effect (MOKE)

"Simple it may be, but not ineffectual; rude, but not crude." Kerr (1898)

On April 21,1820, while presenting a lecture, Hans Christian Oersted noticed that the direction of a compass' needle seemed to depend on the compass' distance from a wire connected to the poles of a battery. Since the existence of magnetic fields and their effects on magnetic materials was well known, it did not seem unfathomable that the force could be caused by a magnetic field.

Upon further investigation, he was able to conclude that a electric current could produce a magnetic field. With this discovery, Oersted was able to confirm the connection between electric and magnetic fields. Although the coupling of magnetic and electric fields had been proposed several years prior to this observation, this experiment was one of the first demonstrations of this phenomenon. This development led scientists to search for a connection between electromagnetic waves and static fields.

Since it was generally believed that a force imparted by an electric field on a light wave would be larger in magnitude than the force of a static magnetic field, the coupling between an electric field and light was explored first. Unfortunately, the results of these experiments were not promising. Scientists such as Herschel and Faraday conducted experiments exploring the effect of static electric fields on the properties of light, all of which, reported no effect. It was not until 1845, that Faraday investigated the interaction between the magnetic field produced by an electromagnet and the polarization of light transmitted through the magnet's field, that a significant effect was observed. Shortly thereafter, in 1877, Reverend John Kerr reported the change in the polarization of a light beam reflected by an electromagnetic pole. This phenomenon would later be regarded as the Magneto-Optic Kerr Effect (Magneto-Optic Kerr Effect (MOKE)). In 1898, Kerr was awarded the Royal Medal for this result. At the ceremony, it was recorded that Kerr stated while responding to a

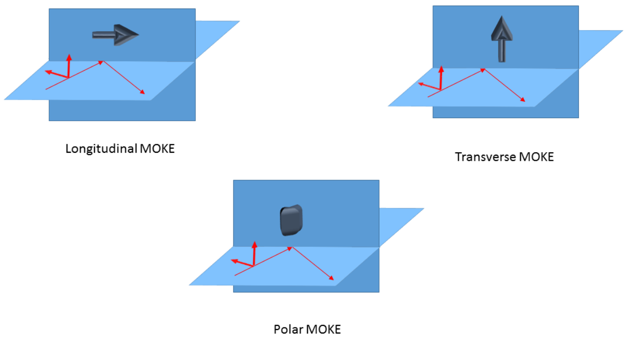

Longitudinal MOKE

Transverse MOKE

Polar MOKE

Figure 2.20: Schematic Drawing of MOKE configurations

question about the simplicity of the MOKE, "Simple it may be, but not ineffectual; rude, but not crude". With this insight, Kerr highlighted the benefits of MOKE magnetometry that have given this effect its staying power. The simplicity of this technique coupled with its sensitivity are the reasons that this effect has maintained relevance and is still regarded as a state of the art technique to indirectly observe the static and dynamic magnetization of thin films. In the remaining portion of this section, the physics of the MOKE will be discussed. *Qiu and Bader* (2000)

Due to the vectorial nature of quantities pertinent to magnetic phenomena, it is important that any technique used to measure magnetism and its effects is capable of measuring both the magnitude and direction of the quantity. The MOKE affords the scientist this capability. Using the MOKE, one can probe the magnetism along three independent axes of the sample, an axis parallel to both the sample plane and the plane of incidence (longitudinal axis), an axis parallel to the sample plane but perpendicular to the plane of incidence (transverse axis), and an axis perpendicular to the sample but parallel to the plane of incidence (polar axis). These measurement axes are displayed in Figure (2.20). MOKE measurements along these different axes are referred to as the longitudinal MOKE, the transverse MOKE, and the polar MOKE, respectively.

When an electromagnetic wave is specularly reflected by an ideal metallic surface, the beam's path upon reflection can be described by the law of reflection which states:

$$\theta_i = \theta_r \tag{2.100}$$

where θ_r and θ_i are the angles of the incident and reflected beams, respectively, relative to the normal of the surface. Assuming that the material does not penetrate the surface of the sample, the other properties of the beam stay the same. One might think that this is true for all materials, and our daily interactions with most materials does not refute this assumption. If one were to examine the properties of light reflected by electrically polarized materials or non-magnetic materials, one would notice very little change in the properties of the reflected beam. However, this is not the case for magnetic materials. After reflection from these materials, there are properties of the reflected beam that depend on the orientation of the magnetization in the magnetic film. Materials where the properties of the incident light and the properties of the material's magnetization are coupled are known as magneto-optic materials. These materials can be described, macroscopically, by examining the dielectric constant of the magneto-optic material, and microscopically, by looking at the spin-orbit coupling of the individual electrons in the material and the incident beam. Upon reflection, spin-orbit coupling between the electric field of the incident beam and the magnetic moments of the electrons alters the polarization of the laser beam. In the laboratory setting, the MOKE allows one to probe the magnetic state of a material by measuring the change of the polarization of the incident EM wave. In this section, the origin of the MOKE and how the effect is used for the work in this dissertation will be discussed. In order to develop an intuition for the MOKE in different magnetic systems, a macroscopic description of the effect will be provided. This description will then be followed by a semi-classical explanation.

In order to understand the MOKE, classically, it is important to remember that the polarization of any EM wave can be described by a unique superposition of orthogonal modes of TEM waves. For this work, the two orthogonal modes can be described by the polarization of the electric wave. The two modes used are one where the electric field polarization is perpendicular to the plane of incidence ($\hat{\mathbf{s}}$-polarized) and one where the electric field polarization is parallel to the plane of incidence (**p**-polarized). Since the linear combination of these two modes can be used to describe any linearly polarized TEM wave, it is useful to derive an equation relating the polarization of the reflected beam and the incident beam for both cases. Using Maxwell's equations which are displayed in the following set of equations:

$$\begin{aligned} \nabla \cdot \mathbf{E} &= \frac{\rho}{\epsilon_0} \\ \nabla \cdot \mathbf{B} &= 0 \\ \nabla \times \mathbf{E} &= -\frac{\partial \mathbf{B}}{\partial t} \\ \nabla \times \mathbf{B} &= \mu_0(\mathbf{J} + \epsilon_0 \frac{\partial \mathbf{E}}{\partial t}) \end{aligned} \tag{2.101}$$

applying these equations at the interface of two dielectric materials, one arrives at the following set of boundary conditions:

$$\begin{aligned} \mathbf{E_i} + \mathbf{E_r} &= \mathbf{E_t} && \textbf{(a)} \\ n_1\mathbf{E_i}\cos(\theta_1) - n_1\mathbf{E_r}\cos(\theta_1) &= n_2\mathbf{E_r}\cos(\theta_2) + n_2\mathbf{E_i}\cos(\theta_2) && \textbf{(b)} \\ \epsilon_1\mathbf{E_i}\sin(\theta_1) + \epsilon_1\mathbf{E_r}\sin(\theta_1) &= \epsilon_2\mathbf{E_t}\sin(\theta_1) && \textbf{(c)} \end{aligned} \tag{2.102}$$

Using Equation (2.102a) to solve for $\mathbf{E_t}$, and inserting the result into Equation (2.102b), results in the following relation between the incident and reflected beam:

$$r_{pp} = \frac{n_t\cos(\theta_i) - n_i\cos(\theta_t)}{n_i\cos(\theta_t) + n_t\cos(\theta_i)} \tag{2.103}$$

For the case where the E-field polarization is perpendicular to the plane of incidence, the equation relating the incident and reflected beam has the following form:

$$r_{ss} = \frac{n_i \cos(\theta_i) - n_i \cos(\theta_t)}{n_i \cos(\theta_i) + n_t \cos(\theta_t)} \tag{2.104}$$

Using these results, for an arbitrary beam incident upon the interface of two dielectric media with refractive indices, n_1 and n_2, the amplitudes of the reflected beam can be described by the following matrix equation:

$$\begin{bmatrix} \mathbf{E_s^r} \\ \mathbf{E_p^r} \end{bmatrix} = \begin{bmatrix} r_{ss} & r_{sp} \\ r_{ps} & r_{pp} \end{bmatrix} \begin{bmatrix} \mathbf{E_s^i} \\ \mathbf{E_p^i} \end{bmatrix} \tag{2.105}$$

For non-magnetic materials, the **s** and **p** are not coupled, as a result the off-diagonal terms, r_{sp} and r_{ps}, are zero. However, in the presence of a magnetic field, the **p** and **s** polarizations are coupled. The classical derivation of this coupling will now be discussed. The electric field of the EM wave exerts a force on the electrons, which can be described using the following equation:

$$\vec{\mathbf{F_e}} = e\vec{\mathbf{E}} \tag{2.106}$$

Modeling the atoms within the magnetic material as an array of classical harmonic oscillators, the motion of a single electron in response to $\mathbf{F_e}$ can be described by the Abraham-Lorentz equation, which can be described by the following equation:

$$m\ddot{\mathbf{x}}(t) + m\gamma\dot{\mathbf{x}}(t) + m\omega_0^2\mathbf{x}(t) = \mathbf{F_{driving}} \tag{2.107}$$

where $\mathbf{x}$ is the distance of the electron from its equilibrium atomic position. The motion of the electron from its equilibrium position in the atom, results in the formation of a dipole moment, **d**. Since the magnetic material consists of an array of atoms, the presence of the EM wave in the material will induce several dipole moments. The sum of each single dipole moment is a macroscopic polarization $\mathcal{P}$ which can be described using the following equation:

$$\mathcal{P}(t) = -Ne\mathbf{x}(t) \tag{2.108}$$

Using Equation (2.108) to solve for $\mathbf{x}(t)$ in terms of $\mathcal{P}$, and inserting the result into Equation (2.107), results in the following equation:

$$\ddot{\mathcal{P}} + \gamma\dot{\mathcal{P}} + \omega_0^2\mathcal{P} = \frac{Ne}{m}\mathbf{F_{driving}} \tag{2.109}$$

In order to determine the driving force, $\mathbf{F_{driving}}$, the properties of the reflecting material must be considered. When the EM wave interacts with the magnetic material, the electrons experience a force from the **E**-field, equal to e**E**. However, since the material is magnetic and there is an applied magnetic field, $\mathbf{B}{=}\mu\mathbf{H}$, the electrons experience a magnetic force which can be described by the following equation:

$$F_B = -e\dot{\mathbf{x}} \times \mathbf{B} = -e\dot{\mathbf{x}} \times \mu\mathbf{H} = -\frac{\dot{\mathcal{P}}}{N} \times \mu\mathbf{H} \tag{2.110}$$

Since the material is composed of polarizable atoms, when the EM wave polarizes the atoms within the material, this polarization results in an **E**-field which then does work on the surrounding atoms. This effect of the polarization on the surrounding atoms can be modeled using a sphere of polarized material. The resulting **E**-field can be described using the following equation:

$$\mathbf{E} = \frac{Ne\mathcal{P}}{3\epsilon_0} \tag{2.111}$$

where $\mathcal{P}_0$ is the polarization of a single atom, N is the number of atoms in the sample, ϵ_0 is electric permittivity of vacuum. The associated driving force, $\mathbf{F_{driving}}$, is described by the following expression:

$$\mathbf{F}_{\mathbf{driving}} = \frac{e}{m}\frac{Ne\mathcal{P}}{3\epsilon_0} \tag{2.112}$$

As a result, $\mathbf{F}_{\mathbf{driving}}$ is described by the following expression:

$$\mathbf{F}_{\mathbf{driving}} = e\mathbf{E}(t) - \frac{\mu}{Ne}\dot{\mathcal{P}} \times \mathbf{H} + \frac{e}{m}\frac{Ne\mathcal{P}}{3\epsilon_0} + \frac{Ne^2}{3\epsilon_0 m}\mathcal{P} \tag{2.113}$$

Inserting Equation (2.113) into Equation (2.109) results in the following expression:

$$\ddot{\mathcal{P}} + \gamma\dot{\mathcal{P}} + \omega_0^2\mathcal{P} - \frac{e}{m}\frac{Ne\mathcal{P}}{3\epsilon_0} = \frac{e\mathbf{E}Nq}{m} - \frac{e\mu}{m}\dot{\mathcal{P}} \times \mathbf{H} \tag{2.114}$$

Assuming $\mathbf{E}(t)$ is sinusoidal, it can be represented by the following complex exponential:

$$\mathbf{E}(t) = \mathbf{Re}[\mathbf{E}_0 e^{i\omega t} + \text{c.c.}] \tag{2.115}$$

Since the polarization $\mathcal{P}$ is a response to the $\mathbf{E}$(t) of the EM wave, one can assume that the polarization should have the same frequency and only differ in phase, ϕ.

$$\mathcal{P}(t) = \mathbf{Re}[\mathcal{P}(\omega)e^{i\omega t} + \text{c.c.}] \tag{2.116}$$

Inserting $\mathcal{P}(t)$ from Equation (2.116), results in the following equation of motion:

$$(-\omega^2 + i\omega\gamma + \omega_0^2)\mathcal{P} - \frac{e^2}{m}\frac{N\mathcal{P}}{3\epsilon_0} = \frac{Ne^2\mathbf{E}(t)}{m} - \frac{e\mu\omega}{m}\mathcal{P} \times \mathbf{H} \tag{2.117}$$

In the remainder of this subsection, Equation (2.117) will be applied to each of the three MOKE configurations, transverse, longitudinal, and polar.= We will begin with the transverse MOKE configuration.

2.6.0.1 Transverse MOKE effect

In the transverse case,

$$\mathbf{E^i} = \begin{bmatrix} \mathbf{E^i_s} \\ \mathbf{E^i_p} \\ 0 \end{bmatrix}, \mathbf{H} = \begin{bmatrix} 0 \\ \mathbf{H} \\ 0 \end{bmatrix} \tag{2.118}$$

Inserting these vectors into Equation (2.117),

$$\xi \begin{bmatrix} \mathbf{P_P} \\ \mathbf{P_s} \\ \mathbf{P_d} \end{bmatrix} = \frac{Ne^2}{m} \begin{bmatrix} \mathbf{E^i_p} \\ \mathbf{E^i_s} \\ \mathbf{E^i_d} \end{bmatrix} - i\beta \begin{bmatrix} -\mathbf{P_d} \\ 0 \\ \mathbf{P_p} \end{bmatrix} \mathbf{H} \tag{2.119}$$

$$\begin{aligned} \xi\mathbf{P_p} &= \frac{Ne^2}{m}\mathbf{E^i_p} + i\beta\mathbf{P_d}\mathbf{H} \quad &\textbf{(a)} \\ \xi\mathbf{P_s} &= \frac{Ne^2}{m}\mathbf{E^i_s} &\textbf{(b)} \\ \xi\mathbf{P_d} &= \frac{Ne^2}{m}\mathbf{E^i_d} - i\beta\mathbf{P_p}\mathbf{H} \quad &\textbf{(c)} \end{aligned} \tag{2.120}$$

where $\xi = -\omega^2 + i\omega\gamma + \omega_0^2$. Substituting the variable:$\Psi = \frac{\beta\mathbf{H}}{\xi}$ into the Equation (2.120). Inserting Equation (2.120a) into Equation (2.120c) results in the following equation,

$$\mathcal{P}_d = \frac{Ne^2}{m\xi}\mathbf{E^i_d} - i\frac{Ne^2}{m\xi}\Psi\mathbf{E_p} \tag{2.121}$$

Since $\mathbf{E^i_d} = 0$, Equation (2.121) can be simplified to the following equation:

$$\mathcal{P}_d = -i\frac{Ne^2}{m\xi}\Psi\mathbf{E_p} \tag{2.122}$$

In Equation (2.122) only terms to first order in **H** were included. Equation (2.121) can be interpreted as the electric field parallel to the plane incidence, $\mathbf{E_p}$ causes a polarization along the propagation direction (**d**) of the incident beam. This coupling can be understood using the Lorentz equation, which can be described by the following equation:

$$\vec{F}_e = -e\vec{E} - e\vec{v} \times \vec{B} \tag{2.123}$$

Using Equation (2.123), the $\hat{\mathbf{p}}$ component of the incident electric field applies an electric force on the electrons that points in the opposite direction of the **E**-field. The motion of the electrons can be described by the velocity **v**. Since the polarization of the incident EM wave, $\mathbf{E^i}$, has components in only the $\hat{\mathbf{p}}$ and $\hat{\mathbf{s}}$ direction the only non-zero component of the applied magnetic field is along the $\hat{\mathbf{s}}$ direction. If one uses Equation (2.123) to determine the $\mathbf{F_B}$ on the electrons, the result is the following set of equations:

$$\mathbf{F_B} = q\mathbf{v} \times \mathbf{B} = q \begin{vmatrix} \hat{\mathbf{p}} & \hat{\mathbf{s}} & \hat{\mathbf{d}} \\ \mathbf{v_p} & \mathbf{v_s} & 0 \\ 0 & \mathbf{B_s} & 0 \end{vmatrix} = |\mathbf{v_p}||\mathbf{B_s}|\hat{\mathbf{d}} \tag{2.124}$$

Since $\mathbf{F_B}$ points along the $\hat{\mathbf{d}}$, the electrons move along the $\hat{\mathbf{d}}$ direction. Although this motion was caused by a magnetic field, the same motion would result from an electric field pointing in the $\hat{\mathbf{d}}$ direction. The electric polarization of a material can be described in terms of an electric field using the following relation:

$$\mathcal{P}_i = \epsilon_0 \alpha_{ij} \mathbf{E}_j \tag{2.125}$$

where α_{ij} is the polarizability tensor which has the following form:

$$\alpha \equiv \begin{bmatrix} \alpha_{pp} & \alpha_{ps} & \alpha_{pd} \\ \alpha_{sp} & \alpha_{ss} & \alpha_{sd} \\ \alpha_{dp} & \alpha_{ds} & \alpha_{dd} \end{bmatrix} \tag{2.126}$$

Applying Equation (2.125) to Equation (2.122), the $\mathcal{P}_d$ can be described in terms of an electric field by the following relation:

$$\mathcal{P}_d = \epsilon_0 \alpha_{dd} \mathbf{E'_d} \tag{2.127}$$

Applying Equation (2.125) to the equations of Equation (2.120), one finds that in the transverse configuration, α_{ij} has the following form:

$$\alpha = \begin{bmatrix} \frac{Ne^2}{m\xi} & 0 & i\frac{Ne^2}{m\xi^2}\beta|\mathbf{H}| \\ 0 & \frac{Ne^2}{m\xi} & 0 \\ -i\frac{Ne^2}{m\xi^2}\beta|\mathbf{H}| & 0 & \frac{Ne^2}{m\xi} \end{bmatrix} \tag{2.128}$$

The electric polarizability (α_{ij}) can be related to the dielectric tensor (ϵ_{ij}) using the following relation:

$$\epsilon_{ij} = \mathcal{I} + \alpha_{ij} \tag{2.129}$$

where $\mathcal{I}$ is the identity matrix. Using this equation, ϵ_{ij} can be described by the following equation:

$$\epsilon = \begin{bmatrix} 1 + \frac{Ne^2}{m\xi} & 0 & i\frac{Ne^2}{m\xi^2}\beta|\mathbf{H}| \\ 0 & 1 + \frac{Ne^2}{m\xi} & 0 \\ -i\frac{Ne^2}{m\xi^2}\beta|\mathbf{H}| & 0 & 1 + \frac{Ne^2}{m\xi} \end{bmatrix} \tag{2.130}$$

The refractive index η can be determined using the following equation:

$$\eta^2 \mathbf{E_j} - \sum_i \epsilon_{ji} \mathbf{E_i} = 0 \tag{2.131}$$

From Equation (2.131), it is clear that light of different polarization will experience different refractive indices. The refractive indices η_p, η_s, and η_d can be described by the following matrix:

$$\begin{bmatrix} \eta_p^2 \\ \\ \eta_s^2 \\ \\ \eta_d^2 \end{bmatrix} = \begin{bmatrix} (1+\frac{Ne^2}{m\xi}) + i\frac{Ne^2}{m\xi^2}\beta|\mathbf{H}|\frac{|\mathbf{E_d}|}{|\mathbf{E_p}|} \\ \\ 1+\frac{Ne^2}{m\xi} \\ \\ (1+\frac{Ne^2}{m\xi}) - i\frac{Ne^2}{m\xi^2}\beta|\mathbf{H}|\frac{|\mathbf{E_p}|}{|\mathbf{E_d}|} \end{bmatrix} \tag{2.132}$$

From Equation (2.132), it is clear that while η_s remains the same. Since η_p is affected by the $\mathbf{H}$, the component of the electron motion along $\hat{p}$ the $\mathbf{E_p}$ the speed of the electrons will be different.

$$\begin{aligned} \mathrm{r_{pp}} =& r_{pp0} + i\Psi\mathbf{D_1^2}2\eta_1\eta_2\cos(\theta_1)\sin(\theta_2) \\ &+ i\Psi^2[\mathbf{D_1^3}2\eta_1^2\eta_2\cos(\theta_1)\sin^2(\theta_2) \\ &- \mathbf{D_1^2}\eta_1\eta_{2n}\cos(\theta_1)cos(\theta_2)] \end{aligned} \tag{2.133}$$

where n_{2n} is the refractive index of the material in the presence of the applied **H**-field and $\Psi = \frac{\beta H}{\epsilon}$. Since η_s is unchanged by the **H**-field, $\mathbf{r}_{ss}$ remains the same. Consequently, the polarization of an incident EM wave will rotate upon reflection from a magnetized surface. The magnitude of the rotation can be described by the following equation:

$$\begin{aligned} \phi_k =& \tan^{-1}[(\frac{\mathrm{r}_{pp}}{\mathrm{r}_{ss}}) \\ =& \tan^{-1}[\frac{r_{pp0}}{r_{ss0}} + \frac{i\Psi\mathbf{D_1^2}2\eta_1\eta_2\cos(\theta_1)\sin(\theta_2)}{r_{ss0}} \\ &+ \frac{i\Psi^2[\mathbf{D_1^3}2\eta_1^2\eta_2\cos(\theta_1)\sin^2(\theta_2)]}{r_{ss0}} \\ &- \frac{i\Psi^2[\mathbf{D_1^2}\eta_1\eta_{2n}\cos(\theta_1)cos(\theta_2)]}{r_{ss0}}] \end{aligned} \tag{2.134}$$

where $\mathrm{D}_1 \equiv \frac{1}{\eta_1\cos(\theta_2)+\eta_2\cos\theta_1}$. If one only includes terms to first order in H, ϕ_k can be described by the following equation:

$$\begin{aligned}\phi_k &= \phi_0 + \Delta\phi_0 \\ &\sim \tan^{-1}[\frac{r_{pp0}}{r_{ss0}} + \frac{i\Psi D_1^2 2\eta_1\eta_2 \cos\theta_1 \sin\theta_2}{r_{ss0}}] \\ &\sim \frac{r_{pp0}}{r_{ss0}} + \frac{i\Psi D_1^2 2\eta_1\eta_2 \cos\theta_1 \sin\theta_2}{r_{ss0}}\end{aligned} \tag{2.135}$$

In magnetic materials, the field, **B**, that the electrons experience is altered from the **H** by the magnetic moments that are present within the material. As was discussed in Section (2.1), the effect of the magnetic moments on the external field, **H**, will either enhance (diamagnetic) or reduce (paramagnetic) the magnetic field. Consequently, $\Delta\phi_k$ provides information about the **M** of the sample, which is along the dir(**H**), which for this configuration is perpendicular to the plane of incidence. The same analysis can be applied to the longitudinal and polar MOKE configurations. The results are similar, $\Delta\phi_k$ in the longitudinal and polar MOKE configuration, provides information about the **M** parallel to the plane of incidence and perpendicular to the sample, respectively. In the next subsection, the information necessary to understand the MOKE results will be discussed.

2.6.1 MOKE implementation

Heretofore, this section of the dissertation covered the theory behind the MOKE. Although this discussion provided insight that is essential, it is also important to understand how one measures this rotation in the polarization of a beam in the laboratory. In this subsection of the dissertation, the experimental implementation of MOKE will be described along with the ways it is used to determine the magnetic properties of the deposited film.

For the experiments discussed in this dissertation, the MOKE setup consisted of a Helium-Neon laser, an electromagnet, a function generator, a polarizer, an analyzer,

Region	$\hat{\mathbf{H}}$	dir($\mathbf{H}$)	$\hat{\mathbf{M}}$
1	$+\hat{\mathbf{x}}$	$+\hat{\mathbf{x}}$	$+\hat{\mathbf{x}}$
2	$+\hat{\mathbf{x}}$	$-\hat{\mathbf{x}}$	$+\hat{\mathbf{x}}$
3	-$\hat{\mathbf{x}}$	$-\hat{\mathbf{x}}$	$-\hat{\mathbf{x}}$
4	-$\hat{\mathbf{x}}$	$+\hat{\mathbf{x}}$	$\hat{\mathbf{x}}$

Table 2.6: Properties of **M** v. **H** plot of a ferromagnet

and a Data Acquisition Board (DAQ Board). Schematic drawings of the longitudinal (in-plane) and polar (out-of-plane) MOKE configurations are displayed in Figure (3.1) and Figure (3.2), respectively.

For our measurements, the magnetic field was generated using an electromagnet which was connected to a function generator whose output voltage was a sinusoid. The sample was placed in between the poles of the electromagnet. The source of the EM wave was a polarized HeNe laser. Before reaching the sample surface, the laser beam was sent through a polarizer which was aligned such that the output beam was s-polarized. The reflected beam was then sent through another polarizer, an analyzer, which was aligned so that its polarization axis was cross-aligned with the original polarizer. In this configuration, any change in the intensity of the output signal of the analyzer is caused by the rotation of the beam. For a magnetic material with no spontaneous magnetization, the magnetic spins either follow or oppose the applied field depending on the nature of the magnetism of the material. It is important to note that for these materials, in the absence of an applied field there is no remnant magnetization. The **M** v. **H** plot for these materials looks similar to Figure. However, for a material with a spontaneous magnetization, a ferromagnet, in the absence of an applied field a magnetization still exists. This magnetization continues to persist even after the magnetic field has switched directions. This behavior is present in the $\mathbf{M}(\mathbf{H})$ v. **H** curve displayed in Figure (2.21) and is highlighted in Table (2.6). It is clear from both the Figure (2.21) and the Table (2.6) that the direction of the magnetization depends on the path of the **H**-field. This behavior describes hysteresis. The hysteresis

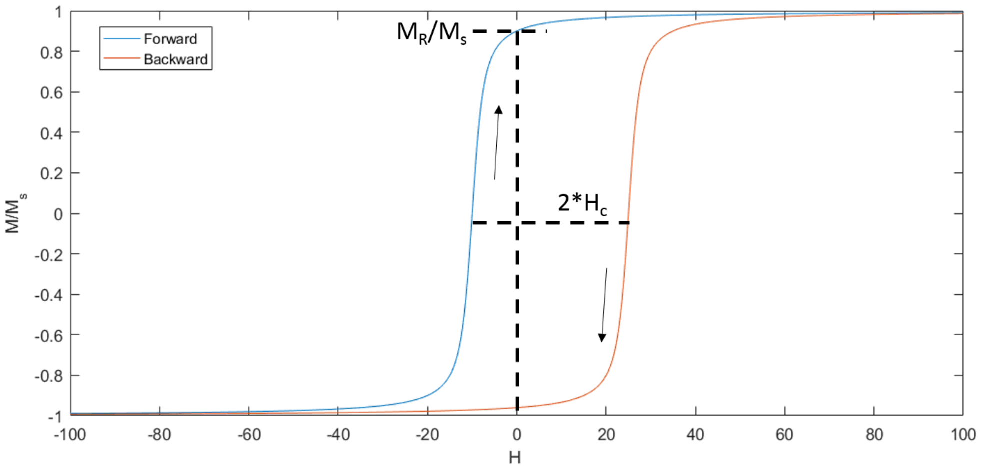

Figure 2.21: Hysteresis loop with highlighted parameters

loop can be broken into four regions that are highlighted in Table (2.6).The hysteretic behavior is captured in Regions 2 and 4 where the direction of $\mathbf{H}$ and the $\hat{\mathbf{M}}$ are in opposite directions. In this region, the magnetic spins respond to the change $\mathbf{H}$, by forming domain walls. This process is reversible. In regions 1 and 3, the path of the magnetization is reversible. In these regions, the magnetization respond to the changing $\mathbf{H}$ through coherent rotation, which is reversible. In Section (2.4.1) of this dissertation, this reversible portion of the loop is referred to as $\mathbf{B_R}$. $\Delta\mathbf{B_R}$ is the difference between the $\mathbf{M}$ in Regions 1 and 3.

Focusing on the properties of the irreversible portion of the loop, the height of the loop at $\mathbf{H=0}$ is referred to as the remnant magnetization ($\mathbf{M}_R$), while the coercive field (H_c)is determined to be half way between the values of the positive and negative switching $\mathbf{H}$ fields. In Figure (2.21), the hysteresis is centered about $\mathbf{H}$=0, which means that the switching of the spins occurs at -$|\mathbf{H_s}|$ and $|\mathbf{H_s}|$. However, there are certain materials where the average of the $|\mathbf{H_s}|$ and -$|\mathbf{H_s}|$ is not zero, but a shifted value. The source of this shift is called an exchange bias. The physical phenomenon responsible for this shift of the hysteresis loop will be discussed in the remainder of this section.

Prior to this point in this section of the dissertation, the response of a ferromagnet to an external **H**-field has been discussed. From this earlier discussion, it is clear that the presence of the spontaneous magnetization of the ferromagnet results in hysteretic behavior, that is centered about the point where **H** is zero. However this behavior changes when the ferromagnet is in contact with an anti-ferromagnet. Similar to a ferromagnet, an Anti-ferromagnet is defined by its magnetic state which consists of magnetic spins that are anti-parallel. The result are planes of parallel magnetic spins that have opposite polarization to the parallel spins of the neighboring plane. At an AFM/FM interface, below the ordering temperature of the AFM, the spins at the interface align parallel to the spins in the FM, in order to minimize the energy due to the exchange interaction between neighboring spins. However, the orientation of the spins within the planes of the AFM that are not at the interface alternate in their orientation. When the **H**-field is applied, the spins within the FM rotate due to the Zeeman interaction. Meanwhile, the spins within the AFM remain roughly unchanged. At the interface, the spins of the FM experience a torque from the spins within the AFM due to the exchange interaction which has a minimum value when the spins are aligned. As a result, the **H** necessary to rotate the spins is increased. Since, the AFM spins remain in their original configuration, the effect is unidirectional. Consequently, the center of the loop shifts from zero. This shift is called the exchange bias. This effect will be important for the work described in this dissertation. due to the effect of the exchange coupling between the spins at the FM/AFM interface, *Nogus and Schuller* (1999).

2.7 Ultra-High Vacuum Deposition (UHV Deposition)

The interactions of interest in this study are magneto-elastic and magneto-electric in nature. Since the magnitude of these couplings depend on the interface between the substrate and the deposited film, it is necessary to minimize inhomogeneities in the deposited film. During UHV deposition, films are deposited with monolayer precision. Such precise control of the film growth coupled with in-situ diffraction techniques (Reflection High-Energy Diffraction (RHEED)) enable one to optimize the quality of the deposited film. For this reason, UHV deposition was used to grow the samples used in this study. However, in order to fully enhance the quality of the films deposited using UHV deposition, it is important to have both an intuition for the physics of the deposited atoms and an understanding of the mechanics of the apparatus. In the rest of this section, both of these topics will be discussed.

During UHV deposition, films are deposited onto a substrate by evaporating elemental materials in a high vacuum chamber(1×10^{-9} torr). As the material evaporates, the vapor coats the chamber surfaces. When a substrate is loaded in the chamber, the vapor condenses on the substrate surface forming a film. As the vapor atoms coat the substrate's surface, they form a spatial configuration that minimizes the free energy of the system. This results in minimizing the interaction of each atom with the other deposited atoms and the neighboring lattice ions of the substrate. Consequently, the substrate's influence on the final film structure is dependent on the thickness of the deposited film. For thin films, the dominant interaction energies are due to the interactions between the few deposited atoms and the lattice ions of the substrate. As a result, the final spatial arrangement of the deposited atoms closely resembles the structure of the substrate with similar in-plane lattice constant and structure. A film with this type of relationship to the substrate is described as epitaxial. If the in-plane lattice constants of the deposited film matches the in-plane lattice constants of the substrate the epitaxial film is also considered to be coherent. As the film thickness grows, the number of deposited atoms increases and the interaction energies between the deposited atoms begins to dominate. Consequently, the atoms arrange themselves to minimize their interaction energies with the neighboring atoms in the deposited film. The crystalline structure (lattice constant and crystal structure) of films of these thicknesses resemble the bulk crystalline structure. These are the two extremes, thin and thick films. One might ask about the intermediate behavior. *What happens when the thickness of the film crosses the "boundary" between thick and thin, such that the arrangement of the atoms no longer depends on the substrate lattice ions and instead depends on the arrangement of the neighboring deposited ions? How does the system of deposited atoms reconcile this shift?* It turns out that the answer is complicated with several variations which will not be discussed in this dissertation. However, to gain an intuition for the deposited film's transition between the "thick" and "thin" regime, we can look at the general behavior of deposited thin film systems. In most cases, the deposited atoms shift their positions relative to the atoms deposited prior to the change, which results in the formation of dislocations. Despite the fact that there are several different classes of dislocations, for our conceptual picture, we can conclude that as the thickness traverses the "thin" to "thick" boundary, there is a shift in the ordering of the newly deposited atoms relative to those already deposited. This change in the position of the atoms minimizes the energy of the system.

Since having a smooth ordered film is important for our studies, it is important that we tune the thickness of the deposited film to ensure that it is thick enough to have detectable magnetization, but also thin enough to be able to form a relatively ordered and smooth film on the substrate with few dislocations. Laying this framework for the ordering of the atoms, we will now discuss the mechanics of the chamber.

During UHV deposition, the pressure in the chamber is maintained at 10^{-9} atm. This low pressure is important for two reasons. It ensures that there are no contaminates on the film surface. Also, it minimizes the collisions between the vaporized atoms in the chamber, thereby maximizing their mean free path. This uninterrupted trajectory ensures a continuous film deposition rate. One can understand this correlation by considering the specifics of the UHV chamber.

During growth, a substrate is mounted with its surface plane parallel to the base of the chamber. Once a substrate is loaded, elemental metals placed in Boron Nitride crucibles in Knudsen cells located at the bottom of the chamber are resistively heated above their boiling point by a wire filament that wraps around the outer rim of the cell. In order to minimize the amount of heat dissipated by the effusion cells, a tantalum shield is placed around the filament. As mentioned earlier, once the vapor reaches the substrate surface, it condenses into a film on the surface of the substrate. If a constant rate of deposition is assumed and maintained, the thickness of the deposited film can be determined using the constant deposition rate and the duration of the substrate's exposure to the vapor. In order to ensure a constant deposition rate, the particle speed and trajectory of the vapor atoms between the effusion cell and the substrate must remain roughly constant. Accordingly, the amount of particle collisions in the chamber must be minimized. Since the working UHV chamber pressure (10^{-10} atm) is well below the Knudsen limit for the walls of the chamber (10^{-5}), we were able to assume that the vaporized atoms suffer no collisions on their path to the substrate. As a result, we can assume that the flux rate of the vapor is roughly constant which allows us to relate the substrate thickness to the time of vapor exposure.

For our purposes, the deposition rate was maintained at $\sim .01\ \frac{\text{Å}}{s}$, to maintain mono-layer control. To achieve this flux rate, the metals are maintained at a temperature where the vapor pressure of the metal is 1.32×10^{-5} atm. Until the temperature of the K-cell reaches this desired value, a shutter is placed between the cell and the substrate. Once the desired temperature is reached, the shutter is removed, and the evaporated metal is allowed to coat the substrate. During this period, the chamber walls are cooled with liquid N_2 to ensure that the vapor that does not coat the sample is condensed on the walls. Once condensed, this gas does not contribute to the ambient pressure of the chamber.

During deposition, Reflection High-Energy Electron Diffraction (RHEED) was used to determine the quality of the deposited film. The specifics of RHEED will be described in Section (2.9).

In order to improve the quality of the deposited layer, the temperature of the substrate can be increased to promote the migration of the atoms on the surface. For a given material, the annealing temperature, T_a, can be described using the following equation:

$$T_a = \frac{T_m}{3} \tag{2.136}$$

where T_m is the melting point of the material, *Thornton* (1986). After a film is deposited, the substrate temperature is raised above the T_a of the material of the film and maintained at this temperature for ∼15-20 min, while watching the RHEED pattern to monitor the changes in the film caused by the heating. The specifics of RHEED characterization will be discussed in Section (2.9). However, since RHEED uses the diffraction of an electron beam scattered by a 2D surface, it is informative to first understand the diffraction of a 3D surface. In the next section, the specifics of the diffraction of X-rays by a 3D surface will be discussed.

2.8 X-Ray Diffraction (XRD)

In Section (2.3.3) and Section (2.3.4), magneto-elastic and magneto-electric coupling were discussed. It has been made clear that in order to understand this coupling, an accurate depiction of the material's crystal lattice is essential. The crystalline structure of the samples used in this study were determined using X-ray crystallography. This technique utilizes the diffraction of X-rays to determine the crystalline structure of a material. Both the physics of this technique and the apparatus used to conduct this analysis will be discussed. This section will begin with the physics of diffraction.

Generally, diffraction relies on the wave nature of a scattered beam. When a beam is incident upon a crystal, the scattered beam changes its direction and or magnitude after interacting with each ion in the crystal lattice. Assuming that these scattering events are elastic, only the direction of the wavevector, $\hat{\mathbf{k}}$, changes, while the magnitude, $|\mathbf{k}|$, remains the same. The specifics of the change in $\hat{\mathbf{k}}$ will depend on the shape of the scatterer. However, for observation points far from the scattering object, small differences in the direction of the beam are negligible. As a result, for distances far from the sample, each scatterer can be treated as a point particle. Consequently, in order to conduct this sort of analysis, it is important to first determine the diffraction regime. To specifically answer the question, *"how far is far?"*, there are generally two regimes that are considered, near-field and far-field. In the near-field regime, Fresnel diffraction holds, and the direction of the diffracted beams are specifically considered. In the far-field regime, the Fraunhofer diffraction regime, the scattered beams are assumed to be parallel. Using one's intuition, it would seem that the conditions for the two regimes would depend on the dimensions of the scatterer, d, the wavelength of the scattered beam, λ, and the distance between the scattering object and the point of observation, L. Considering the effect each of these parameters has on the observed diffraction pattern, one can define a diffraction parameter, D, which enables one to determine the diffraction regime. D can be described by the following equation:

$$D = \frac{d^2}{L\lambda} \tag{2.137}$$

The different regimes are determined by the following conditions of D:

$$\begin{aligned} D << 1 \ &\textbf{(Fraunhofer diffraction Regime)} \\ D >> 1 \ &\textbf{(Fresnel diffraction Regime)} \end{aligned} \tag{2.138}$$

When determining the value of this parameter for the setup used during this analysis, one can begin with the value of L, where L is $\sim .5$ m. Since this value is much larger than the inter-atomic spacing, d ($\sim$ 1 Å), $\frac{d}{L}$<<1. The only remaining free parameter is λ. The condition used to determine the λ necessary to resolve the structure of the lattice depends on the inter-atomic spacing of the lattice ions. The value of λ should be $\sim$d. Therefore, for most materials, λ must be $\sim$ 1 Å.Since the wavelength of X-rays ranges from 0.1Å- 1Å, X-rays satisfy this criterion on λ, and thus are used to resolve the structure of the lattice. Inserting these approximate values for the important parameters in Equation (2.137) to determine D, one finds the following result:

$$D = \frac{(1 \times 10^{-10})^2}{L(1 \times 10^{-10})} \approx \frac{1 \times 10^{-10}}{L} \tag{2.139}$$

From this analysis, it is clear that the measurements described in this dissertation were conducted in the Fraunhofer regime, and that the scattered beams can be assumed to be parallel. This result will be important for the analysis implemented later in this section.

When determining the diffraction pattern of a crystal, there are two methods that are generally employed to describe the diffraction of X-rays by a crystal lattice, the Von Laue and the Bragg representation. Although, these formulations are equivalent, they highlight different aspects of the diffraction of X-rays by an ordered lattice. Both methods will be described and used. However, a demonstration of the equivalence of these formulations will not be discussed. For an explanation of the congruence of these methods, the interested reader can refer to *Ashcroft and Mermin* (1976). In the following portion of this section, the Bragg formulation of X-Ray Diffraction (XRD) will be discussed.

A schematic figure depicting the diffraction of an X-ray beam using the Bragg representation can be found in Figure (2.22). From this figure, it is also clear that this model rests on the planar nature of the diffracted beams, which is only satisfied in the Fraunhofer regime. As was mentioned in Section (2.2.2), if one uses the Bragg representation, a family of lattice planes consists of an infinite number of evenly

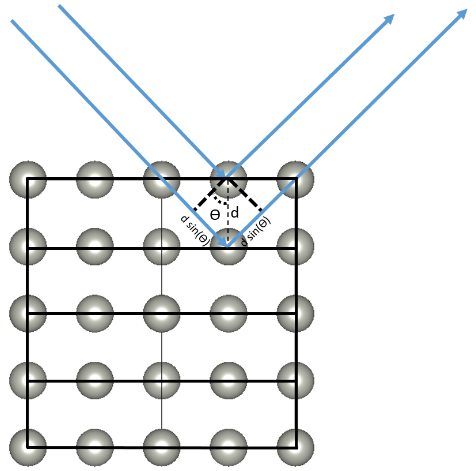

Figure 2.22: Schematic representation of the diffraction of an X-Ray beam by a a 3D lattice

spaced planes. As a result, the intensity of the diffracted beam at a point in space, $\mathbf{r_0}$, will be equal to the sum of the amplitudes of the diffracted beams from each plane at the position, $\mathbf{r_0}$. Due to the wave nature of the X-ray beams, the observed intensity at the position, $\mathbf{r_0}$, will depend on the difference in the path lengths of the rays diffracted by each family of planes. In the Bragg formulation, the maximum intensity will occur when the beams interfere constructively, or when the path length difference ($\Delta\mathbf{r}$) of the diffracted rays is proportional to an integer multiple of the X-ray wavelength. This condition can be described using the following equation:

$$\Delta\mathbf{r} = m\lambda \tag{2.140}$$

where λ is the wavelength of the incident beam and m is the diffraction order of the observed peak. The different orders in Equation (2.140) are a consequence of the oscillatory nature of the diffracted beam. Figure (2.22) depicts the path length difference between beams scattered by planes separated by a distance, d. From this

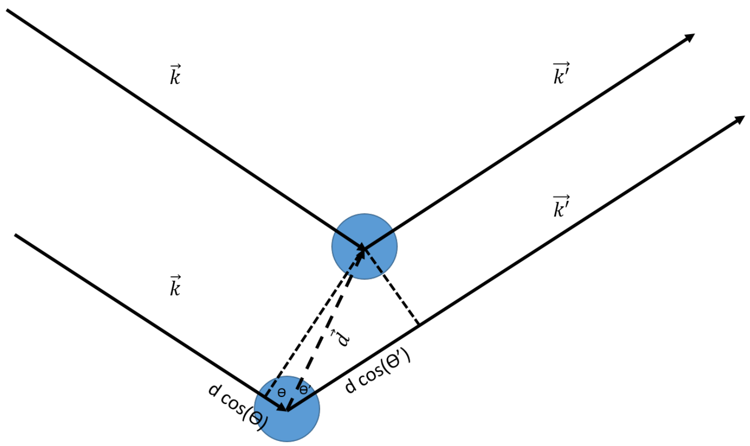

Figure 2.23: Schematic Diagram of Von Laue reflection

figure, one can deduce that Δr can also be described using the following equation:

$$\mathbf{\Delta r} = 2\text{dsin}(\theta) \tag{2.141}$$

where θ is equal to the angle between the incident beam and the diffracting lattice plane. Setting Equations (2.140) and (2.141) equal to one other results in the following relation between the wavelength of the scattered beam and the inter-atomic spacing of the lattice scatterers:

$$m\lambda = 2\text{dsin}(\theta) \tag{2.142}$$

As was highlighted in Section (2.2.2), each lattice consists of several families of planes. Consequently, the complete description of the XRD pattern of a material will require that each family of planes is considered. However, if one uses the Von Laue representation of diffraction, the scattering of the X-rays can be described using only two atoms. This representation will now be discussed.

Figure (2.23) schematically depicts the Von Laue representation of the scattering of X-rays using two atoms of a Bravais lattice. Using Figure (2.23), one can conclude that the path length difference (**Δr**) between atoms scattered by each of the two atoms can be described by the following equation:

$$\Delta\mathbf{r} = \hat{\mathbf{k}}_{\mathbf{f}} \cdot \mathbf{d} - \hat{\mathbf{k}}_{\mathbf{i}} \cdot \mathbf{d} = |\mathbf{d}|\cos(\theta') - |\mathbf{d}|\cos(\theta) \tag{2.143}$$

where θ and θ' are the angles of the incident and scattered beams measured relative to the displacement vector ($\hat{\mathbf{d}}$) between the two atoms, respectively. Although, the incident beams are scattered in all directions, as was the case in the Bragg representation, it is assumed that the maximum intensity occurs when the beams constructively interfere or when Δr is equal to an integer multiple of the wavelength of the scattered beam. Setting Equations (2.143) and (2.140) equal to one another, we find the following relation to be true:

$$|\mathbf{d}|\cos(\theta') - |\mathbf{d}|\cos(\theta) = m\lambda \tag{2.144}$$

Multiplying both sides of this equation by $\frac{2\pi}{\lambda}$, results in the following equation:

$$\mathbf{k}' \cdot \mathbf{d} - \mathbf{k} \cdot \mathbf{d} = (\mathbf{k}' - \mathbf{k}) \cdot \mathbf{d} = 2\pi m \tag{2.145}$$

. After taking the exponent of both sides of Equation (2.145) with a base of e, it follows that the next equation holds:

$$e^{i(\mathbf{k}'-\mathbf{k})\cdot\mathbf{d}} = e^{i2\pi m} = 1 \tag{2.146}$$

Since the two atoms used to describe Von Laue diffraction [Figure (2.23)] are atoms of the Bravais lattice, **d** can be replaced by $\mathbf{R_i}$, where $\mathbf{R_i}$ is the lattice constant of the Bravais lattice along the i-axis. Making this substitution, the final result can be described using the following equation:

$$e^{i(\mathbf{k}'-\mathbf{k})\cdot\mathbf{Ri}} = 1 \tag{2.147}$$

Comparing this equation to Equation (2.49), we find that the change in the wavevector ($\mathbf{k}'$-$\mathbf{k}$) due to scattering must be equal to the reciprocal lattice vector ($\mathbf{K}$). Making this substitution in Equation (2.147), results in the following result:

$$e^{i\mathrm{K}\cdot\mathrm{R_i}} = 1 \tag{2.148}$$

Equating the exponents of Equation (2.147) and Equation (2.148) results in the following equation:

$$\mathbf{k}' - \mathbf{k} = \mathbf{K} \tag{2.149}$$

This equation's dependence on $\mathbf{k}'$ can be removed by adding $\mathbf{k}$ to both sides of Equation (2.149) and then squaring each side, which leads to the following equation:

$$|k'|^2 = |k|^2 + 2\mathbf{k}\cdot\mathbf{K} + |K|^2 \tag{2.150}$$

If only elastic scattering is considered, $|\mathbf{k}'|$=$|\mathbf{k}|$, then the following equation is valid:

$$-2\mathbf{k}\cdot\mathbf{K} = |K|^2 \tag{2.151}$$

Dividing both sides of this equation [Equation (2.151)] by a factor of both $|\mathbf{K}|$ and 2 results in the following relation:

$$\mathbf{k}\cdot\hat{\mathbf{K}} = \frac{|\mathbf{K}|}{2} \tag{2.152}$$

This equation[Equation (2.152)] is depicted schematically in Figure (2.24). From this figure, it is clear that the Laue condition requires that the component of $\mathbf{k}$ along the reciprocal lattice vector, ($\hat{\mathbf{K}}$), be equal to ($\frac{|\mathbf{K}|}{2}$). Although there are several $\mathbf{k}$ vectors that satisfy this condition, each one can be described by the following definition:

Definition II.1. For a reciprocal lattice vector, $\mathbf{K}$, with an origin, $\mathcal{O}$, there exists a

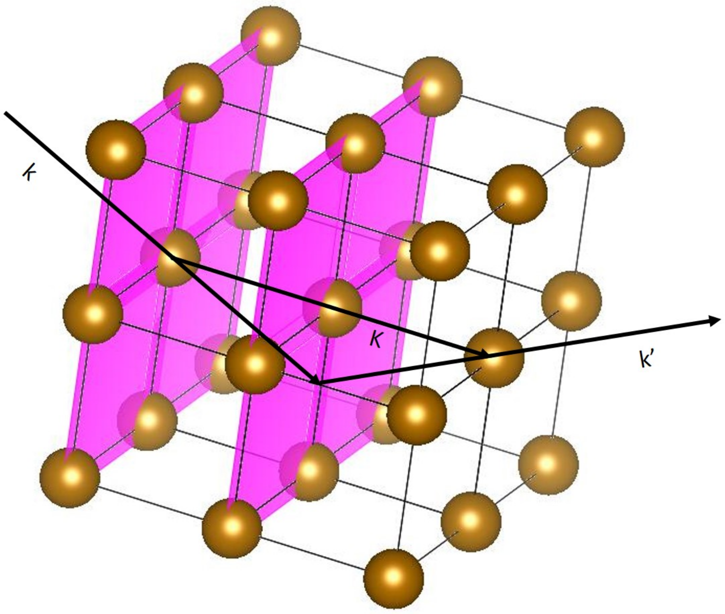

Figure 2.24: Schematic representation of the Von Laue diffraction condition

plane, $\mathcal{A}$, containing all of the perpendicular bisectors of $\mathbf{K}$. The incident $\mathbf{k}$ vectors with origin, $\mathcal{O}$, whose endpoints rest in this plane, $\mathcal{A}$, will result in scattered vectors, $\mathbf{k'}$, that lead to a diffraction peak of maximum intensity.

Upon further inquiry, one finds that the plane $\mathcal{A}$ in the Von Laue depiction is equivalent to a Bragg plane of atoms in the Bragg representation. This equivalence is highlighted in Figure (2.24). The verification of this equivalence will not be covered in this dissertation. However, interested readers are encouraged to refer to reference *Ashcroft and Mermin* (1976).

Another method used to describe these diffraction conditions, geometrically, is the Ewald construction. In this depiction, the constraints created by the conservation of both energy and momentum are represented graphically. The restrictions on the energies and momenta of the incident and scattered beams are described by the following set of equations:

$$\begin{aligned} |\mathbf{k_f}| &= |\mathbf{k_i}| \qquad \text{(a)} \\ \mathbf{k_f} - \mathbf{k_i} &= \mathbf{K} \qquad \text{(b)} \end{aligned} \tag{2.153}$$

Since Equation (2.153a) states that the magnitudes of the incident and diffracted beam must be equivalent, if one were to draw a sphere of radius $\mathbf{k_i}$ about the incident $\mathbf{k}$-vector, the points on the sphere represent the heads of all of the $\mathbf{k}_f$ vectors with tails positioned at the center of the sphere that satisfy this condition. This sphere, often referred to as the Ewald sphere, is depicted in Figure (2.25). From Equation (2.153b), it is evident that the Bragg condition will be satisfied when the scattering vector is equal to $\mathbf{K}$. Using the Ewald construction, one finds that this condition is met when two points of the reciprocal lattice lie on the Ewald sphere. This condition is depicted graphically in Figure (2.25) and will be important during the discussion of the diffraction from a 2D surface. The next part of this section will discuss the experimental techniques used to obtain the XRD pattern.

It is clear from this analysis that the diffraction peaks of a crystal will only occur when the equivalent diffraction conditions of the Bragg [Equation (2.140)] and Laue [Equation (2.152)] depictions are satisfied. For a fixed incident beam, $\mathbf{k}$, and a fixed reciprocal lattice vector, $\mathbf{K}$, there will only be one scattered vector, $\mathbf{k}'$, that satisfies the diffraction condition in either representation. Moreover, a fixed beam-lattice $(\mathbf{k} - \mathbf{K})$ orientation satisfying the diffraction condition for one order, m, will not satisfy the condition for any other order. As a consequence, these other orders will not be visible. Accordingly, in order to observe all of the diffraction peaks of a crystal, one must vary the $\mathbf{k} - \mathbf{K}$ configuration by altering either: $\hat{\mathbf{k}}$ by varying the angle of the incident beam, θ, or $\hat{\mathbf{K}}$ by rotating the sample. For the XRD characterization described in this dissertation, the sample was rotated, while the input X-ray source remained fixed. This technique is often called the Rotating-Crystal method. Figure (2.26) depicts the setup necessary for this method. In this setup, the X-rays are

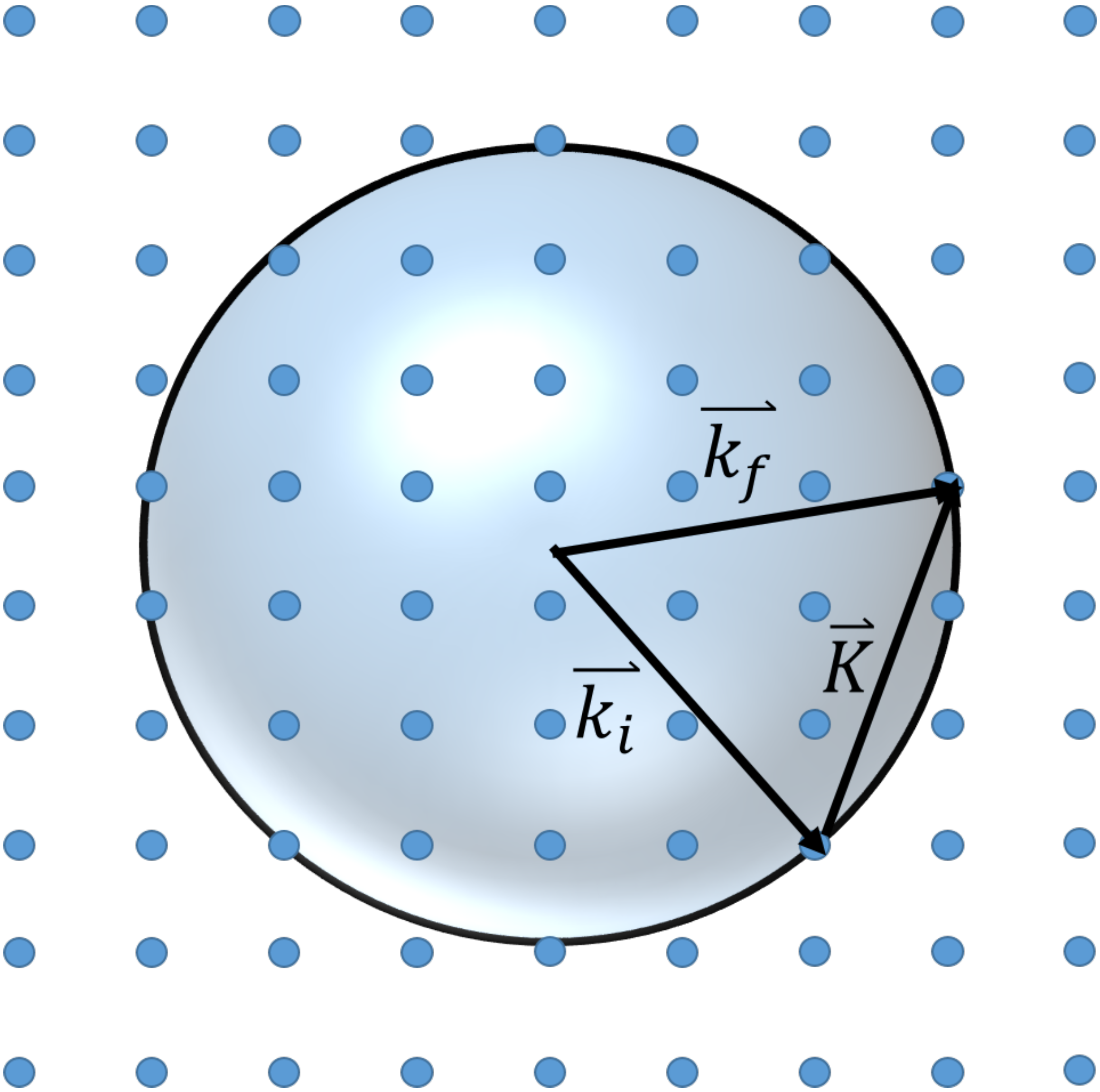

Figure 2.25: Ewald Sphere and reciprocal lattice of 3D material

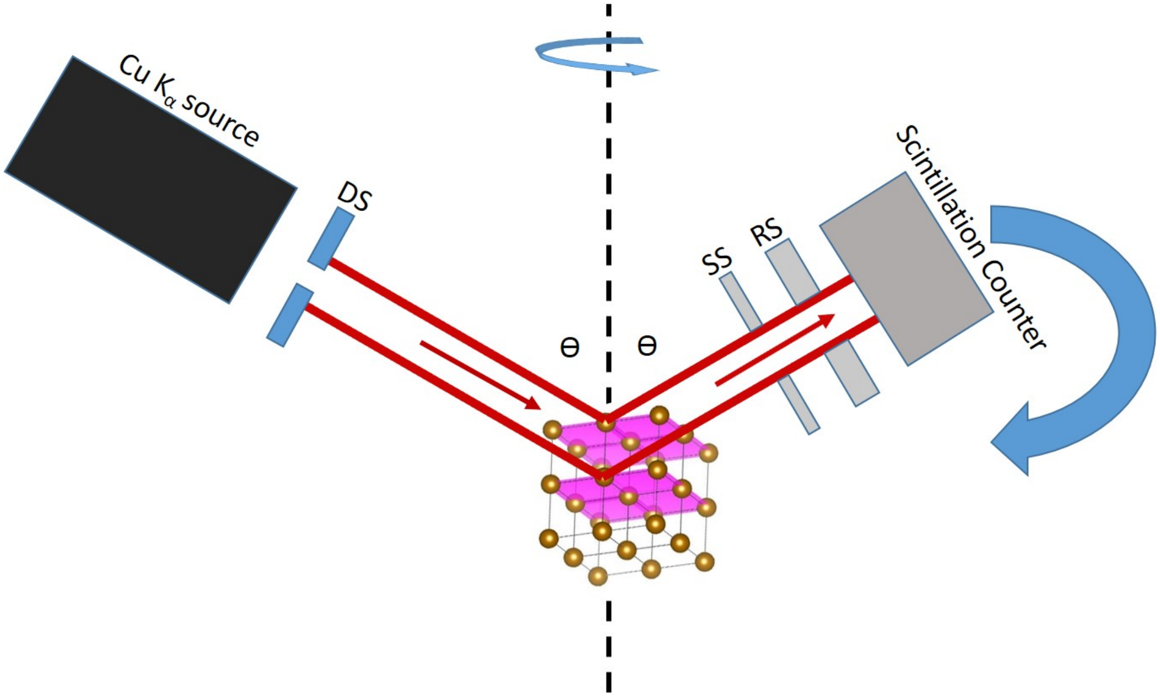

Figure 2.26: Schematic representation of the Rotating-Crystal Diffraction method

generated using a Cu Kα_2 source. Once created, the X-rays scatter off of the atoms in the crystal. Finally, the scattered beams are detected using a Scintillation counter. In the next part of this section, the mechanics of each instrument in this setup will be discussed.

The instrument used to generate the Cu Kα_2 rays, produced X-rays by bombarding a Cu target with electrons that were emitted by a heated Tungsten filament. When an electron strikes the Cu target, some of its energy was imparted to a specific Cu atom in the target resulting in the loss of an electron from the subshell with the lowest energy of the Cu atom, the 1s subshell. Since the 2P and 3P subshells both have higher energies than the 1S subshell, once ionized, the energy of the atom is decreased by the transition of an electron from either the 2P or 3P subshell of the Cu atom to the 1S subshell. This transition results in the emission of a photon with an energy equal to the difference between the initial and final states of the electron. The resultant photon of a transition to the 1S subshell from either the 2P or 3P subshells is referred to as the Kα_1 and Kα_2 lines, respectively. As the name of the source suggests, the Kα_2 lines were filtered leaving only the Kα_1 lines which were used for the XRD characterization. Once filtered, the X-rays traveled through a divergence slit (DS) to improve the resolution in the direction of the incident beam, $\mathbf{k_i}$. After traveling through this slit, the X-rays then were scattered by the atoms in sample. In order to increase the angular resolution of the measurement, after interacting with the sample, the scattered rays then entered through a scattered slit (SS). Then the rays then went through a receiving slit, before being detected using a scintillation counter. Now that the basic mechanics of X-ray Diffractometer in Figure (2.26) have been generally discussed, the methods used to implement the XRD characterization will be further explained. It is clear that as the sample is rotated during the implementation of the Rotating-Crystal method of XRD characterization, the direction of the reciprocal lattice vector, $\mathbf{K}$, will also be altered while the incident beam, $\mathbf{k}$, remains fixed. As a result, during the sample rotation, the angle between $\mathbf{k}$ and $\mathbf{K}$ changes. Since both the Bragg and Von Laue representations of diffraction rely on the specular reflection of the incident beam, if the sample is rotated by an angle, $\Delta\theta$ from its original position, the maximum diffraction signal will occur at an angle, $\Delta\theta$ from the detector's original position. Accordingly, the detector must also be rotated by $\Delta\theta$ to maximize the diffracted signal.For this reason, both the sample and the detector are both rotated for each measurement. Now that the physics of both X-ray diffraction and the experimental apparatus have been discussed, these concepts will be applied to a crystal lattice to calculate the XRD patterns of specific crystals.

Since XRD maps the reciprocal lattice, to predict the diffraction pattern of a specific crystal, one must calculate the reciprocal lattice. Returning to the derivations of the reciprocal lattice discussed earlier in Section (2.2.2), these derivations relied on the representation of the direct lattice as a series of impulses separated by distances of $\mathbf{R_i}$, more specifically, it rested on the assumption that the lattice was a Bravais lattice. As a result, the derived equations for reciprocal lattice vectors only hold for lattices that can be completely described using primitive vectors. Although this is possible for several materials, Section (2.2.1) highlighted several crystals that could only be described using the *lattice with a basis* formalism. Since lattices described using the *lattice with a basis* representation include an underlying Bravais lattice with a set of basis atoms copied at each Bravais lattice site, Equations (2.77) for the reciprocal lattice can only be used to determine the dual pair of the underlying Bravais lattice, but not the basis vectors. So how does one proceed? It is important to remember that both the Bravais lattice and the *lattice with a basis* representations are just methods used to represent a crystal lattice. For example, a bcc lattice of a single atomic species can be described using either representation. Since the crystalline structure of this material is independent of the method used to describe the lattice, the calculated XRD patterns using these different representations should be equivalent. The first step to understanding the techniques needed to resolve any discrepancy between the two representations is to examine the differences between the calculation of the diffraction signal of a crystal described using the two different methods. Therefore, this discussion will continue to explore the simple example, the diffraction of X-rays from a bcc lattice.

As was mentioned in Section (2.2.1), the bcc lattice can be described by the following set of primitive vectors:

$$\begin{aligned}
\mathbf{a_{x_0}} &= a\hat{\mathbf{x}}, \\
\mathbf{a_{y_0}} &= a\hat{\mathbf{y}}, \\
\mathbf{a_{z_0}} &= \frac{a}{2}(\hat{\mathbf{x}} + \hat{\mathbf{y}} + \hat{\mathbf{z}}).
\end{aligned} \tag{2.154}$$

where a is the lattice constant of the bcc unit cell. According to Equations (2.77), the corresponding reciprocal lattice vectors of the bcc primitive vectors are described by the following set of equations:

$$\begin{aligned}
\mathbf{b_1} &= \frac{2\pi}{a}(\hat{\mathbf{x}} - \hat{\mathbf{z}}), \\
\mathbf{b_2} &= \frac{2\pi}{a}(\hat{\mathbf{y}} - \hat{\mathbf{z}}), \\
\mathbf{b_3} &= 2\frac{2\pi}{a}\hat{\mathbf{z}}.
\end{aligned} \tag{2.155}$$

From this set of equations, one can conclude that the reciprocal lattice of the bcc lattice is the fcc lattice. Since the fcc lattice is a Bravais lattice, this structure could be equivalently represented by the following set of primitive vectors:

$$\begin{aligned}
\mathbf{b}_1 &= \frac{2\pi}{a}(\hat{\mathbf{x}} + \hat{\mathbf{y}}), \\
\mathbf{b}_2 &= \frac{2\pi}{a}(\hat{\mathbf{y}} + \hat{\mathbf{z}}), \\
\mathbf{b}_3 &= \hat{\mathbf{0}}.
\end{aligned} \tag{2.156}$$

Using the *lattice with a basis* formalism the underlying Bravais lattice used to describe the bcc unit cell is a simple cube which has the following primitive vectors:

$$\begin{aligned}
\mathbf{x_0} &= a\hat{\mathbf{x}}, \\
\mathbf{y_0} &= a\hat{\mathbf{y}}, \\
\mathbf{z_0} &= a\hat{\mathbf{z}},
\end{aligned} \tag{2.157}$$

while the following set of vectors are used to describe the basis:

$$\begin{aligned}
\mathbf{r_1} &= \hat{\mathbf{0}} \\
\mathbf{r_2} &= \frac{a}{2}(\hat{\mathbf{x}} + \hat{\mathbf{y}} + \hat{\mathbf{z}})
\end{aligned} \tag{2.158}$$

Although, this underlying Bravais lattice and basis describe a bcc lattice, if one attempts to use Equations (2.77) to determine the reciprocal lattice of this direct lattice, the resulting structure is a simple cube with the following primitive vectors:

$$\begin{aligned}\mathbf{b_1} &= \frac{2\pi}{a}\hat{\mathbf{x}},\\ \mathbf{b_2} &= \frac{2\pi}{a}\hat{\mathbf{y}},\\ \mathbf{b_3} &= \frac{2\pi}{a}\hat{\mathbf{z}}.\end{aligned} \tag{2.159}$$

Since the vectors used to describe the basis atoms were not included in the calculation, this result is inconsistent with the reciprocal lattice calculated for the same structure using only primitive vectors. Nonetheless, in the calculation using primitive vectors to describe the bcc lattice, the reciprocal lattice was determined to be the fcc lattice. Since the XRD pattern of a specific crystal is unique, the calculated diffraction pattern of the two representations must be equivalent.

The source of this inconsistency is the absence of the basis atom vectors which are not included in Equation (2.77) which is used to describe the reciprocal lattice vectors. To understand how these atoms affect the XRD signal, it is important to remember the source of the XRD signal. Depending on the position of the basis atoms, the rays diffracted by each basis atom will interfere either constructively or destructively with the rays scattered by the ions of the underlying lattice. The change in the magnitude of the detected signal will depend on the distance of the basis atoms relative to the lattice sites of the underlying Bravais lattice. Since the Von Laue depiction of diffraction considers the signal from two atoms separated by a distance d, the results of this analysis can be used to determine the dependence of the diffraction signal from the basis atoms. Equation (2.148) states that beams scattered by atoms positioned at the sites of the Bravais lattice ($\mathrm{R_i}$) will result in a maximum signal, and that the phase difference of the rays scattered by the two scatterers will be equal to $2\mathrm{m}\pi$. Consequently, the difference between the phase of rays scattered by an atom positioned at a Bravais lattice site and one scattered by an ion placed at an intermediate position will be smaller than this maximum value. This difference in phase will be dependent on the distance between the atoms. For two atoms separated by a displacement **d**, the difference in phase of rays scattered by each atom can be described by the following expression:

$$S_{\mathcal{A}} = e^{i\mathbf{K}\cdot\mathbf{d}} \tag{2.160}$$

where **K** is equal to the change in wavevector upon scattering which for scattering events that result in the maximum diffracted signal is equal to the reciprocal lattice of the underlying Bravais lattice. We know that constructive interference occurs when $\mathbf{K}\cdot\mathbf{d}$ is equal to $2\mathrm{m}\pi$ which results in a value of $S_{\mathcal{A}}$ that is equal to 1. To extend this analysis to several atoms, we can look at the scattered signal of three atoms, one placed at each of the following set of positions:

$$\begin{aligned} \mathbf{r}_0 &= \hat{\mathbf{0}}, \\ \mathbf{r}_1 &= \mathrm{d}\hat{\mathbf{y}}, \\ \mathbf{r}_2 &= \mathrm{R}\hat{\mathbf{y}}. \end{aligned} \tag{2.161}$$

If we define the phase of the scattered ray from the atom positioned at $\mathbf{r}_0$, S_0, to be equal to 1, then the phase of the ray scattered by the atom at position $\mathbf{r}_1$ will differ in phase from S_0 by the factor $e^{i\mathbf{K}\cdot(\mathbf{r}_1-\mathbf{r}_0)}$. Since atom 2 is positioned at the equivalent position of atom 0 in a neighboring unit cell, the distance between $\mathbf{r}_2$ and $\mathbf{r}_0$ is $|\mathbf{R}_i|$. Using Equation (2.48), S_3 and S_0 will be in phase. The total structure factor, $\mathrm{S}_{\mathcal{A}}$ from atoms 0,1 and 2, can be described by the following equation:

$$S_{\mathcal{A}} = S_0 S_1 S_2 = e^{i\mathbf{K}\cdot(\mathbf{r}_1-\mathbf{r}_0)} e^{i\mathbf{K}\cdot(\mathbf{r}_2-\mathbf{r}_0)} \tag{2.162}$$

Since $\mathbf{r}_2 - \mathbf{r}_0 = \mathbf{R_i}$, Equation (2.162) simplifies to the following expression:

$$S_{\mathcal{A}} = e^{i\mathbf{K}\cdot\mathbf{R_i}} e^{i\mathbf{K}\cdot(\mathbf{r}_2-\mathbf{r}_0)} = (1)(e^{i\mathbf{K}\cdot(\mathbf{r}_1-\mathbf{r}_0)}) \tag{2.163}$$

The last manipulation of this equation holds due to Equation (2.48). The results of this analysis can be generally stated by the following equation:

$$S_{\mathcal{A}} = \sum_{i=1}^{n} e^{i\mathbf{K}\cdot(\mathbf{r}_n-\mathbf{r}_0)} \tag{2.164}$$

where $\mathbf{r}_n$ is the position of the nth scatterer and $\mathbf{r}_o$ is the position of the reference atom with scattering amplitude S_0. In an attempt to resolve the discrepancy between the calculated XRD patterns of the bcc lattice described using primitive vectors and the lattice with a basis description, this analysis will be applied to the bcc unit cell. As was discussed in Section (2.2.1), for the bcc lattice, the first Brillouin zone of the reciprocal lattice can be represented by a simple cube described by the following set of k-vectors:

$$\begin{aligned} \mathbf{b}_1 &= \frac{2\pi}{a}\hat{\mathbf{x}}, \\ \mathbf{b}_2 &= \frac{2\pi}{a}\hat{\mathbf{y}}, \\ \mathbf{b}_3 &= \frac{2\pi}{a}\hat{\mathbf{z}}. \end{aligned} \tag{2.165}$$

Extending Equation (2.165) to higher zones, it is possible to describe each point of the reciprocal lattice using the following expression:

$$\mathbf{K} = \frac{2\pi}{a}(l\hat{\mathbf{x}} + m\hat{\mathbf{y}} + n\hat{\mathbf{z}}) \tag{2.166}$$

Meanwhile, the basis atoms of the bcc lattice are described in Equation (2.57), but are reiterated by the following set of vectors:

$$\begin{aligned}\mathbf{a}_1 &= \hat{\mathbf{0}} \\ \mathbf{a}_2 &= \frac{a}{2}(\hat{\mathbf{x}} + \hat{\mathbf{y}} + \hat{\mathbf{z}}).\end{aligned} \tag{2.167}$$

Applying Equation (2.164) to both the reciprocal lattice described in Equation (2.166) and the positions of the basis atoms as they are described in Equation (2.167), results in the following expression:

$$S_{\mathcal{A}} = e^{i\frac{2\pi}{a}(l\hat{\mathbf{x}}+m\hat{\mathbf{y}}+n\hat{\mathbf{z}})\cdot(\hat{\mathbf{0}}+\frac{a}{2}(\hat{\mathbf{x}}+\hat{\mathbf{y}}+\hat{\mathbf{z}}))} = 1 + e^{i\pi(l+m+n)} \tag{2.168}$$

The results of this analysis suggest that the value of $S_{\mathcal{A}}$ will depend on the sum of the scalars, l,m, and n in a manner described by the following set of conditional equations:

$$\begin{aligned}l+m+n = \text{odd} &\rightarrow S_{\mathcal{A}} = 0 \\ l+m+n = \text{even} &\rightarrow S_{\mathcal{A}} = 2.\end{aligned} \tag{2.169}$$

Using this equation, we see that the (1 0 0), (0 1 0), (0 0 1), and (1 1 1) peaks vanish. Meanwhile, the (0 0 0), (1 1 0), (1 0 1), and (0 1 1) peaks all survive. These peaks are the same as those for an fcc structure. From this analysis,it is clear that when only the Bravais lattice is considered for a structure described using the *lattice with a basis* method, the calculated XRD pattern differs from the same structure represented using only primitive vectors. However, when the interference from the basis atoms is included in the diffraction pattern by using the structure factor, $S_{\mathcal{A}}$, the XRD pattern of the structure represented using only primitive vectors is recovered. Since the *lattice with a basis* method will be used to describe the crystalline structures studied in this dissertation, the structure factor will be used to describe the measured and calculated XRD patterns of this dissertation.

Earlier in this Section (2.8), the structure factor, $\mathcal{S}_{\mathcal{A}}$ was introduced to describe the cancellation of the Bragg peak with mixed Miller indices caused by an intermediate plane of atoms between the two planes which contain the corners of the unit cell. For the fcc Bravais lattice all of the atoms in each plane were the same. However, this is not the case for the $FePd_3$ lattice, where the planes that contain the corners of the cube contain both Fe and Pd atoms, while the intermediate planes consist only of Pd atoms. As a result, when the scattered rays reach the detector they are in phase, but due to the difference in the chemical composition of the scatterers the relative amplitudes are not equivalent. Consequently, the reflection is not completely canceled. As a result, the Bragg peaks from lattice planes with mixed indices are observed. The size of the peak depends on the chemical ordering of the lattice. The larger the number of chemically and structurally ordered crystallites, the higher the intensity of the mixed Bragg peak. Accordingly, the (100) Bragg peak can be used to determine the chemical and structural ordering of the structure. For the sample described in this dissertation, the ratio of the (100):(200) peaks, **S**, will be used to determine the degree of ordering in the sample.

In this section, the diffraction of X-rays by a 3D material was discussed. In the next section, the diffraction pattern of waves scattered by a 2D surface during Reflection High Energy Electric Diffraction (RHEED) characterization will be discussed.

2.9 Reflection High-Energy Electron Diffraction (RHEED)

As was mentioned in Section (2.7), the samples used in this study were grown using Ultra-High Vacuum deposition. During the growth of each sample, Reflection High-Energy Electron Diffraction (RHEED) was used to determine the surface quality of each deposited layer, in-situ. In this section of the dissertation, the theory of this structural characterization method will be discussed.

The RHEED setup used for these studies consisted of an electron gun, a phosphor screen, and a camera. The electron gun, placed inside the chamber, was used to

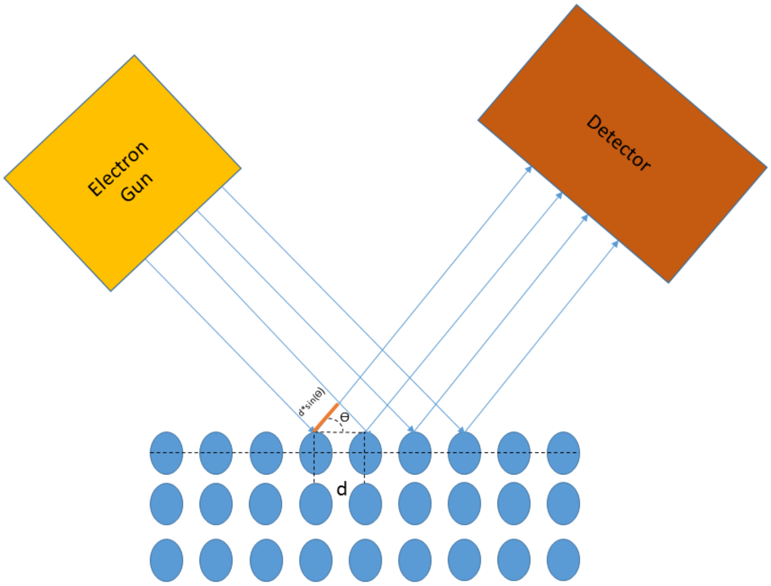

Figure 2.27: Schematic Drawing of RHEED setup

generate a beam of electrons of fixed energy. For this study, the electrons used had an energy, E, equal to 14.6 keV. The magnitude of the associated wavevector, $\mathbf{k_i}$, of each incident electron can be determined using the following equation,

$$|\mathbf{k}| = \sqrt{\frac{2m^{\star}E}{\hbar^2}} \tag{2.170}$$

where m^* is the free electron mass within the solid Inserting the value of $|\mathbf{k_i}|$ into Equation (2.170), one can conclude that $|\mathbf{k_i}|$ is equal to . Once ejected, the trajectory of the electrons was controlled using a magnetic deflector which ensured that the electrons were incident at grazing angles ($\sim$ 2-3^o) relative to the crystal surface. Upon reaching the sample, the electrons were scattered by the crystal ions. After interacting with the ions of the crystal, these scattered electrons continued to travel through the chamber with the wavevector, $\mathbf{k_f}$. Ultimately, the paths of the diffracted electrons were terminated by an interaction with the atoms in a phosphor screen. The light released during the interaction between the ions of the screen and the electrons enabled the diffraction pattern to be recorded by the camera outside of the chamber. A schematic drawing of the RHEED setup is displayed in Figure (2.27). Since the propagation vector of the beam of electrons ($\mathbf{k}_i$) was nearly parallel to the sample surface, the beam of electrons only penetrated the first few layers of the sample. Consequently, the majority of the scattering events took place in the top layers of the sample. As a result, RHEED allowed us to probe the structure of the sample surface. As was the case for XRD [Section (2.8)], the RHEED pattern of a surface depends on the spacing and orientation of the scatterers in the crystal along with the distance of each scatterer from the phosphor screen. Consequently, the theory of RHEED is similar to that of XRD. It is for this reason that the formalism used to derive the diffraction pattern of the 3D surface will now be used to derive the diffraction pattern of a 2D surface.

Following the derivation found in *Ichimiya and Cohen* (2004), the diffraction pattern of a 2D lattice can be determined by first representing the lattice as an M × N array of ions. The positions of each ion in the array can be described by the following equation:

$$\mathbf{r} = na\hat{\mathbf{x}} + mb\hat{\mathbf{y}} \tag{2.171}$$

where n=1,2,3,...,N and m=1,2,3,...,M and the parameters a and b represent the lattice constants along the $\hat{\mathbf{x}}$ and $\hat{\mathbf{y}}$ directions, respectively. The interference pattern of the scattered beams at the detector can be determined by inserting $\mathbf{r}$ into Equation (2.160), which results in the following expression for $\mathcal{S}_A$:

$$\mathcal{S}_A = \sum_{n=1}^{N}\sum_{m=1}^{M} e^{i\mathbf{K}\cdot(ma\hat{\mathbf{x}}+nb\hat{\mathbf{y}})} \tag{2.172}$$

Solving the finite geometric sum, results fin the following relation:

$$\mathcal{S}_A = \frac{1-e^{i\mathbf{K}\cdot Ma\hat{\mathbf{x}}}}{1-e^{i\mathbf{K}\cdot a\hat{\mathbf{x}}}}\frac{1-e^{i\mathbf{K}\cdot Nb\hat{\mathbf{y}}}}{1-e^{i\mathbf{K}\cdot b\hat{\mathbf{y}}}} \tag{2.173}$$

Calculating the intensity of the signal by taking the square modulus of $\mathcal{S}_A$, one finds that the intensity is proportional to the following expression:

$$I \propto \frac{\sin^2(\frac{K_x M a}{2})\,\sin^2(\frac{K_y N b}{2})}{\sin^2(\frac{K_x a}{2})\,\sin^2(\frac{K_y b}{2})}. \tag{2.174}$$

It is clear from Equation (2.174) that for variations in $\mathbf{K_x}$, the non-zero values of intensity exist over a spread in $\mathbf{K_x}$ approximately described by the following relation:

$$\Delta\mathbf{K_x} \sim \frac{2\pi}{Na} \tag{2.175}$$

Moreover, since Equation (2.174) has no dependence on $\mathbf{K}_z$, one can deduce that instead of discrete points along the $\mathbf{K_Z}$-axis, as was the case for the reciprocal lattice of a 3D material, the reciprocal lattice of the 2D surface consists of parallel rods evenly spaced along the x and y axes. In order to determine the diffraction pattern of this surface, one can use the Ewald construction introduced in Section (2.8). While using this representation, it is important to recall that Bragg diffraction occurs when the points of the reciprocal lattice lie on the surface of the Ewald sphere. Since the incident electrons have high energies, |E|, the radius of the Ewald sphere is large. As a result, the angular spread of the points of intersection of the sphere and the reciprocal lattice rods includes several points. This phenomenon is depicted in Figure (2.28). Consequently, surrounding every scattered beam with wavevector, $\mathbf{k_f}$, is a spread of allowed $\mathbf{k}$-vectors, $\Delta\mathbf{k}_f$. $\Delta\mathbf{k_f}$ is also depicted in the Figure (2.28) and can be described by the following equation:

$$\begin{aligned} \Delta\mathbf{k}_{\mathbf{f},||} = |\mathbf{k_f}|\text{sin}(\theta_f)|\Delta\theta_f &\sim \frac{2\pi}{Na} \\ \Delta\theta_f &\sim \frac{2\pi}{|\mathbf{k_f}|sin(\theta_f)Na} \end{aligned} \tag{2.176}$$

From this analysis, we can see that the finite width of the reciprocal lattice rod results

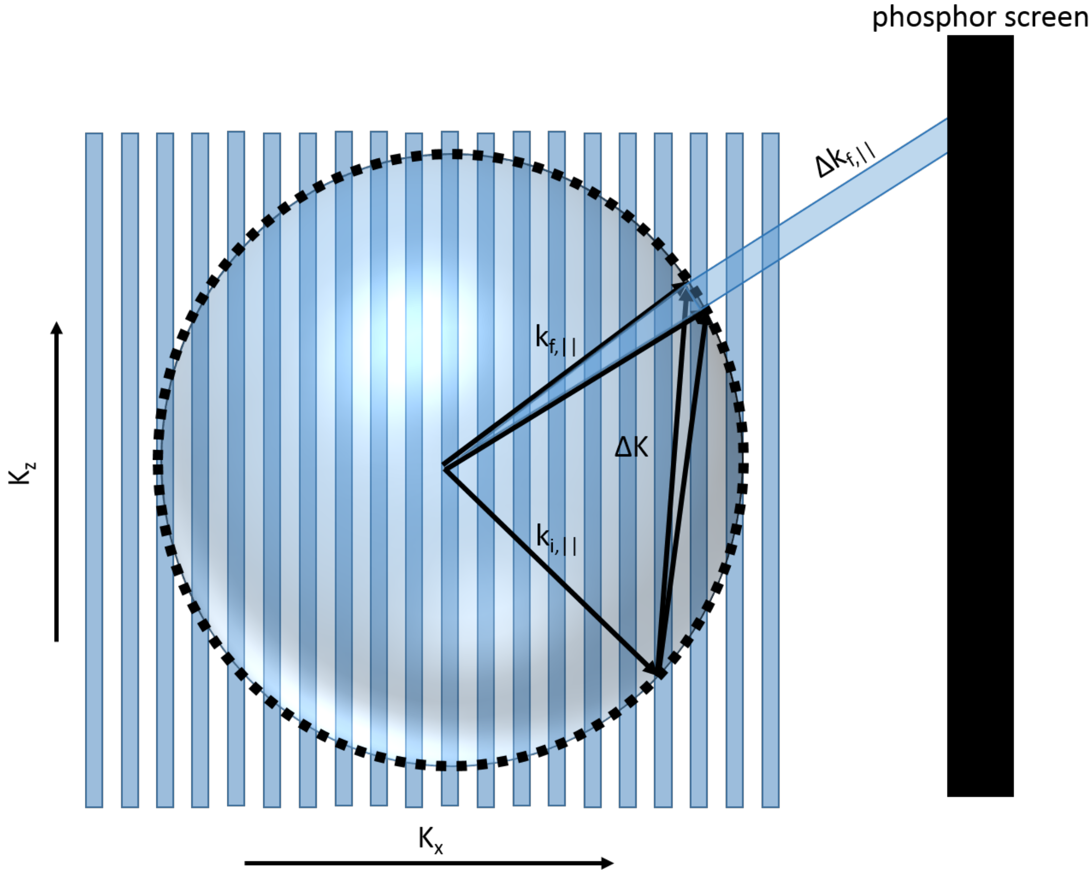

Figure 2.28: Ewald Sphere and reciprocal lattice of 2D surface

in the spread of the measured pattern along $\mathbf{K}_z$. Using Equation (2.175), it is also clear that the length of the observed streak in the diffraction pattern of a 2D lattice along the $\mathbf{K_Z}$-axis depends on the number of coherent scatterers, N. Consequently, the length of the reciprocal lattice rod can be used to determine the degree of local ordering of the atoms on the surface. In conclusion, using the formalism introduced in Section (2.8), we were able to deduce that the length of the streaks provides information about the ordering of the crystal. In Section (2.8), using the structure factor, $\mathcal{S}_A$, the effect of the basis atoms of the conventional unit cell was determined for the diffraction of a 3D surface. Using the structure factor, it is possible to determine the effect of the basis atoms on the diffraction pattern of a 2D surface.

Since the coordination number of the surface atoms is smaller than that of the bulk atoms, the structure of the surface, and in turn, the reciprocal lattice can vary greatly from the corresponding bulk counterparts. Using Equation (2.77), while assuming that the normal of the surface is parallel to ẑ, one can conclude that the reciprocal lattice of the surface of a material with bulk in-plane lattice parameters, $\mathbf{a_1}$ and $\mathbf{a_2}$, can be described by the following vectors:

$$\begin{aligned} \mathbf{a_1^*} &= 2\pi \frac{\mathbf{a_2} \times \hat{\mathbf{z}}}{\mathbf{a_1} \cdot (\mathbf{a_1} \times \hat{\mathbf{z}})} \\ \mathbf{a_2^*} &= 2\pi \frac{\mathbf{a_1} \times \hat{\mathbf{z}}}{\mathbf{a_2} \cdot (\mathbf{a_2} \times \hat{\mathbf{z}})} \end{aligned} \tag{2.177}$$

Using this formalism, while assuming that the structure of the surface is equivalent to that of the bulk, the reciprocal lattice vectors of the (001) fcc lattice has the following form:

$$\begin{aligned} \mathbf{a_1^*} &= \frac{2\pi}{|\mathbf{a_2}|}\hat{\mathbf{x}} \\ \mathbf{a_2^*} &= \frac{2\pi}{|\mathbf{a_1}|}\hat{\mathbf{y}} \end{aligned} \tag{2.178}$$

As a result, the reciprocal lattice of the surface can be described by the following equation:

$$\mathbf{B} = h\mathbf{a_1^*} + k\mathbf{a_2^*}. \tag{2.179}$$

Using the formalism of Section (2.8) to determine the scattering factor of the fcc lattice, one finds the following result,

$$\mathcal{S}_A = e^{i\mathbf{B}\cdot\mathbf{u_i}} \tag{2.180}$$

where $\mathbf{u_i}$ represents the position vectors of the basis atoms. For the fcc lattice the positions of the basis atoms are described by the following position vectors:

$$\begin{aligned} \mathbf{u_1} &= \hat{\mathbf{0}} \\ \mathbf{u_2} &= \frac{|\mathbf{a_1}|}{\mathbf{2}}\hat{\mathbf{x}} + \frac{|\mathbf{a_2}|}{\mathbf{2}}\hat{\mathbf{y}} \end{aligned} \tag{2.181}$$

Inserting these positions into Equation (2.180) results in the following equation:

$$S = 1 + e^{i\pi(h+k)} \tag{2.182}$$

As a result, the following conditions are true:

$$\begin{aligned} S &= \text{non-zero (h+k is even)} \\ S &= 0 \text{ (h+k is odd)} \end{aligned} \tag{2.183}$$

Consequently, for the surface of an fcc lattice, the intensity of the (00) Bragg peak will be greater than that of the {10} peaks. However for the bcc lattice, the basis atoms are described in Equation (2.57). Since the atom at the body-center is not in the 1^{st} lattice plane from the top surface, for grazing incidence electrons, the intensity contributions of these atoms to the pattern are not as great as for the 2^{nd} or 3^{rd} lattice plane. As a result, the RHEED pattern of the surface of the bcc lattice should be similar to that of a simple cube, where the intensities of the (00) and {10} peaks are roughly equivalent. Up to this point, we have only considered electrons that have experienced a single elastic scattering event. Since the electrons used in RHEED have high energies, it turns out for RHEED this is not the only possibility. It is possible for the electrons to scatter multiple times, inelastically. In the remaining portion of this section, these cases will be discussed.

The electrons that experience multiple scattering events are depicted in Figure (2.29) where the incident beam of electrons with wavevector, $\mathbf{k}_1$ is diffracted by the lattice plane, $\mathcal{P}_1$. Ignoring the effect of refraction on the trajectory of the scattered beam, the diffracted beam of electrons, is scattered again by plane $\mathcal{P}_2$. This scattered beam with wavevector $\mathbf{k_2}$ exits the sample. The intensity of the $\mathbf{k_2}$ will depend on the orientation of $\mathcal{P}_1$ relative to $\mathcal{P}_2$. These higher order reflections can be used to determine the ordering of the sample in different regions. As a result, these inelastically scattered beams are the source of the diagonal Kikuchi lines which are used to determine the long-range order of the material. This sort of analysis will be used to understand the RHEED results described in the Section(IV) in the thesis.

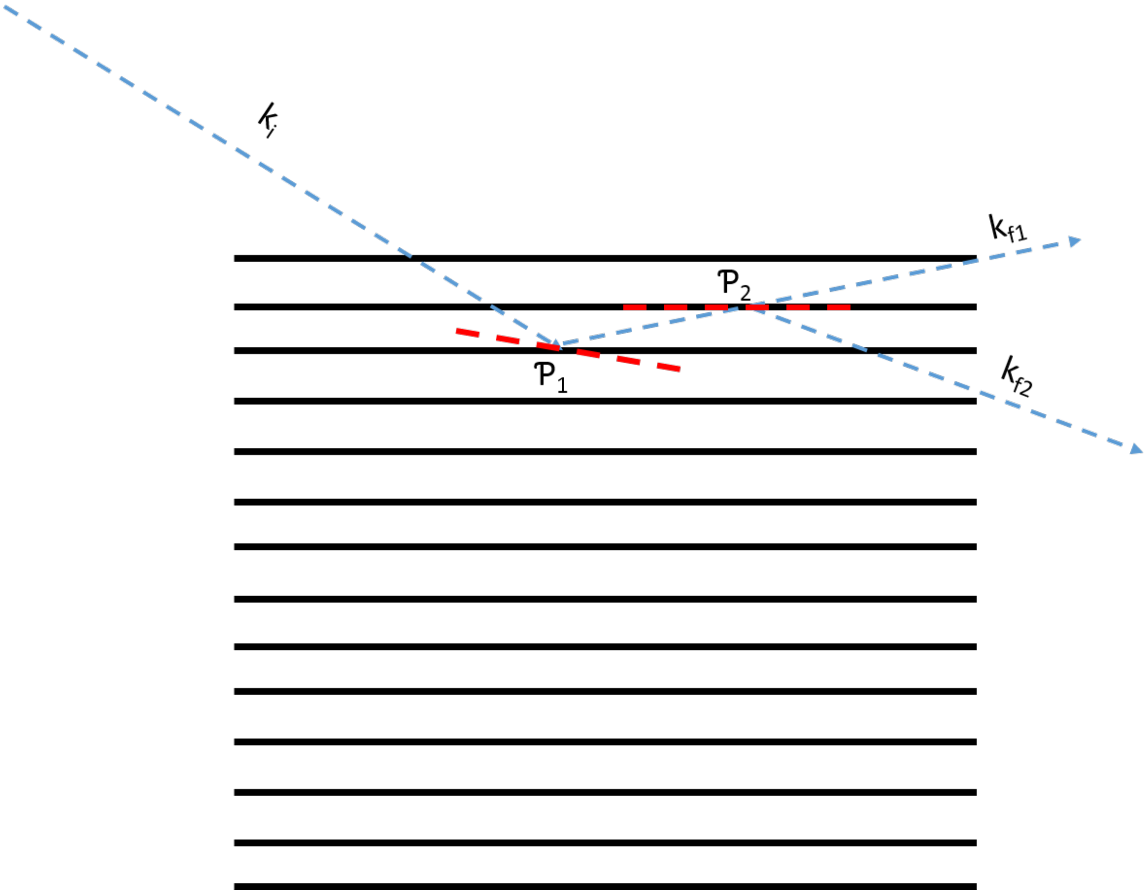

Figure 2.29: Schematic drawing of Multiple Scattering events of high energy electrons

CHAPTER III

Methods

3.0.1 Fe/BTO

Before the substrate was loaded into the chamber, the $BaTiO_3$ (100) was rinsed using methanol. Following this initial preparation, the substrate was loaded into the chamber. After the BTO substrate was mounted, it was heated to 120^oC where a 66ÅFe layer was deposited onto the substrate. This deposition took 35 minutes. After this layer was deposited, another 13 ÅFe layer was deposited. In order to increase the order of the film, during the deposition of this second layer, the substrate temperature was increased to 550^oC and then decreased to 250^oC.

3.0.2 $Fe_{84}Pd_{16}$ on $BaTiO_3$(100) of thickness .5mm

3.0.2.1 Sample Preparation and Growth

Before loading, the $BaTiO_3$ (100) substrate was rinsed in methanol and dried using N_2 gas. This process was repeated 3 times. At the end of this preparation, the substrate was loaded in the chamber where it was outgassed at 485^oC for 3.5 hours to remove any contaminates not removed by the methanol rinsing. After outgassing, the substrate was cooled to 244^oC, a temperature at which the substrate is in its cubic phase. Once the temperature stabilized, an $Pd_{84}Fe_{16}$ film of thickness 110 nm was deposited onto the substrate. Once deposited, the film was annealed for 30 min at 311^oC . After annealing, a Au cap layer was deposited onto the film to prevent oxidation.

3.0.2.2 Film Characterization

The objective of studying this sample was to determine the effect of the change in strain induced by the $BaTiO_3(100)$ substrate across the T-C transition (137^o) on the magnetization of the film. As a result, for these studies, the magnetization parallel and perpendicular to the surface of the sample was measured as a function of temperature. As was mentioned in 2.6, the longitudinal MOKE configuration is used to measure the magnetization in-plane. The setup used to implement this set of MOKE measurements is displayed in Figure (3.1). For this configuration, it is important to note that the poles of the electromagnet used to generate the magnetic field are parallel to the sample. In this configuration, the poles of the electromagnet are aligned with the normal of the sample plane. From (3.2), one can see that the laser must also, be aligned with the sample normal. As a result, the laser must travel through the poles of the electromagnet. For this geometry, the center of the electromagnet poles used in the configuration had small holes which the laser was sent through and reflected off of the sample, and then sent along the same beam path used for the longitudinal configuration. Using Labview, we were able to create a vi that generated a time-averaged MOKE signal.

From Figure (3.1), one can see for the longitudinal MOKE measurements, the sample was mounted onto a Cu mount. Holes were drilled into the mount to ensure that both the 15 W Resistive Cartridge Heater, and the 100 Ohm Platinum Resistance Temperature Detector made a good thermal connection with the Cu mount. Although, the slots were custom made to fit both elements, Apiezon H grease was used to reduce the potential for air gaps between the elements and the Cu mount. The heated elements were isolated from the motor and table using a Teflon adapter.Both

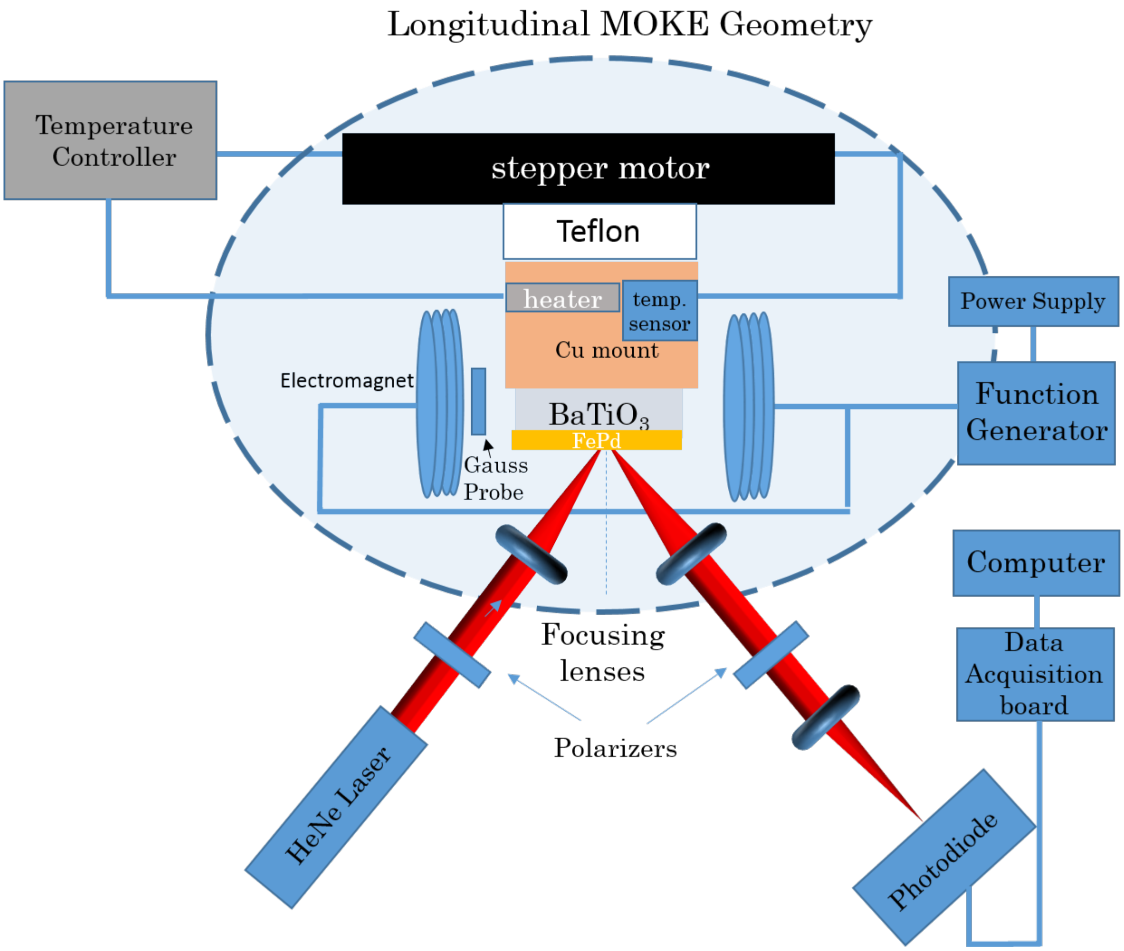

Figure 3.1: Schematic drawing of the longitudinal MOKE configuration

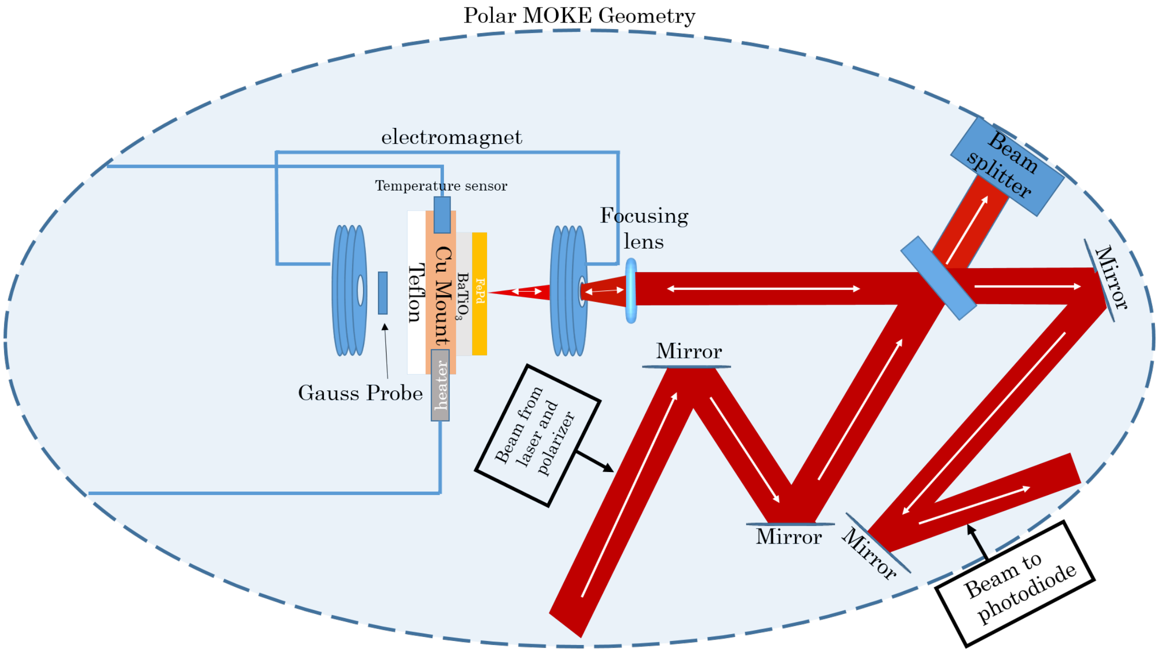

Figure 3.2: Schematic drawing of the polar MOKE configuration

the heater and temperature sensor were controlled by a the TC200 PID controller. The position of the sample was controlled using a Velmex stepper motor. For the MOKE measurements, an electromagnet was used to generate the magnetic field used to control the magnetization of the samples. The electromagnet was driven by a function generator. For these measurements, the output signal of the function generator was a sine wave with an amplitude of 2.3 V and a frequency of 1 Hz. The temperatures studied on this sample in both the longitudinal and polar geometries were 23^{o}C, 40^{o}C, 60^{o}C, 140^{o}C,160^{o}C,180^{o}C, and 190^{o}C.

The temperature dependent structural characterization was conducted using Hi-Temperature XRD crystallography. For these measurements, $\theta - 2\theta$ scans were collected at various temperatures above and below the T-C transition temperature.

3.0.3 Ordering via interdiffusion of Fe/Pd multilayer heterostructure deposited onto STO

Using Ultra-High Vacuum deposition, we were able to construct an Fe/Pd multilayer heterostructure by depositing alternating Fe and Pd layers onto a $SrTiO_3(100)$ substrate. In this section of the dissertation, the methods used to grow this heterostructure will be discussed.

The $SrTiO_3(100)$ substrate had the following dimensions (l×w×h) (10 mm × 10 mm × .5 mm). Prior to being loaded in the chamber, the substrate was rinsed in boiling methanol. Once loaded, it was outgassed at 435 ^{o}C for 1 hr. After this substrate preparation, the layers of the heterostructure were deposited. The total heterostructure consisted of two Fe/Pd bi-layers. The specifics of the structure will now be discussed.

In order to determine the composition and thickness of the bottom layer of the 1st bi-layer, the crystalline structures of $SrTiO_3$, fcc Pd, and bcc Fe were all considered. The lattice constants of $SrTiO_3$, fcc Pd, and bcc Fe are 3.905 Å,3.89 Å, and 2.87 Å, respectively. Using this information, we were able to estimate the interfacial strain of each possible configuration. A figure of the unit cells at an $Fe/SrTiO_3$ interface and a $Pd/SrTiO_3$ interface, along with each configuration's associated strain are displayed in Figure (3.3). For the $Pd/SrTiO_3$ interface, the lattice mismatch($\epsilon_{\mathrm{Pd/STO}}$) is .39%; while for an $Fe/SrTiO_3$ interface, the lattice mismatch ($\epsilon_{\mathrm{Fe/STO}}$) is -3.79%. In this configuration, the strain is compressive, while in the $Pd/SrTiO_3$ interface, the strain is tensile.It is important to note that for the $Fe/SrTiO_3$ interface, the Fe unit cell is rotated by 45^{o} to decrease the magnitude of $\epsilon_{\mathrm{Fe/STO}}$. Since the following relation holds,

$$|\epsilon_{\mathrm{Fe/STO}}| > |\epsilon_{\mathrm{Pd/STO}}|, \tag{3.1}$$

Pd was chosen as the first layer.

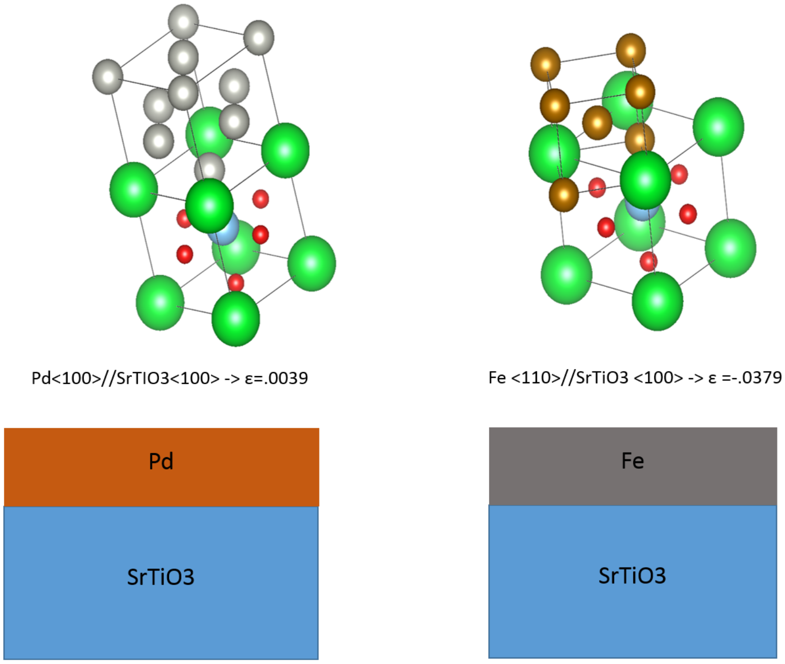

Figure 3.3: RHEED pattern of final Pd layer

Another reason that Pd was chosen as the first layer was that in previous studies of Fe/ $BaTiO_3$ heterostructures[*Govind et al.* (2013)], it was suggested that the deposited Fe ions interacted with the O^{-2} ions of the perovskite, thus forming an oxide that affected the crystalline quality of the deposited film. Given the proximity of the substrate's O^{-2} ions and the Fe ions of the deposited film at the Fe/STO interface, it was plausible that interfacial bonding between these ions could occur, resulting in the formation of an oxide at the Fe/STO interface. Using Pd as the first layer of the heterostructure, we were able to avoid this potential challenge.

In order to obtain the desired atomic Fe_xPd_{1-x} composition, the structural properties of both bcc Fe and fcc Pd were both considered. The unit cells of both body-centered cubic Fe, face-centered cubic Pd are displayed in Figure (2.4) . If one represents these unit cells using the *lattice with a basis* formalism, both the fcc and bcc structures have cubic underlying Bravais lattices. However, the basis of the fcc unit cell has 4 atoms, while the bcc basis has only 2 atoms. Referring to the bulk phase diagram of Fe/Pd alloys in Figure (2.14), it is clear that the ordered $L1_2$- $FePd_3$ phase is observed at the composition, $Fe_{30}Pd_{70}$. Since the desired atomic ratio of the entire sample is $FePd_3$, it is clear from this diagram that an Fe(30):Pd(70) ratio must be achieved in each Fe/Pd bi-layer. This information was used to determine the relative thicknesses of the constituent layers of each bi-layer.

In order to ensure that the substrate and first Pd layer had an epitaxial relationship, the Pd layer of the first bi-layer had a thickness of 19 nm. Since a 3:1 Pd:Fe ratio was required within each bi-layer, this constraint on the first Pd layer fixed the thickness of the first Fe layer.

During the deposition of each layer, the chamber pressure was maintained at 3×10^{-9} torr. The growth of each bi-layer was achieved using two Knudsen cells (K-cells) that were loaded with elemental metals with 99.9% purity. One K-cell was loaded with Fe pellets while the other was loaded with Pd pellets. During deposition, the Pd K-cell was maintained at 1251 ^{o}C which resulted in a Pd deposition rate of $.12\frac{\mathring{A}}{s}$. Since we wanted the necessary deposition time of each layer to be equivalent, the deposition rate of Fe needed to be altered to achieve the desired elemental flux. For a a Pd deposition rate of R_{Pd}, the Fe rate (R_{Fe}) needed to observe the desired composition can be determined using the following equation:

$$R_{\mathrm{Fe}} = \frac{R_{\mathrm{Pd}} n_{\mathrm{Pd}} v_{\mathrm{Fe}}}{C_{Pd\backslash Fe} n_{\mathrm{Fe}} v_{\mathrm{Pd}}} \tag{3.2}$$

where n_{Pd} (n_{Fe}) is the number of atoms per Pd (Fe) unit cell, R_{Pd} (R_{Fe}) is the deposition rate of Pd (Fe), $C_{Pd\backslash Fe}$ and v_{Pd} (v_{Fe}) is the unit volume of Pd (Fe). Using Equation (3.3), we found that the necessary deposition rate was .034 $\frac{\mathring{A}}{s}$. This deposition rate is achieved when the Fe K-cell is maintained at 1298^{o}C. During the deposition of each layer, the sample was only exposed to the vapor of a single K-cell.

Layer	thickness[nm]	dep. time[min]
Pd 1	19	26
Fe 1	10	26
Pd 2	38	52
Fe 2	30	52

Table 3.1: Simulated 2θ values of the Bragg reflections of the possible bulk phases of Pd/Fe multilayer heterostructure

For the first layer, in order to achieve a Pd layer that was 19 nm thick, the amount of time, t, that the sample was exposed to the elemental vapor was found by using the following equation:

$$t_{Pd} = \frac{L}{R_{Pd}} \tag{3.3}$$

Using Equation (3.3), we were able to determine that the sample should be exposed to the Pd flux for 26 min. Using the same analysis for each layer of the heterostructure, we were able to determine the exposure times for each layer. These times along with the corresponding film thicknesses are listed in the Table (3.1). Once the final bilayer was deposited, the sample was heated above the $FePd_3$ formation temperature, 550 ^{o}C *Myagkov et al.* (2012), for 15 minutes. Since the order-disorder transition temperature of $FePd_3$ was observed to occur at 650 ^{o}C *Myagkov et al.* (2012), during annealing the temperature did not exceed this value. After heating, a 5 nm Au cap layer was deposited onto the sample to protect the sample from oxidation. The final heterostructure was 87 nm thick along with the 5 nm cap layer, thus resulting in a total thickness of 92 nm.A schematic drawing of this structure can be found in Figure (3.4).

During the growth, the structure of each layer was determined using RHEED. The structure of the final heterostructure was determined using XRD analysis.

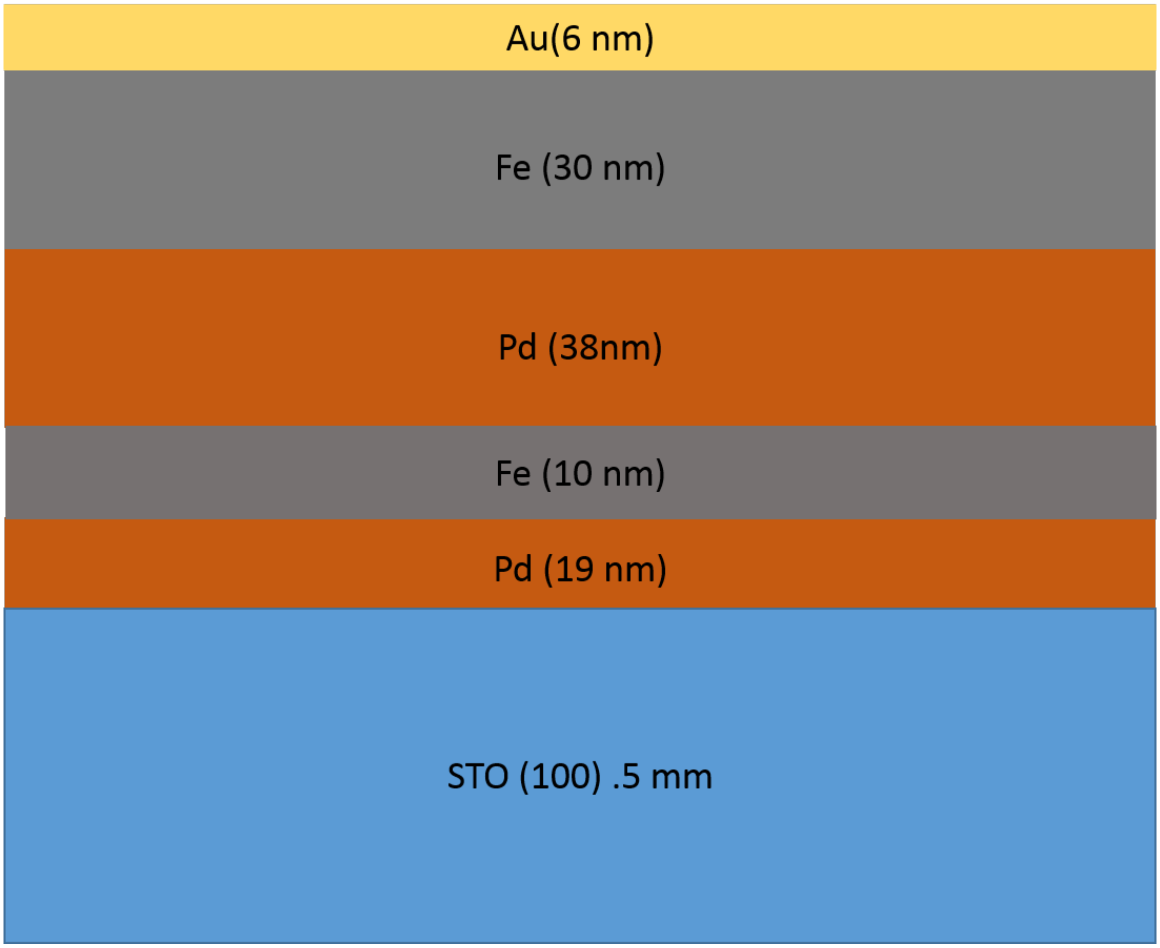

Figure 3.4: Properties of each layer of the Fe, Pd multilayer heterostructure

CHAPTER IV

Experimental Results on Structure and Magnetic Properties

Using Reflection High Energy Electron Diffraction(in-situ) and X-ray Diffraction (ex-situ), we were able to determine the crystalline structure of each sample. MOKE magnetometry in both the longitudinal and polar geometries was employed to measure the anisotropy of each sample. The results of this analysis will be discussed in this section of the dissertation.

4.0.1 Results: Fe on $BaTiO_3$(100)

The in-plane magnetization of the Fe/BTO (100) sample as a function of angle was measured using MOKE in the longitudinal configuration[Figure (3.1)]. These measurements were conducted at 23^{o}C (room temperature) and 150^{o}C. Since the T-C transition of $BaTiO_3$(100) occurs at 137^{o}C, the results of this study show the effect of the T-C transition on the deposited Fe film. A plot of the in-plane magnetization versus applied **H**-field at the angle 182^{o}C measured at RT is displayed in Figure (4.1). The magnetization v. H plot displayed in this figure exhibits saturation and switching. For this sample, the coercive field (H_c) is 100 Oe. It is clear from the absence of coherent rotation of the magnetization that the axis of **H** is along the easy axis of the plane.

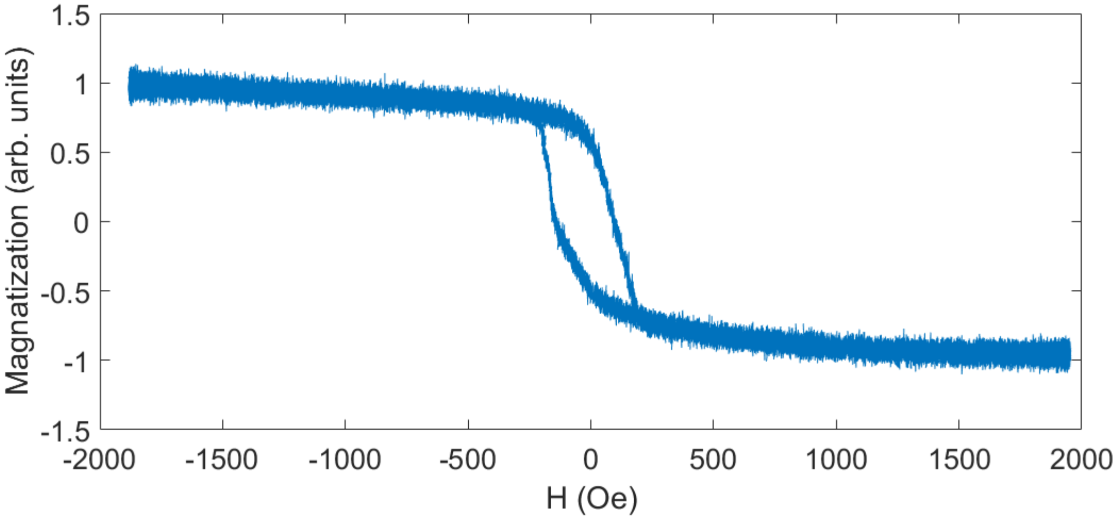

Figure 4.1: Magnetization v. H of Fe/BaTiO$_3$(100) at 23^{o}C at 182 ^{o}

Figures (4.2 and 4.3) show the results of the measurement of the H$_c$ as a function of angle at RT and 150^{o}C. It is clear from Figure (4.2) that below the T-C transition the sample demonstrates uniaxial anisotropy about the $\hat{\mathbf{a}}$ axis. Since the BaTiO$_3$ unit cell is tetragonal, from Figure, it is clear that in this phase a=b≠c. The magnitudes of the lattice constants of the unit cell along the a and b axes of the unit cell in this phase are equal to 3.9935 Å, while the c-axis is equal to 4.0385 Å. Since both the c and a-axes are in-plane, a uniaxial structural anisotropy exists within the substrate. This asymmetry in the structure of the substrate is transferred to the deposited film through an anisotropy in the strain experienced by the deposited film. From the discussion of Section(2.3.3), this anisotropy in strain results in the spins of the sample having a preferred orientation relative to the asymmetry in the strain. Consequently, when the applied **H**-field is aligned with the elongated c-axis, the $|\mathbf{H}|$ required to align the spins along this axis is smaller than along the shorter a-axis. Since a uniaxial asymmetry is observed in the coercivity polar plot of the deposited film, it is clear that below the T-C transition, there is magneto-elastic coupling between the Fe ions of the film and the BaTiO$_3$(100) substrate. However, above the T-C transition, this asymmetry disappears and the coercivity polar plot is isotropic with respect to variations in angle. This result can be explained by the change in the $BaTiO_3$ unit cell above the T-C transition. In the cubic (C) phase, the lattice parameters of the unit cell are equivalent (a=b=c) and equal to 4.0105Å. The Fe film was deposited onto the substrate while it was in its cubic phase. Since the unit cell of Fe is body-centered cubic with a lattice constant of 2.87 Å. Since the Fe unit cell is body-centered cubic, the diagonal of the cubic face of the Fe unit cell is 4.06 Å. As a result, the lattice mismatch between the deposited film and substrate is minimized if the a-axis of the Fe film is rotated by 45^o relative to the a-axis of $BaTiO_3$(Fe<110>//$BaTiO_3$<100>). When the substrate is in this phase, there is no substrate-induced strain anisotropy, and thus no observed magnetic anisotropy. This result is confirmation that the observed uniaxial anisotropy is a consequence of the substrate-induced strain anisotropy.

4.0.2 Results: Atomic ordering via interdiffusion of Fe/Pd multilayer heterostructure deposited onto STO

As was mentioned in Section (4.0.2), the Fe/Pd multilayer heterostructure deposited onto the $SrTiO_3(100)$ substrate consisted of two Fe/Pd bi-layers which were annealed to promote inter-diffusion between the deposited layers. After annealing, a Au cap layer was deposited on the structure to prevent oxidation. A schematic drawing of the heterostructure can be found in Figure (3.4). During deposition, in-situ RHEED patterns were collected to determine the film quality and orientation of each deposited layer. These images are displayed in Figure (4.4).

The RHEED pattern of the $SrTiO_3$ (100) substrate is displayed in Figure (4.4a). Using the results of the analysis of Section (2.9), one can conclude from the vertical streaks present in the image that the exposed surface exhibited local order; while the visible Kikuchi lines suggest that this order was also long-range. The RHEED patterns of the top surfaces of each deposited Fe and Pd layer are displayed in Figures (4.4b-

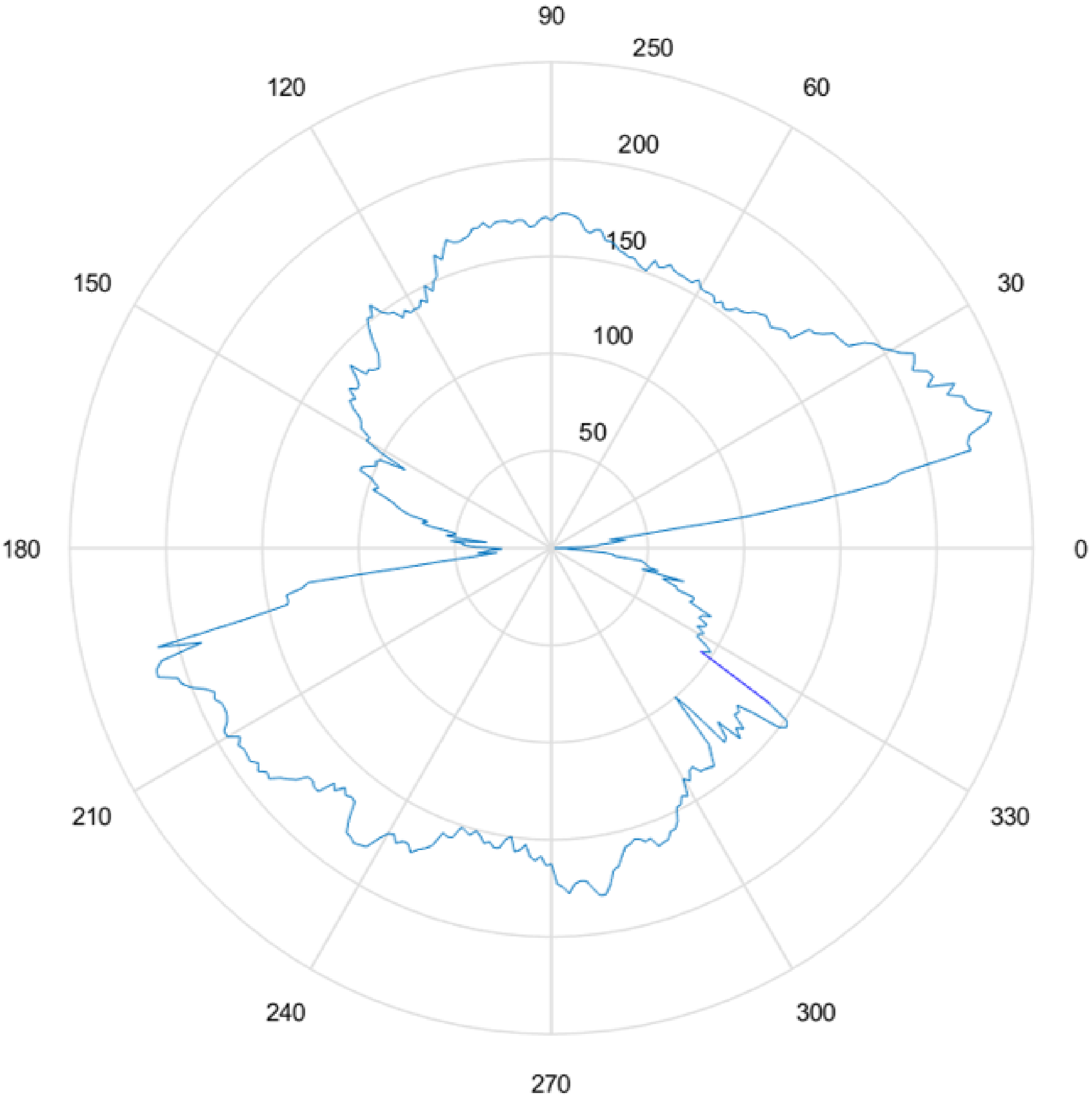

Figure 4.2: Coercive field as a function of azimuthal (in plane) angle at RT

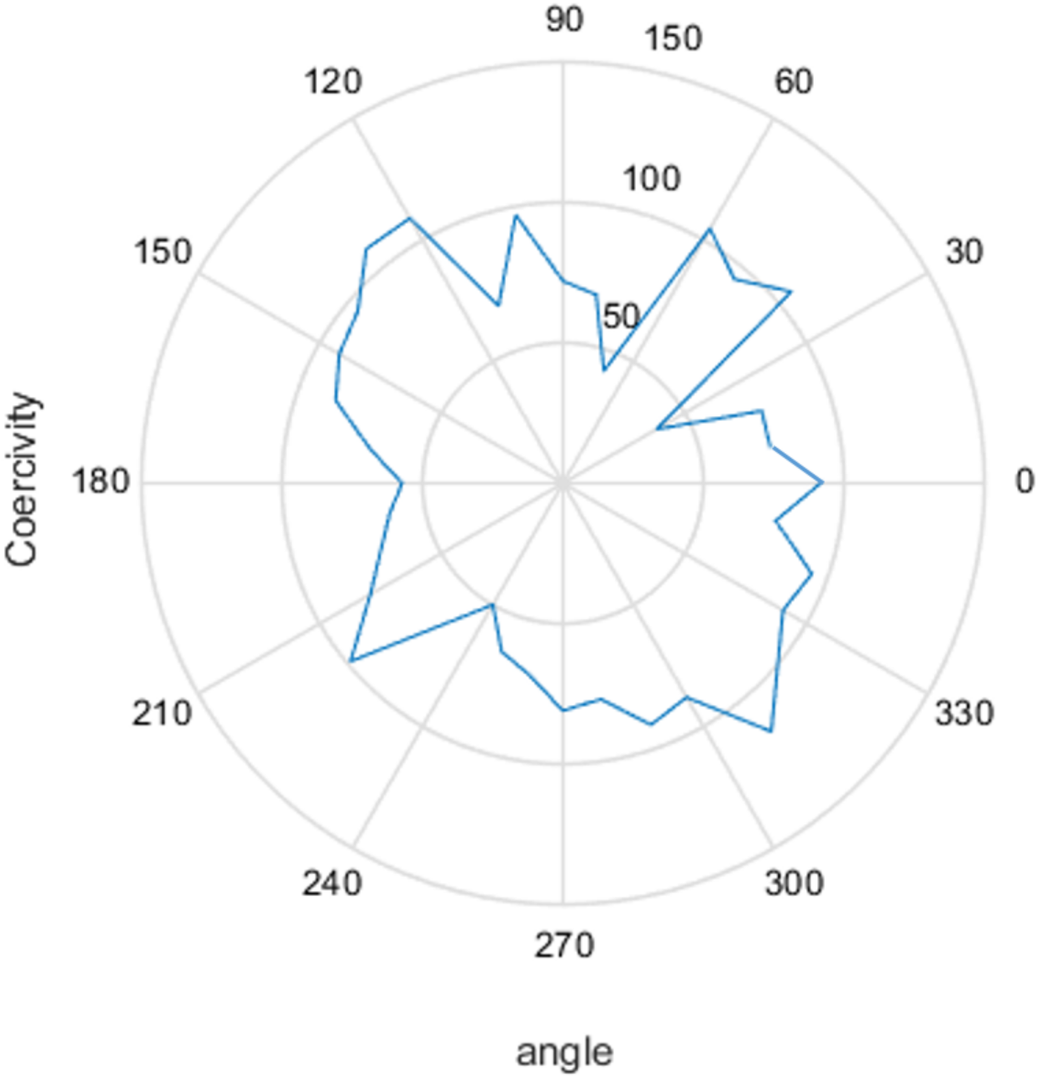

Figure 4.3: Coercive field as a function of azimuthal (in plane) angle at 150^{o}C

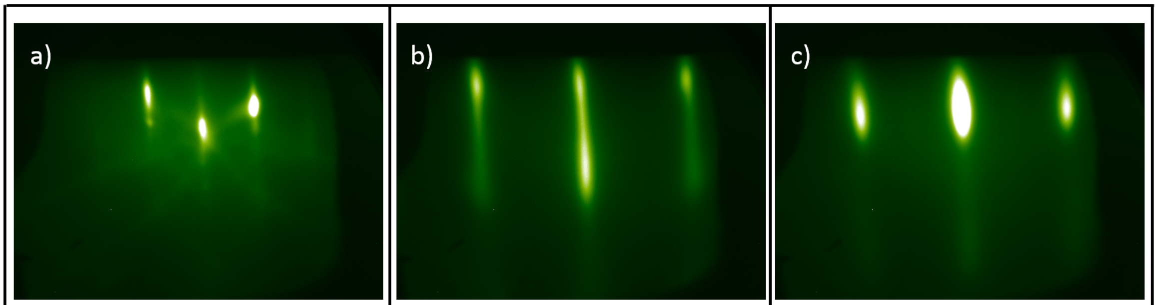

STO substrate (.5 mm)

1 Pd Layer (20 nm)

1 Fe Layer (10 nm)

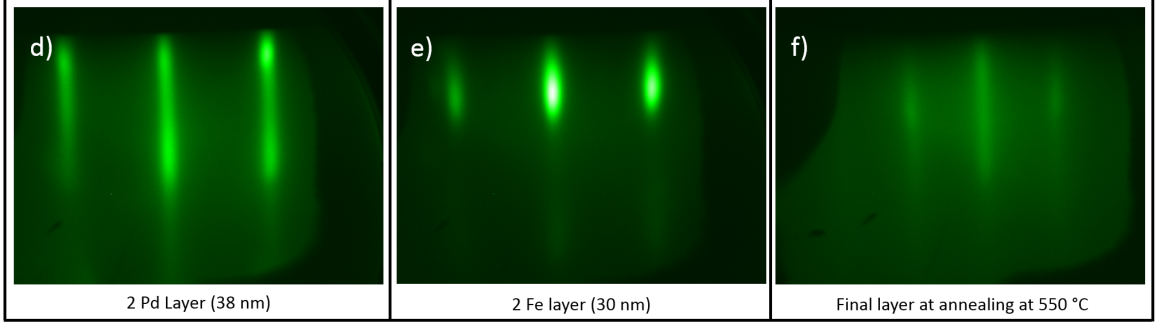

2 Pd Layer (38 nm)

2 Fe layer (30 nm)

Final layer at annealing at 550 °C

Figure 4.4: RHEED images of sample 1 heterostructure

4.4e). The vertical streaks present in each RHEED image suggests local ordering. However, the absence of Kikuchi lines in these patterns leads one to conclude that this ordering was not long-range. In each of the patterns, the visible peaks correspond to the (10),(00),($\bar{1}$0) reflections. Comparing the intensity variations of the RHEED streaks along the $\mathbf{K}_z$-axis of the Pd layers [Figures (4.4b and 4.4d)] to those of the Fe layers [Figures (4.4c and 4.4e)], we find that the Pd streaks consist of regions of continuous intensity that are larger than those of the Fe layers. From Section (2.9), we know that the length of the streak along the $\mathbf{K}_z$-axis is proportional to the number of coherent scatters, N, on the surface. Consequently, we can conclude that the ordered regions in the Pd layers are larger than in the Fe layers.

The source of this discrepancy can be understood by examining the process of film growth during UHV deposition. During growth, the sample is exposed to the elemental vapor which then condenses to form an even coating on the sample. Once deposited, the atoms with sufficient energy, migrate to potentially form structures on the surface. Using Equation (2.136), the annealing temperature of a deposited material is proportional to the material's melting temperature,T_m. Since, the melting temperatures of Fe and Pd are 1535^{o}C and 1554^{o}C, respectively, using Equation (2.136), it is clear that the associated annealing temperatures,T_a are 512 ^oC and 518^{o}C, respectively. Consequently, if the temperature of the substrate is close to the annealing temperature of the deposited layer, diffusion will occur, which would result in a decrease in the size of the ordered region. Since the annealing temperature, T_a, of Fe is lower than Pd, the Fe atoms, once deposited, had energies sufficient enough to form microstructures on the surface. These findings are consistent with *Govind et al.* (2013), where Fe nano-islands were observed on $BaTiO_3$ after annealing at 499.8^{o}C. Upon further examination, one might also notice the difference in intensities between different peaks. In the Pd RHEED patterns, the intensity of the (00) peak is larger than that of the (10) and ($\bar{1}$0) peaks. Meanwhile, in the RHEED patterns of the Fe layers, the intensities of all of the peaks are the same. From the results of the analysis in Section (2.9), this variation in the streak intensities is due to the difference in the structure factors of the Pd (fcc) and Fe (bcc) lattices. These results confirm that each layer is epitaxial. In the following section, the relative orientation of each deposited layer will be discussed.

Once the RHEED patterns were collected, using Matlab, we were able to generate intensity profiles of these patterns. Using these profiles, we were able to track the spacing between the RHEED orders of each layer at different times during the deposition of each layer. Using the spacing of the RHEED orders of each layer and Equation (), we were able to determine the relative orientation of the layers in each bi-layer. The image profiles of the Fe and Pd layer of the first bi-layer of the heterostructure are displayed in Figure (4.6a). In order to minimize the strain experienced by both films, the system works to minimize the spacing between the Fe and Pd atoms at the interface. In Figure (4.5), schematic drawings of two possible orientations of the Fe unit cell relative to the Pd unit cell at the Fe/Pd interface are displayed, along with a schematic diagram showing the position of this interface in the heterostructure. From the drawing, it is clear that when the edges of the Fe unit cell are aligned with the edges of the Pd unit cell(Fe<100>//Pd<100>) the lattice mismatch is $\epsilon_{0^o} = .26$. However, when the Fe unit cell is rotated by 45^o relative to the Pd lattice (Fe<110>//Pd<100>), $\epsilon_{45^o} = -.04$. Since

$$|\epsilon_{0^o}| > |\epsilon_{45^o}|, \tag{4.1}$$

one might expect the Fe<110>//Pd<100> to be the favored configuration of the system. Using the image profiles displayed in Figure (4.6), we were able to determine the configuration chosen by the system.

Since the in-plane lattice spacing is inversely proportional to the spacing between the RHEED diffraction orders, x_{hk}, it is clear that a larger $d_a=|x_{10}-x_{00}|$ results in a smaller in-plane lattice constant. From the unit cell configurations displayed in Figure (4.6), we can see that the d_a of Fe is slightly smaller than the d_a of Pd. Consequently, one can conclude that when exposed to e^-waves along the $\{100\}$ axes of the crystal, the spacing between the Fe atoms was larger than that of the Pd atoms. As a result, one can gather that the Fe lattice experienced compressive strain before relaxing to its bulk value on the Pd layer. Furthermore, we can also deduce that the Fe lattice was rotated by 45^o relative to the Pd lattice.

As was mentioned earlier in this section, once the heterostructure was annealed, a Au cap layer was deposited on the structure to prevent oxidation. The RHEED image of the final layer after annealing at 550^oC for 15 minutes is displayed in Figure (4.4f). The vertical streaks suggest that the final structure is ordered. However, the change in the intensities of these streaks from the final Fe layer [Figure(4.4e)], lead one to conclude that the system has formed a new ordered phase that is similar in

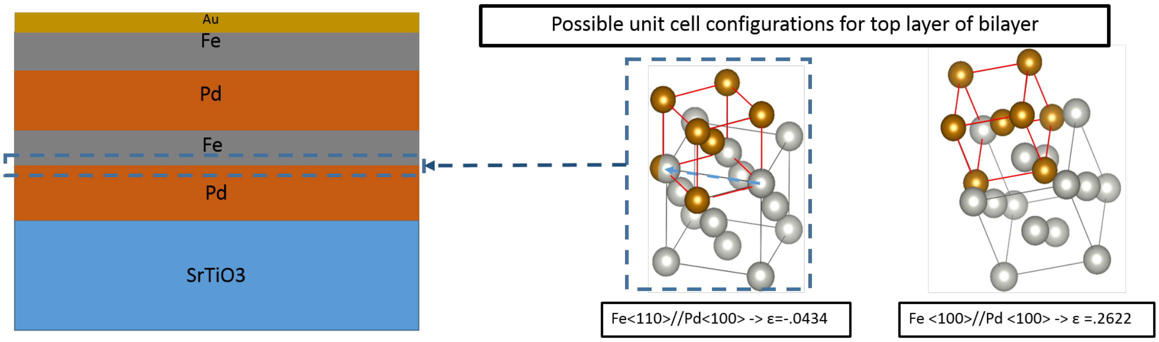

Figure 4.5: Possible unit cell configurations of the 1st Fe/Pd interface in the heterostructure

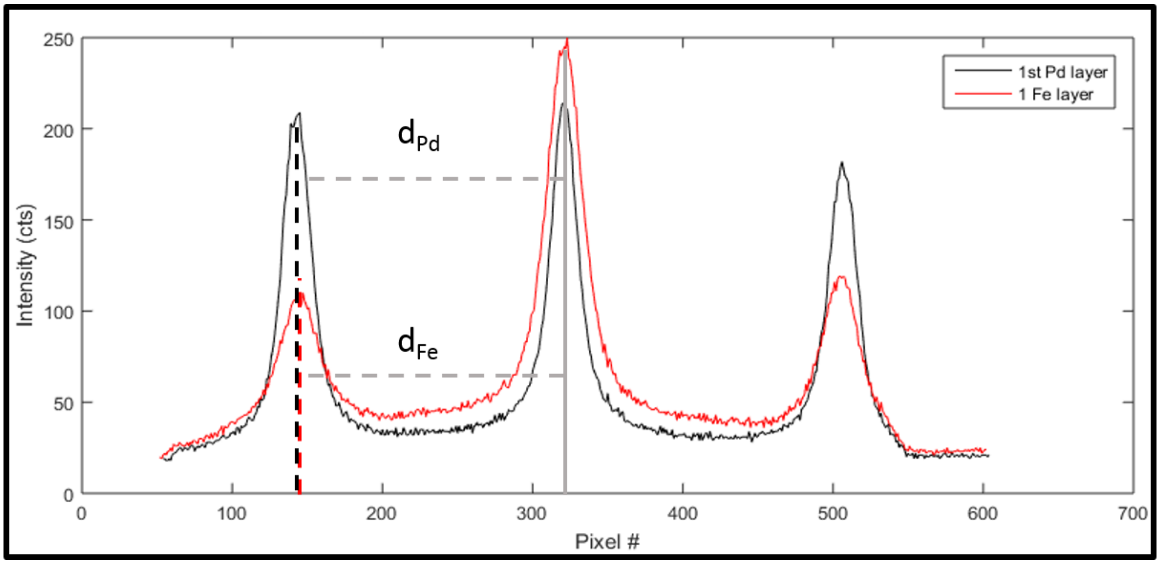

Figure 4.6: Image profiles of the RHEED images of the 1st Fe and 1st Pd layer

Phase	Bravais	(100)	(011)	(111)	(200)	(002)
$SrTiO_3$	cubic	22.752^o	32.395^o	39.9539^o	46.4689^o	46.4689^o
$FePd_3$	cubic	23.1134^o	32.9170^o	40.6073^o	47.241^o	47.241^o
FePd	tetragonal	N/A	N/A	41.0583^o	47.1888^o	48.9289^o
Fe	cubic	N/A	44.651^o	N/A	64.9882^o	64.9882^o
Pd	cubic	N/A	N/A	40.1499^o	46.7003^o	46.7003^o
Au(fcc)	cubic	N/A	N/A	38.2153^o	44.4178^o	44.4178^o

Table 4.1: Simulated 2θ values of the Bragg reflections of the possible bulk phases of Pd/Fe multilayer heterostructure

structure to the Pd (fcc) layer. These results point to the annealed layer having an fcc-like crystalline structure, which is the structure of L1_2-$FePd_3$. Although these images give a qualitative picture of the final annealed layer that is somewhat clear, in order to gain a quantitative understanding of the final structure of the sample after annealing, XRD characterization is required. The results of the XRD analysis of the final annealed Fe/Pd heterostructure will now be discussed.

The measured XRD pattern of the sample after annealing is displayed in Figure (4.7). Since the inter-diffusion as a result of annealing could result in several possible phases, the bulk diffraction peaks used for analysis were calculated using the following equations for the distance (d) between Bragg planes:

$$\begin{aligned} \frac{1}{d^2} &= \frac{h^2+k^2+l^2}{a^2}(\text{cubic}) \\ \frac{1}{d^2} &= \frac{h^2+k^2}{a^2}+\frac{l^2}{c^2}(\text{tetragonal}), \end{aligned} \tag{4.2}$$

where h,k, and l are the indices of the Bragg reflections. Using this equation [Equation (4.2)], along with Equation (2.142), we were able to determine the angular positions of the Bragg reflections for each possible phase. The simulated structures included bcc Fe, fcc Pd, L1_2-$FePd_3$, L1_0-FePd, fcc Au, and $SrTiO_3$. The 2θ values of the (100),(011),(111), (200), and (002) Bragg reflections of these phases are displayed in Table (4.1). Using non-linear regression, a sum of 7 gaussian functions was used to

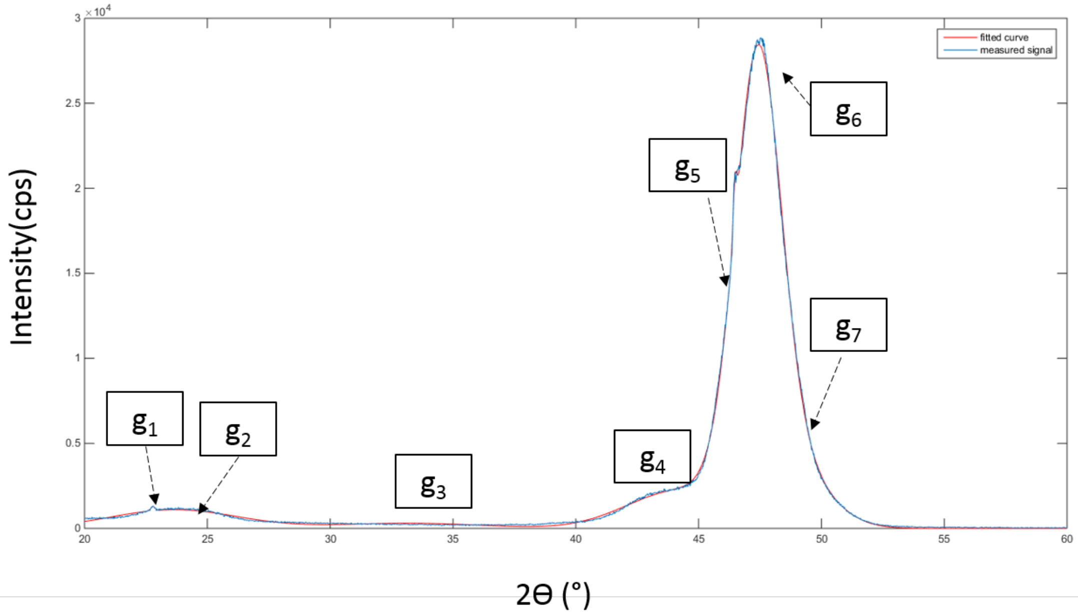

Figure 4.7: XRD FePd multilayer plots for both samples

fit the XRD profile of the sample. Each gaussian had the following form:

$$g_n = a_n exp(-(x - b_n)^2/(2c_n^2)) \tag{4.3}$$

The following function was used to fit the XRD data:

$$\mathbf{g_T} = \sum_{n=1}^{7} g_n \tag{4.4}$$

The values of each fit parameter along with the bounds of their 95 % confidence interval are included in Table (4.2). The R-square value of the fit was .9995. A figure of a plot of the XRD data along with the fitted function and its 95% bounds is displayed in Figure (4.7).

Using the 2θ positions of the simulated peaks, we were able to determine the source of each peak used to fit the measured XRD spectra. The results of this analysis are displayed in Table (4.3).

g_n	a_n	b_n	c_n
g_1	257.8 (143.9, 371.7)	22.78 (22.74, 22.82)	0.08266 (0.03972, 0.1256)
g_2	1098 (1075, 1121)	23.65 (23.58, 23.73)	2.594 (2.5, 2.688)
g_3	304.7 (284.9, 324.6)	33.18 (32.91, 33.45)	3 (2.663, 3.337)
g_4	2158 (2016, 2299)	44.13 (43.83, 44.44)	2.114 (1.956, 2.273)
g_5	2735 (2612, 2858)	46.48 (46.48, 46.48)	0.07609 (0.07192, 0.08026)
g_6	2.395e+04 (2.322e+04, 2.467e+04)	47.41 (47.41, 47.42)	0.9288 (0.9195, 0.9381)
g_7	4489 (3760, 5218)	48.3 (48.05, 48.56)	1.594 (1.523, 1.665)

Table 4.2: $\mathbf{g_T}$ fitting parameters

g_n	phase
g_1	$SrTiO_3$(100)
g_2	$FePd_3$(100)
g_3	background
g_4	Au(200)
g_5	$SrTiO_3$(200)
g_6	$FePd_3$(200)
g_7	FePd(200)

Table 4.3: Associated phases of g_N peaks

Using these results, it is clear that the fundamental lines of the $FePd_3$ (200) and FePd (200) phases are both present. However, from Table (4.2), it is evident that the amplitude of the FePd(200) peak is significantly smaller than the $FePd_3$ (200)peak. ($\frac{FePd(200)}{FePd_3(200)} = .1874$). Accordingly, we can conclude that the majority of the sample exhibits the crystalline structure of $FePd_3$. Also present in the XRD spectrum is the (100) superstructure line of $FePd_3$, which is used to determine the nature of the ordering of the $FePd_3$ phase. Using the results of the $\mathbf{g_T}$ fit, it is clear that the order parameter ($\mathbf{S}$) is equal to 0.046. These results suggest that the film exhibits structural ordering that is local. However, since S is small and the peak is broad, b_2=2.594^o, one can conclude that the film does not exhibit long-range order. It is also important to note the absence of the $FePd_3$(111) peak. From Table (4.1), the (111) peaks of the the possible phases in bulk occur between the 2θ positions 38^{o}C and 41.06^{o}C. In Figure(4.7) these peaks are not present. Since the surface of the $SrTiO_3$ substrate

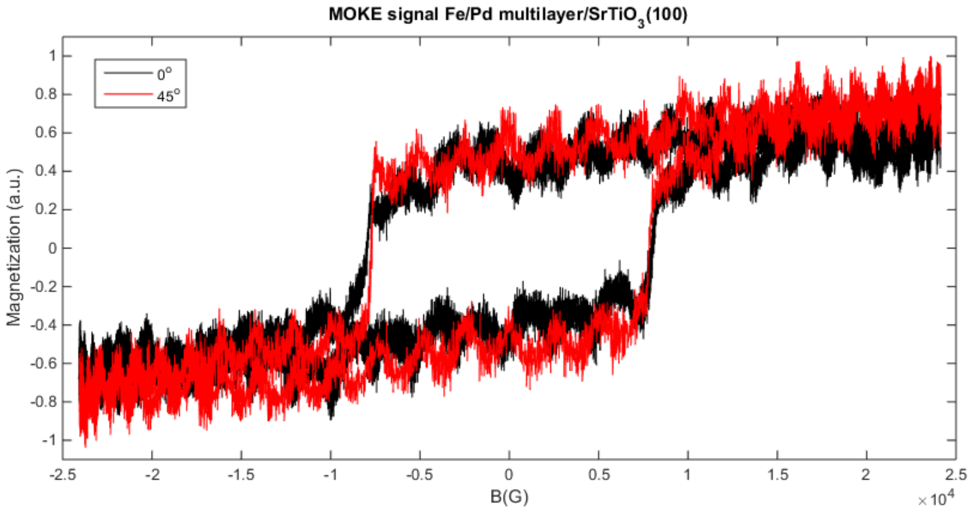

Figure 4.8: Longitudinal MOKE Pd,Fe multilayer SrTiO$_3$(100) at 0^o and 45^o

has (100) orientation and the Bragg-Brentano geometry configuration was used for these XRD measurements, reflection from crystallites with (111) orientation would only be observed for grains that are not epitaxial. Hence, the absence of the (111) orders suggests that the film is epitaxial.

Using MOKE magnetometry in the longitudinal configuration, we were able to characterize the magnetization of this material along the sample plane. A sample hysteresis loop is displayed in Figure (4.8). The results of the MOKE measurements suggest that the film demonstrates switching in-plane, with a coercive field of ~ 7600 G. Furthermore, the change in the coercivity of the magnetic hysteresis loops along the 0^o and 45^o axes of the sample displayed in Figure (4.8) suggest that the film magnetization is weakly anisotropic; exhibiting four-fold symmetry with its easy axes aligned along the $\{110\}$ axes of the SrTiO$_3$ (100) substrate. This result is further confirmation that the annealed film is epitaxial.

4.0.3 Results: Elastic control of the magnetism in $Fe_{16}Pd_{84}/BaTiO_3$ films

In this section of the dissertation, the results of the *Elastic control of the magnetism in* $Fe_{16}Pd_{84}/BaTiO_3$ *(100)* experiments will be discussed. Using XRD crystallography, we were able to characterize the structure of the $Fe_{16}Pd_{84}/BaTiO_3$ (100) sample at room temperature. The resulting XRD profile is displayed in Figure (4.9).

From this figure, it is clear that the film has several ordered phases. Since the film was deposited using co-deposition of both Fe and Pd vapor, within the film there are several possible phases involving Fe, Pd, and potentially O, if an iron oxide was formed at the film/substrate interface. In order to determine the phases present in the sample, we calculated the angular positions of the Bragg reflections of each possible phase of the sample using Equation (4.2). The 2θ positions of each of the simulated bulk phases are displayed in Table (4.4). The species of the phases responsible for the labeled peaks in the XRD profile at 23 ^oC [Figure (4.9)] were determined using the calculated angular positions of Tables (4.4) and (4.5). Allowing a tolerance of 5%, the peaks were fit to the XRD profile. A few of these peaks are highlighted in Figure (4.9).

In the room temperature XRD pattern displayed in Figure (4.9), Bragg peaks resulting from reflections from the (100), (200) and (111) planes of the $FePd_3$ and FePd are each present. Since the $BaTiO_3$ substrate was cleaved along the (100) plane, the presence of peaks other than those resulting from reflections from planes with (h00) orientation suggests that the film is not epitaxial. However, since several peaks are observed, it is clear that the sample is not structurally disordered. Consequently, one can conclude that the crystalline structure of the sample is textured.

While the $FePd_3$ (200), (111), and (100) phases are all present, it is important to note the presence of the ϵ-Fe_2O_3 (100), (111), and (200) Bragg peaks. The magnetic and structural properties of this oxide along with other Fe-oxides are displayed in Table (4.7)[cite]. The magnetic state of the ϵ-Fe_2O_3 phase is anti-ferromagnetic.

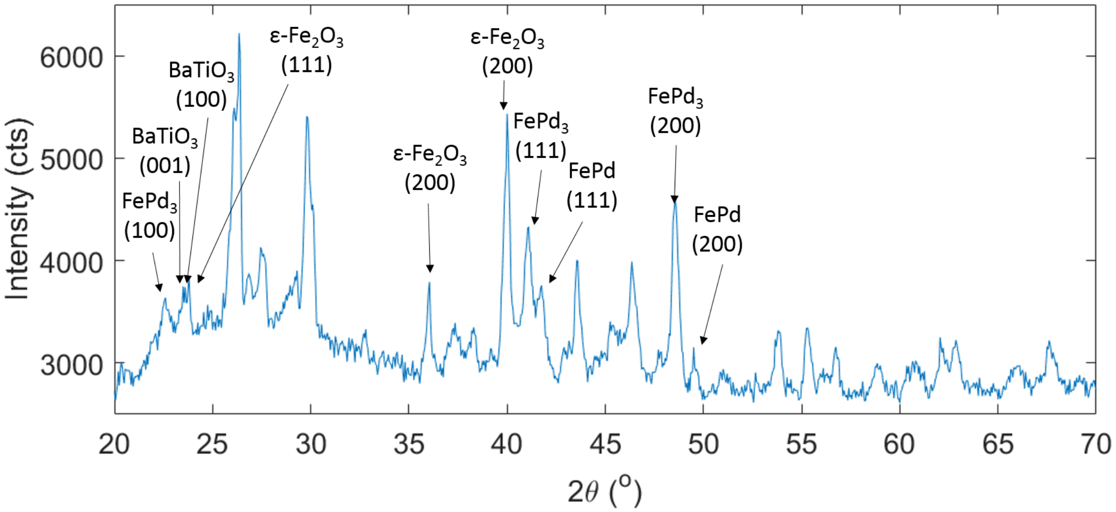

Figure 4.9: XRD pattern of $Fe_{16}Pd_{84}/BaTiO_3(100)$ at 23^oC with labeled phases

Phase	(100)	(101)	(011)	(110)	(111)	(200)	(002)
$BaTiO_3$(C)	22.1732^o	31.5598^o	31.5598^o	31.5598^o	38.902^o	45.2359^o	45.2359^o
$BaTiO_3$(T)	22.2603^o	31.5049	31.5049^o	31.6855	38.9160^o	45.4213^o	44.8874^o
$FePd_3$	23.1134^o	32.9170	32.9170^o	32.9170	40.6073^o	47.241^o	47.241^o
FePd	N/A	33.4731	33.4731	34.0553	41.5486^o	48.9289^o	47.1888^o
Fe	N/A	N/A	N/A	N/A	54.45^o	64.99^o	64.99^o
Pd	N/A	N/A	N/A	40.15^o	46.70^o	46.70^o	46.70^o
Au(fcc)	N/A	N/A	N/A	38.23^o	44.43^o	44.43^o	44.43^o
ϵ-Fe_2O_3	17.4051	19.8023	13.7672	20.1440	22.2585	35.2289	18.8061

Table 4.4: Simulated Bragg Reflections of possible phases in $Fe_{16}Pd_{84}/BaTiO_3$ sample

Since the Pd,Fe phases are ferromagnetic at room temperature (2.4.2), at the points of contact between the ϵ-Fe_2O_3 and Pd,Fe phases, the center of the hysteresis loop will shift in **H** due to the presence of an exchange bias. The basic physics of this effect were discussed in the MOKE implementations subsection [Section(2.6)].

In order to characterize the magnetization (**M**) of the sample as a function of temperature, the MOKE magnetometer was used in both the longitudinal and polar configurations to determine the in-plane and out-of-plane magnetization of the film for each temperature, respectively. The longitudinal results are displayed in Figure (4.10)

Phase	(220)	(022)
$BaTiO_3$(C)	65.8970^o	65.8970^o
$BaTiO_3$(T)	66.1855^o	65.771^o
$FePd_3$	69.1969^o	69.1969^o
FePd	71.7001^o	70.3314^o
Fe	98.8814^o	98.8814^o
Pd	68.18^o	68.18^o
Au(fcc)	64.64^o	64.64^o
ϵ-Fe_2O_3	40.9466^o	27.7384^o

Table 4.5: Simulated Bragg Reflections of possible phases in $Fe_{16}Pd_{84}/BaTiO_3$ sample (continued)

and the polar MOKE results are displayed in Figure (4.11). For the high temperature measurements, a resistive heater was used to control the temperature of the sample. Referring to the longitudinal (in-plane) MOKE measurements conducted below the T-C transition, the **M** v. **H** plots demonstrate hysteresis, while the magnetization saturates at each temperature below the T-C transition. It is important to note that for these measurements, the remnant magnetization and the saturation magnetization ($\frac{\mathbf{M}_r}{\mathbf{M}_\mathrm{S}}$) is equal to .95.

Meanwhile, the polar MOKE measurements conducted at the same temperatures suggest that the out-of-plane magnetization of the sample exhibits a small amount of hysteresis, but never reaches saturation. For these results $\frac{\mathbf{M}_\mathrm{R}}{\mathbf{M}_\mathrm{S}}$ ∼.25. The small size of this ratio suggests that $\mathbf{M}_R$ is negligible out of plane. Since $\mathbf{M}_R$ is a measure of the spontaneous magnetization, these results suggest that below the T-C transition, the sample is ferromagnetic with a spontaneous magnetization that lies along the sample plane. However, above the T-C transition, the behavior of the magnetization changes. For temperatures above this transition, the M_R of the longitudinal (in-plane) signal decreases, while that of the polar (out-of-plane) signal increases, until the switching behavior which was present in-plane is now observed out-of-plane. The transition in behavior seems to stabilize at 160^oC. The polar MOKE signal at this temperature is displayed in Figure (4.11). In this figure, it is clear that the M_R is equal to the M_S

Phase	unit cell	a,b,c (Å)	magnetic state
ϵ-Fe_2O_3	orthorhombic	a:5.095,b:8.79,c:9.437	AFM
Magnetite Fe_3O_4	fcc	a:8.39	ferrimagnetic
Maghemite γ-Fe_2O_3	cubic	8.34 Å	ferrimagnetics
Magnetite Fe_3O_4	cubic	a:8.34	ferrimagnetic
Hematite α-Fe_2O_3	hexagonal	a:5.034,c:13.75	weakly FM

Table 4.6: Iron-oxide with AFM phases along with a few characteristic properties

Phase	T_{order}(K)
ϵ-Fe_2O_3	1026
Magnetite Fe_3O_4	850
Maghemite γ-Fe_2O_3	820-986
Magnetite Fe_3O_4	850
Hematite α-Fe_2O_3	956

Table 4.7: Iron-oxide with AFM phases along with a few characteristic properties (continued)

($\frac{\mathbf{M_R}}{\mathbf{M_S}}$) and that there is significant hysteresis. The coercivity is equal to .5 G which is comparable to the in-plane value below the T-C transition. For temperatures above the T-C transition and below 160^{o}C, the signal fluctuates as though in a transition region.

Meanwhile, $\frac{\mathbf{M_R}}{\mathbf{M_S}} \sim 0$ of the longitudinal MOKE loops above the T-C transition. These results suggest that the magnetization has switched out-of-plane.

It is important to note, the shift of the center of the hysteresis loop along the **H**-axis. This shift of the hysteresis loop along the H-field axis suggests that there is an exchange bias field which results in the a larger **H** required to switch the sample spins. Since the exchange bias is typically observed at an FM/AFM interface, this result suggests the presence of an oxide layer at the film-substrate interface *Nogus and Schuller* (1999). This result is confirmed in Figure (4.9), where the Bragg reflections of the ϵ-Fe_2O_3 phase are present. In Table (4.7),the different iron-oxides phases along with a few of their characteristic properties. The results of the longitudinal MOKE measurements are displayed in Figure (4.10).

In order to determine the source of this phenomenon, High-temperature XRD measurements were conducted at temperatures above and below the T-C transition temperature. The results of these measurements are displayed in Figure (4.12). It is clear from this measurement that the peak $FePd_3$ (111) and (100) peak is present at RT, but then disappears at 100^oC, and remains absent until the T-C transition temperature (137^oC) is reached. For temperatures slightly above this temperature, this peak appears and disappears until 150^oC where it stabilizes and continues to persist until the maximum temperature, 200 ^{o}C, is reached. This behavior is also observed in the $FePd_3$(100) peak, but not observed in the $FePd_3$(200) for temperatures above room temperature, and then disappears, but returns for temperatures above the T-C transition.These results suggest that the $FePd_3$ crystallites with $FePd_3$<111>//$BaTiO_3$<100> are responsible for this behavior.

While the $FePd_3$ (100) and (111) peaks, are affected by the change in strain, the $FePd_3$(200) peak remains unchanged. Although the substrate/ film coupling is significant at the interface where the grains are epitaxial, since the film is thick (137 nm), after reaching a critical thickness, the $FePd_3$ crystallites within the film relaxed. As was mentioned in Section (2.7), this relaxation resulted in the decoupling of the crystallites from the substrate. Consequently, over the distance between the $FePd_3$(200) planes, the coupling decreases enough such that the strain effects of the substrate are not experienced by the $FePd_3$ crystallites far from the interface. This result is also confirmed by the small size of the signal above the T-C transition.

Returning to Figure (4.12), it is also important to note the variation of the $FePd_3$(111) peak as the temperature is increased. Above the T-C transition temperature, the rate of change of the angular position of the $FePd_3$ (111) peak as a function of temperature appears to decrease above the T-C transition. This result signifies the decrease in the thermal expansion of the $FePd_3$ (111) crystallites. This effect is a signature of invar behavior. This finding would be consistent with the work of Winterrose et. al. where pressure-induced invar behavior was observed in bulk $FePd_3$

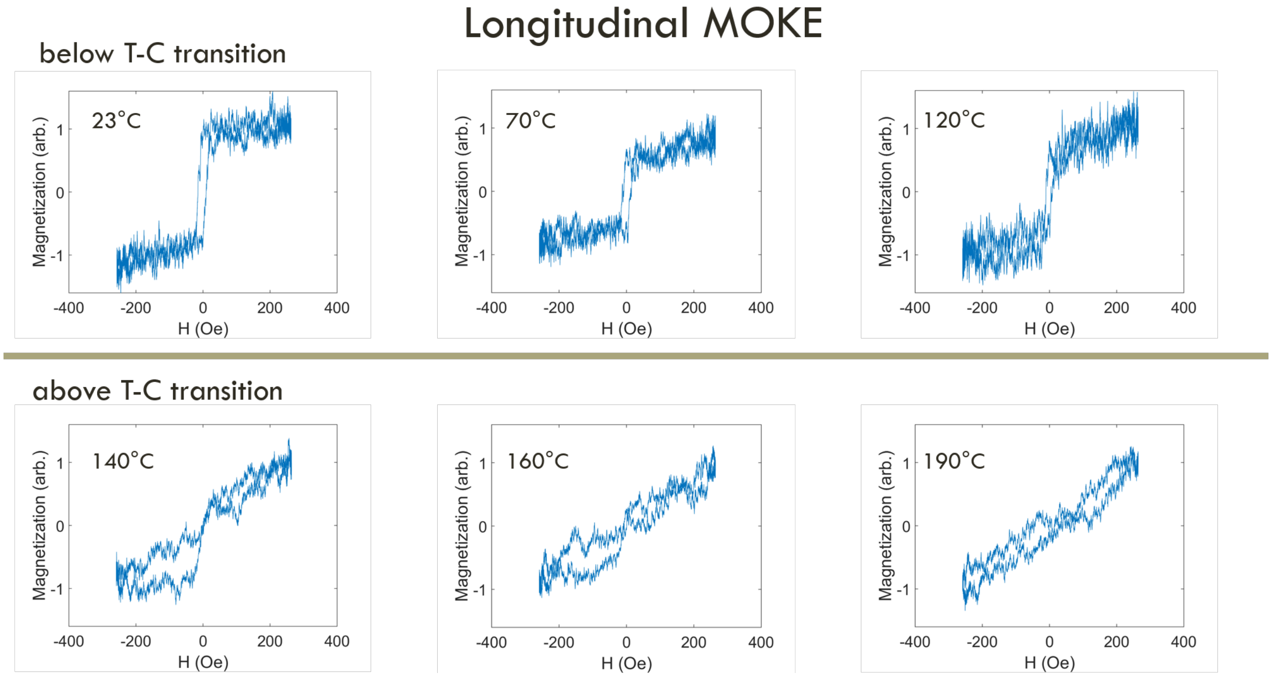

Figure 4.10: In-plane Magnetization v. **H** for various temperatures

in *Winterrose et al.* (2009). In order to confirm this finding further investigation is needed.

Displayed in Figure (3.1) are the longitudinal MOKE signals at various temperatures between 40^{o}C and 180^{o}C. The longitudinal MOKE signals at these temperatures can be found in Figure(4.10).

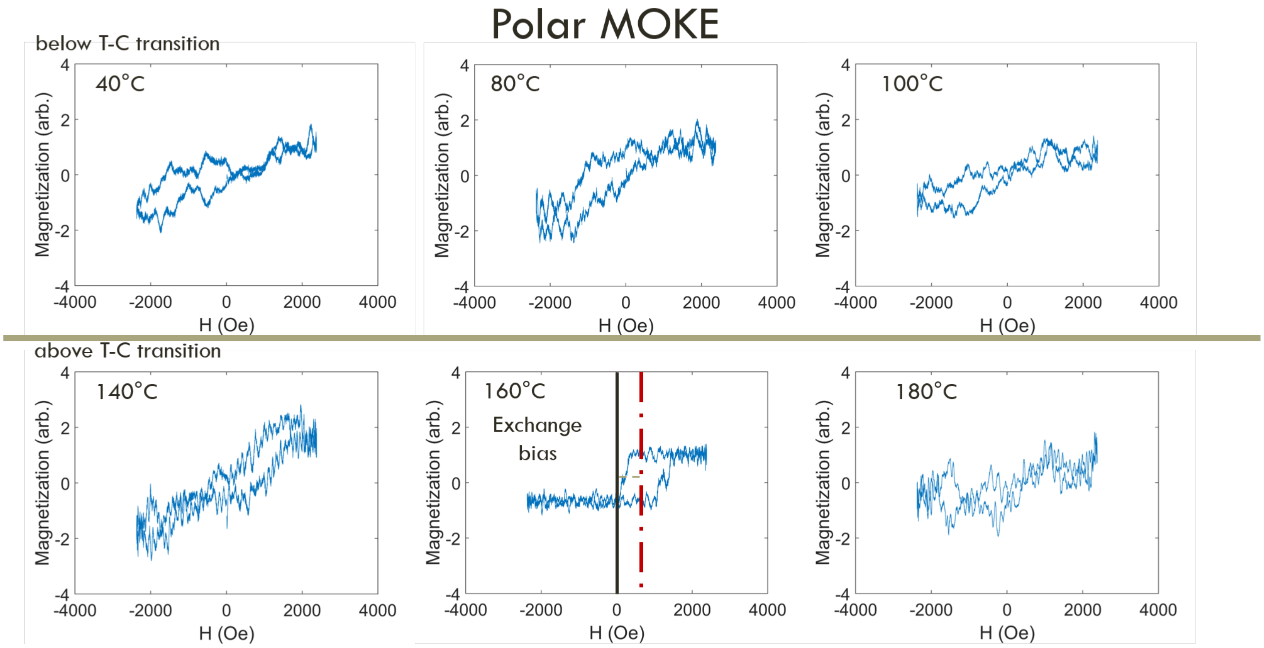

Figure 4.11: Out-of-plane Magnetization v. **H** for various temperatures

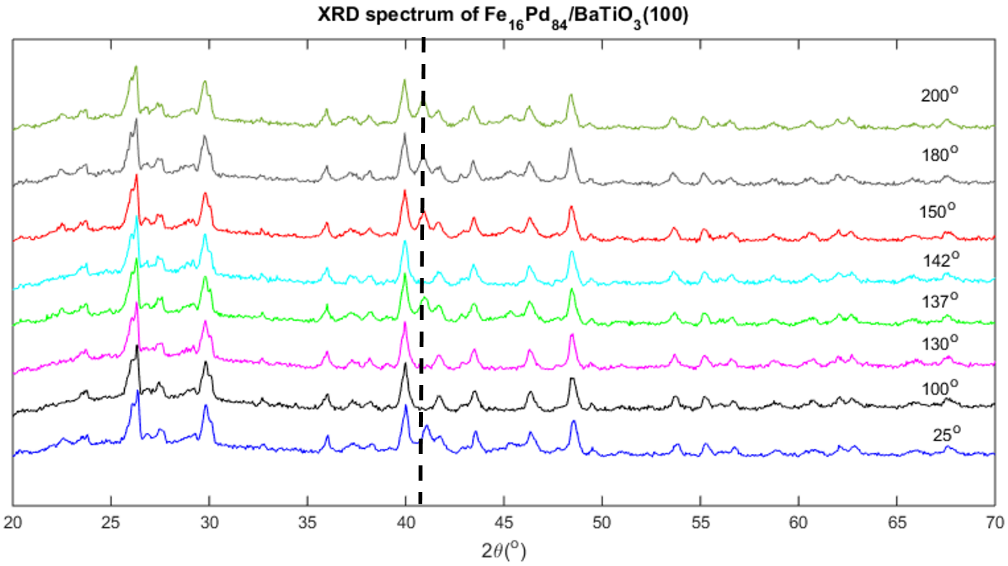

Figure 4.12: X-Ray diffraction pattern of $Pd_{84}Fe_{16}/BaTiO_3(100)$ at various temperatures

CHAPTER V

Conclusions and Future work

The work described in this dissertation can be separated into two parts. One part focused on the elastic control of the magnetism of Pd,Fe films deposited onto $BaTiO_3$(100), while the other part focused on enhancing the coupling between the substrate and the ferromagnetic film by fabricating an ordered $FePd_3$ film onto a perovskite, $SrTiO_3$. For the parts of the dissertation focusing on *elastic control*, we first discussed the current state of high density recording media and why the ability to control the perpendicular magnetic anisotropy of a magnetic film is important. The goal of our work was to control the perpendicular magnetic anisotropy of a Pd,Fe film by imparting a tetragonal distortion to the film using the tetragonal $BaTiO_3$ (100). After the discussion of the goal of this work, the methods used to grow and characterize the structure and magnetization of the Pd,Fe/$BaTiO_3$(100) sample as a function of temperature were discussed. In order to enhance the effect of the strain in the tetragonal phase, the Pd,Fe film with a thickness of 110 nm was deposited onto the $BaTiO_3$ (100) while in its cubic phase. MOKE magnetometry and XRD characterization at temperatures above and below the T-C transition were used to determine the effect of the tetragonal distortion on the deposited Pd,Fe film. The results of this study suggest that we were able to tune the perpendicular magnetic anisotropy using a distortion of -.7 % along the c-axis and .4 % along the a-axis of the $BaTiO_3$ (100) substrate across its tetragonal to cubic phase transition. Using high-temperature XRD analysis, we were able to conclude that the $FePd_3$ phase was responsible for the observed perpendicular anisotropy phenomena. However, due to the relaxation of the film, only crystallites near the substrate surface experienced significant coupling between the substrate and film. Accordingly, for future work, it would be important to examine the effect of film thickness on this phenomenon by fabricating a wedge sample with a range of thicknesses. Moreover, to optimize this coupling, it is important to conduct total energy calculations using density functional theory to aid in the fabrication of future heterostructures. Although the findings of this study are consistent with the results of *Winkelmann et al.* (2006), to the best of our knowledge this work is the first time that a reversible tetragonal distortion has been used to control the perpendicular magnetic anisotropy. Since perpendicular magnetic anisotropy is important for high density recording, this demonstration signifies a major advancement in this field.

Since this effect was observed using strain induced by the phase transition of the $BaTiO_3$ substrate, future work could explore different methods to impart this kind of strain to the ferromagnetic film, one possibility is using a piezoelectric substrate. Exploiting the coupling between the electric state and the elastic state of the material in such a substrate would enable one to control the magnetization using a simple voltage signal applied across the substrate interface region. Another aspect of our work focused on the growth of an ordered $FePd_3$ phase on the ABO_3 perovskite. Using Atomic Layer Epitaxy, we were able to fabricate an epitaxial Fe/Pd multilayer heterostructure onto $SrTiO_3$. We accomplished the growth of this structure by first depositing the following sequence of layers: Fe(30 nm)/Pd(38 nm)/Fe(10 nm)/Pd(19 nm). Once grown, the heterostructure was annealed above the formation temperature of $FePd_3$ at 550^o C. After annealing for 15 minutes at this temperature, the $FePd_3$ phase was observed. The results of XRD analysis demonstrated conclusively that the film had an excellent epitaxial match with the $SrTiO_3$ (100) substrate. Using MOKE magnetometry, we found that the sample exhibited in-plane magnetization reversal at ambient temperature. In this study, the minimum thickness for ordering upon annealing of the two bilayers of the heterostructure was not explored. This technique could also be used to enhance the magneto-elastic coupling between the $FePd_3$ film and the $BaTiO_3$ (100)substrate by growing an ordered $FePd_3$ phase.

Most of the work in this thesis relates to static strain, in the future, we could explore dynamic effects, investigating the effects of transient strain induced by laser pulses. Since, pressure-induced invar behavior has been observed in this material, *Winterrose et al.* (2009), it would be interesting to see the effects of transient strain on spin waves in $FePd_3$. In the magnetostrictive material, we could generate phonons impulsively using ultra-fast laser pulses. Due to the magnetostrictive coupling this could induce switching on the ultra-fast time (sub-picosecond) scale. This approach could be used for the manipulation of the magnetization, including switching, using only optical pulses rather than magnetic fields generated by a solenoid. This opens up the possibility to accomplish all-optical magnetization manipulation, including ultrafast dynamical switching.

Moreover, since $SrTiO_3$ has a high electric susceptibility, *Uwe et al.* (1973), future work could also include the fabrication of epitaxial heterostructures consisting of $FePd_3$ deposited onto $SrTiO_3$ with a patterned electrode. This structure would allow one to study the effect of magneto-electric coupling between the $SrTiO_3$ and the ferromagnetic thin film. The work presented here points the way to new and interesting future directions for novel magnetic recording media that are compatible with all-optical switching. The physics of magnetoelectric coupling in such materials is currently a very active area of study and is likely to reveal many new avenues for research into the future.

BIBLIOGRAPHY

BIBLIOGRAPHY

Ablowitz, M. J., and A. S. Fokas (2003), *Complex variables: introduction and applications*, Cambridge texts in applied mathematics, 2nd ed ed., Cambridge University Press, Cambridge, UK ; New York.

Arae, F., H. Arimune, F. Ono, and O. Yamada (1985), Anomalous Temperature and Field Dependences of Magnetocrystalline Anisotropy in Disordered FePt and FePd Invar Alloys, *Journal of the Physical Society of Japan*, *54*(8), 3098–3105, doi:10.1143/JPSJ.54.3098.

Ashcroft, N. W., and N. D. Mermin (1976), *Solid state physics*, Holt, Rinehart and Winston, New York.

Burkert, T., L. Nordstrm, O. Eriksson, and O. Heinonen (2004), Giant Magnetic Anisotropy in Tetragonal FeCo Alloys, *Physical Review Letters*, *93*(2), doi:10.1103/PhysRevLett.93.027203.

Buschbeck, J., et al. (2009), Full Tunability of Strain along the fcc-bcc Bain Path in Epitaxial Films and Consequences for Magnetic Properties, *Physical Review Letters*, *103*(21), doi:10.1103/PhysRevLett.103.216101.

Chiarotti, G. (1995), 1.6 Crystal structures and bulk lattice parameters of materials quoted in the volume, in *Interaction of Charged Particles and Atoms with Surfaces*, vol. 24c, edited by G. Chiarotti, pp. 21–26, Springer-Verlag, Berlin/Heidelberg.

Clarke, R. (1976), Phase transition studies of pure and flux-grown barium titanate crystals, *Journal of Applied Crystallography*, *9*(4), 335–338, doi:10.1107/S0021889876011436.

Coey, J. M. D. (2010), *Magnetism and magnetic materials*, Cambridge University Press, Cambridge.

Comes, R., M. Lambert, and A. Guinier (1968), The chain structure of BaTiO3 and KNbO3, *Solid State Communications*, *6*(10), 715–719, doi:10.1016/0038-1098(68)90571-1.

Cornell, R. M., U. Schwertmann, and John Wiley & Sons (2003), *The iron oxides structure, properties, reactions, occurrences, and uses*, Wiley-VCH, Weinheim.

Delyagin, N. N., A. L. Erzinkyan, V. P. Parfenova, and S. I. Reyman (2002), Antiferromagnetic spin correlations in palladium-based Pd-Fe, Pd-Fe-Ag, and Pd-Fe-Rh magnetic alloys, *Journal of Experimental and Theoretical Physics*, *95*(6), 1056–1061, doi:10.1134/1.1537297.

Duc, N. H., and P. Brommer (2002), chapter 2 Magnetoelasticity in Nanoscale Heterogeneous Magnetic Materials, in *Handbook of Magnetic Materials*, vol. 14, pp. 89–198, Elsevier.

Endo, Y., Y. Yamanaka, Y. Kawamura, and M. Yamamoto (2005), Formation of L 1 $_0$ -type Ordered FePd Phase in Multilayers Composed of Fe and Pd, *Japanese Journal of Applied Physics*, *44*(5A), 3009–3014, doi:10.1143/JJAP.44.3009.

Ewerlin, M., B. Pfau, C. M. Gnther, S. Schaffert, S. Eisebitt, R. Abrudan, and H. Zabel (2013), Exploration of magnetic fluctuations in PdFe films, *Journal of Physics: Condensed Matter*, *25*(26), 266,001, doi:10.1088/0953-8984/25/26/266001.

Fiebig, M. (2005), Revival of the magnetoelectric effect, *Journal of Physics D: Applied Physics*, *38*(8), R123–R152, doi:10.1088/0022-3727/38/8/R01.

Fukamichi, K. (1979), Positive large linear magnetostriction in Fe-Pd crystalline alloys, *Journal of Applied Physics*, *50*(10), 6562, doi:10.1063/1.325718.

Gijs, M. A. M., F. Petroff, and European Materials Research Society (Eds.) (1997), *Magnetic ultra thin films, multilayers, and surfaces: proceedings of Symposium E on Magnetic Ultra Thin Films, Multilayers, and Surfaces of the 1996 E-MRS Spring Conference, Strasbourg, France, June 4-7, 1996*, no. v. 62 in European Materials Research Society symposia proceedings, Elsevier, Amsterdam ; New York.

Gorria, P., et al. (2009), Stress-induced Curie temperature increase in the Fe $_{64}$ Ni $_{36}$ invar alloy, *physica status solidi (RRL) - Rapid Research Letters*, *3*(4), 115–117, doi:10.1002/pssr.200903056.

Govind, R., V. Hari Babu, C.-T. Chiang, E. Magnano, F. Bondino, R. Denecke, and K.-M. Schindler (2013), Magnetic properties of self-assembled Fe nanoislands on BaTiO3(001), *Journal of Magnetism and Magnetic Materials*, *346*, 16–20, doi:10.1016/j.jmmm.2013.07.004.

Grupp, D. E. (1997), Giant Piezoelectric Effect in Strontium Titanate at Cryogenic Temperatures, *Science*, *276*(5311), 392–394, doi:10.1126/science.276.5311.392.

Haeni, J. H., et al. (2004), Room-temperature ferroelectricity in strained SrTiO3, *Nature*, *430*(7001), 758–761, doi:10.1038/nature02773.

Hubert, A., and R. Schafer (1998), *Magnetic Domains the Analysis of Magnetic Microstructures.*

Ichimiya, A., and P. I. Cohen (2004), *Reflection High-Energy Electron Diffraction*, Cambridge University Press, Cambridge.

Kittel, C. (2005), *Introduction to solid state physics*, 8th ed ed., Wiley, Hoboken, NJ.

Kobliska, R. J., J. A. Aboaf, A. Gangulee, J. J. Cuomo, and E. Klokholm (1978), Amorphous ferromagnetic thin films, *Applied Physics Letters*, *33*(5), 473, doi:10.1063/1.90384.

Kovacs, A., K. Sato, and Y. Hirotsu (2007), High-resolution transmission electron microscopy analysis of L1[sub 0] ordering process in Fe/Pd thin layers, *Journal of Applied Physics*, *102*(12), 123,512, doi:10.1063/1.2826632.

Kvashnin, Y. O., S. Khmelevskyi, J. Kudrnovsk, A. N. Yaresko, L. Genovese, and P. Bruno (2012), Noncollinear magnetic ordering in compressed FePd 3 ordered alloy: A first principles study, *Physical Review B*, *86*(17), doi:10.1103/PhysRevB.86.174429.

Kwei, G. H., A. C. Lawson, S. J. L. Billinge, and S. W. Cheong (1993), Structures of the ferroelectric phases of barium titanate, *The Journal of Physical Chemistry*, *97*(10), 2368–2377, doi:10.1021/j100112a043.

Longworth, G. (1968), Temperature Dependence of the Fe 57 hfs in the Ordered Alloys Fe Pd 3 and FePd near the Curie Temperature, *Physical Review*, *172*(2), 572–576, doi:10.1103/PhysRev.172.572.

Meng, H., V. B. Naik, and R. Sbiaa (2013), Tuning of perpendicular exchange bias for magnetic memory applications, *physica status solidi (a)*, *210*(2), 391–394, doi:10.1002/pssa.201228487.

Miura, Y., S. Ozaki, Y. Kuwahara, M. Tsujikawa, K. Abe, and M. Shirai (2013), The origin of perpendicular magneto-crystalline anisotropy in L1 $_0$ FeNi under tetragonal distortion, *Journal of Physics: Condensed Matter*, *25*(10), 106,005, doi:10.1088/0953-8984/25/10/106005.

Myagkov, V., V. Zhigalov, B. Belyaev, L. Bykova, L. Solovyov, and G. Bondarenko (2012), Solid-state synthesis and magnetic properties of epitaxial FePd3(001) films, *Journal of Magnetism and Magnetic Materials*, *324*(8), 1571–1574, doi:10.1016/j.jmmm.2011.12.005.

Myagkov, V. G., V. S. Zhigalov, L. E. Bykova, L. A. Solovev, and G. N. Bondarenko (2010), Solid-phase synthesis of L10-FePd(001) epitaxial thin films: Structural transformations and magnetic anisotropy, *JETP Letters*, *91*(9), 481–485, doi:10.1134/S0021364010090109.

Nogus, J., and I. K. Schuller (1999), Exchange bias, *Journal of Magnetism and Magnetic Materials*, *192*(2), 203–232, doi:10.1016/S0304-8853(98)00266-2.

Okamoto, H. (1992), Fe-Pd phase diagram.

Okazaki, A., and M. Kawaminami (1973), Lattice constant of strontium titanate at low temperatures, *Materials Research Bulletin*, *8*(5), 545–550, doi:10.1016/0025-5408(73)90130-X.

Peng, Y., C. Park, and D. E. Laughlin (2003), Fe[sub 3]O[sub 4] thin films sputter deposited from iron oxide targets, *Journal of Applied Physics*, *93*(10), 7957, doi:10.1063/1.1556252.

Polisetty, S., W. Echtenkamp, K. Jones, X. He, S. Sahoo, and C. Binek (2010), Piezoelectric tuning of exchange bias in a BaTiO 3 / Co / CoO heterostructure, *Physical Review B*, *82*(13), doi:10.1103/PhysRevB.82.134419.

Qiu, Z. Q., and S. D. Bader (2000), Surface magneto-optic Kerr effect, *Review of Scientific Instruments*, *71*(3), 1243, doi:10.1063/1.1150496.

Rabe, K. (2007), *Physics of Ferroelectrics*, *Topics in Applied Physics*, vol. 105, Springer Berlin Heidelberg, Berlin, Heidelberg.

Ramesh, R., and N. A. Spaldin (2007), Multiferroics: progress and prospects in thin films, *Nature Materials*, *6*(1), 21–29, doi:10.1038/nmat1805.

Sahoo, S., S. Polisetty, C.-G. Duan, S. S. Jaswal, E. Y. Tsymbal, and C. Binek (2007), Ferroelectric control of magnetism in Ba Ti O 3 Fe heterostructures via interface strain coupling, *Physical Review B*, *76*(9), doi:10.1103/PhysRevB.76.092108.

Sbiaa, R., H. Meng, and S. N. Piramanayagam (2011), Materials with perpendicular magnetic anisotropy for magnetic random access memory, *physica status solidi (RRL) - Rapid Research Letters*, *5*(12), 413–419, doi:10.1002/pssr.201105420.

Shirahata, Y., T. Nozaki, G. Venkataiah, H. Taniguchi, M. Itoh, and T. Taniyama (2011), Switching of the symmetry of magnetic anisotropy in Fe/BaTiO3 heterostructures, *Applied Physics Letters*, *99*(2), 022,501, doi:10.1063/1.3609237.

Singh, J. (2003), *Electronic and optoelectronic properties of semiconductor structures*, Cambridge University Press, Cambridge ; New York.

Smith, W. F. (1995), *Scienza e tecnologia dei materiali*, McGraw Hill Libri Italia, Milano.

Thornton, J. A. (1986), The microstructure of sputter-deposited coatings, *Journal of Vacuum Science & Technology A: Vacuum, Surfaces, and Films*, *4*(6), 3059, doi:10.1116/1.573628.

Tiwari, U., R. Ghosh, and P. Sen (1994), Theory of magneto-optic Kerr effects, *Physical Review B*, *49*(3), 2159–2162, doi:10.1103/PhysRevB.49.2159.

Uwe, H., H. Unoki, Y. Fujii, and T. Sakudo (1973), Stress induced ferroelectricity in KTaO3, *Solid State Communications*, *13*(7), 737–739, doi:10.1016/0038-1098(73)90356-6.

Venkataiah, G., Y. Shirahata, I. Suzuki, M. Itoh, and T. Taniyama (2012), Strain-induced reversible and irreversible magnetization switching in Fe/BaTiO3 heterostructures, *Journal of Applied Physics*, *111*(3), 033,921, doi:10.1063/1.3684695.

Wang, C., K. Kuo, C. Lin, and G. Chern (2009), Magnetic anisotropy in (, .44, .55, .67, and .78) alloy film grown on and MgO(001) by molecular beam epitaxy, *Solid State Communications*, *149*(37-38), 1523–1526, doi:10.1016/j.ssc.2009.06.005.

Wei, D. H., and Y. D. Yao (2009), Controlling microstructure and magnetization process of FePd (001) films by staged thermal modification, *Applied Physics Letters*, *95*(17), 172,503, doi:10.1063/1.3246795.

Wijn, H. P. J. (1997), 1.1.2.6 Magnetostriction coefficients, in *3d, 4d and 5d Elements, Alloys and Compounds*, vol. 32A, edited by H. P. J. Wijn, pp. 39–40, Springer-Verlag, Berlin/Heidelberg.

Winkelmann, A., M. Przybylski, F. Luo, Y. Shi, and J. Barthel (2006), Perpendicular Magnetic Anisotropy Induced by Tetragonal Distortion of FeCo Alloy Films Grown on Pd(001), *Physical Review Letters*, *96*(25), doi:10.1103/PhysRevLett.96.257205.

Winterrose, M. L., M. S. Lucas, A. F. Yue, I. Halevy, L. Mauger, J. A. Muoz, J. Hu, M. Lerche, and B. Fultz (2009), Pressure-Induced Invar Behavior in Pd 3 Fe, *Physical Review Letters*, *102*(23), doi:10.1103/PhysRevLett.102.237202.

Wunderlich, W., K. Takahashi, D. Kubo, Y. Matsumura, and Y. Nishi (2009), Magnetostriction properties of FePd thin films: Dependence on microstructure, *Journal of Alloys and Compounds*, *475*(12), 339–342, doi:10.1016/j.jallcom.2008.07.041.

Yang, Y. T., Y. Q. Song, D. H. Wang, J. L. Gao, L. Y. Lv, Q. Q. Cao, and Y. W. Du (2014), Electric field control of magnetism in FePd/PMN-PT heterostructure for magnetoelectric memory devices, *Journal of Applied Physics*, *115*(2), 024,903, doi:10.1063/1.4861618.

Yousuf, M., P. C. Sahu, and K. G. Rajan (1986), High-pressure and high-temperature electrical resistivity of ferromagnetic transition metals: Nickel and iron, *Physical Review B*, *34*(11), 8086–8100, doi:10.1103/PhysRevB.34.8086.

Zhao, T., et al. (2006), Electrical control of antiferromagnetic domains in multiferroic BiFeO3 films at room temperature, *Nature Materials*, *5*(10), 823–829, doi:10.1038/nmat1731.